

TECHNICAL REPORT



Defense Threat Reduction Agency
8725 John J. Kingman Road, MS
6201 Fort Belvoir, VA 22060-6201



DTRA-TR-16-63

Understanding the Electronic Structure of the a-B₅C:H_x-to-Metal Interface

Distribution Statement A. Approved for public release; distribution is unlimited.

June 2016

HDTRA1-10-1-0092

Michelle M. Paquette et al.

Prepared by:
University of Missouri-Kansas
City
621 S. Sierra Madre
5100 Rockhill Rd.
Kansas City, MO, 64110

DESTRUCTION NOTICE:

Destroy this report when it is no longer needed.
Do not return to sender.

PLEASE NOTIFY THE DEFENSE THREAT REDUCTION
AGENCY, ATTN: DTRIAC/ J9STT, 8725 JOHN J. KINGMAN ROAD,
MS-6201, FT BELVOIR, VA 22060-6201, IF YOUR ADDRESS
IS INCORRECT, IF YOU WISH IT DELETED FROM THE
DISTRIBUTION LIST, OR IF THE ADDRESSEE IS NO
LONGER EMPLOYED BY YOUR ORGANIZATION.

REPORT DOCUMENTATION PAGE				Form Approved OMB No. 0704-0188	
<p>The public reporting burden for this collection of information is estimated to average 1 hour per response, including the time for reviewing instructions, searching existing data sources, gathering and maintaining the data needed, and completing and reviewing the collection of information. Send comments regarding this burden estimate or any other aspect of this collection of information, including suggestions for reducing the burden, to Department of Defense, Washington Headquarters Services, Directorate for Information Operations and Reports (0704-0188), 1215 Jefferson Davis Highway, Suite 1204, Arlington, VA 22202-4302. Respondents should be aware that notwithstanding any other provision of law, no person shall be subject to any penalty for failing to comply with a collection of information if it does not display a currently valid OMB control number.</p> <p>PLEASE DO NOT RETURN YOUR FORM TO THE ABOVE ADDRESS.</p>					
1. REPORT DATE (DD-MM-YYYY) 00-06-2016	2. REPORT TYPE Final technical report	3. DATES COVERED (From - To) 08/17/2010-08/16/2015			
4. TITLE AND SUBTITLE Understanding the Electronic Structure of the a-B5C:Hx-to-Metal Interface			5a. CONTRACT NUMBER		
			5b. GRANT NUMBER HDTRA1-10-1-0092		
			5c. PROGRAM ELEMENT NUMBER		
6. AUTHOR(S) Paquette, Michelle M., Bhattarai, Gyanendra, Caruso, Anthony N.			5d. PROJECT NUMBER		
			5e. TASK NUMBER		
			5f. WORK UNIT NUMBER		
7. PERFORMING ORGANIZATION NAME(S) AND ADDRESS(ES) Curators of the University of Missouri on behalf of the University of Missouri-Kansas City			8. PERFORMING ORGANIZATION REPORT NUMBER		
9. SPONSORING/MONITORING AGENCY NAME(S) AND ADDRESS(ES) Defense Threat Reduction Agency 8725 John J. Kingman Road Fort Belvoir, VA 22060-6201			10. SPONSOR/MONITOR'S ACRONYM(S) DTRA		
			11. SPONSOR/MONITOR'S REPORT NUMBER(S) DTRA-TR-16-63		
12. DISTRIBUTION/AVAILABILITY STATEMENT Distribution Statement A					
13. SUPPLEMENTARY NOTES					
14. ABSTRACT The interfacial and bulk electronic structure and charge transport properties of amorphous hydrogenated boron carbide (a-BC:H) were investigated toward its application in solid-state direct-conversion neutron detection. From photoemission spectroscopy and current-voltage measurements, it was found that a range of metals exhibited ohmic injection. From space-charge-limited-current and steady-state photoconductivity measurements, it was found that films could be deposited with the charge carrier mobility and lifetime required for maximum theoretical detection efficiencies for a model planar thin-film (15 um) detector heterostructure scenario.					
15. SUBJECT TERMS amorphous hydrogenated boron carbide, direct-conversion neutron detection, charge transport, electronic structure, mobility, mobility-lifetime product, photoemission spectroscopy, steady-state photoconductivity, space-charge-limited current, plasma-enhanced chemical vapor deposition					
16. SECURITY CLASSIFICATION OF: a. REPORT U b. ABSTRACT SAR c. THIS PAGE SAR			17. LIMITATION OF ABSTRACT UU	18. NUMBER OF PAGES 77	19a. NAME OF RESPONSIBLE PERSON Anthony N. Caruso (carusoan@umkc.edu)

UNIT CONVERSION TABLE
U.S. customary units to and from international units of measurement*

U.S. Customary Units	Multiply by ← Divide by [†]	International Units
Length/Area/Volume		
inch (in)	2.54 $\times 10^{-2}$	meter (m)
foot (ft)	3.048 $\times 10^{-1}$	meter (m)
yard (yd)	9.144 $\times 10^{-1}$	meter (m)
mile (mi, international)	1.609 344 $\times 10^3$	meter (m)
mile (nmi, nautical, U.S.)	1.852 $\times 10^3$	meter (m)
barn (b)	1 $\times 10^{-28}$	square meter (m^2)
gallon (gal, U.S. liquid)	3.785 412 $\times 10^{-3}$	cubic meter (m^3)
cubic foot (ft^3)	2.831 685 $\times 10^{-2}$	cubic meter (m^3)
Mass/Density		
pound (lb)	4.535 924 $\times 10^{-1}$	kilogram (kg)
unified atomic mass unit (amu)	1.660 539 $\times 10^{-27}$	kilogram (kg)
pound-mass per cubic foot ($lb\ ft^{-3}$)	1.601 846 $\times 10^1$	kilogram per cubic meter ($kg\ m^{-3}$)
pound-force (lbf avoirdupois)	4.448 222	newton (N)
Energy/Work/Power		
electron volt (eV)	1.602 177 $\times 10^{-19}$	joule (J)
erg	1 $\times 10^{-7}$	joule (J)
kiloton (kt) (TNT equivalent)	4.184 $\times 10^{12}$	joule (J)
British thermal unit (Btu) (thermochemical)	1.054 350 $\times 10^3$	joule (J)
foot-pound-force (ft lbf)	1.355 818	joule (J)
calorie (cal) (thermochemical)	4.184	joule (J)
Pressure		
atmosphere (atm)	1.013 250 $\times 10^5$	pascal (Pa)
pound force per square inch (psi)	6.984 757 $\times 10^3$	pascal (Pa)
Temperature		
degree Fahrenheit ($^{\circ}\text{F}$)	$[\text{T}({}^{\circ}\text{F}) - 32]/1.8$	degree Celsius (${}^{\circ}\text{C}$)
degree Fahrenheit ($^{\circ}\text{F}$)	$[\text{T}({}^{\circ}\text{F}) + 459.67]/1.8$	kelvin (K)
Radiation		
curie (Ci) [activity of radionuclides]	3.7 $\times 10^{10}$	per second (s^{-1}) [becquerel (Bq)]
roentgen (R) [air exposure]	2.579 760 $\times 10^{-4}$	coulomb per kilogram ($C\ kg^{-1}$)
rad [absorbed dose]	1 $\times 10^{-2}$	joule per kilogram ($J\ kg^{-1}$) [gray (Gy)]
rem [equivalent and effective dose]	1 $\times 10^{-2}$	joule per kilogram ($J\ kg^{-1}$) [sievert (Sv)]

* Specific details regarding the implementation of SI units may be viewed at <http://www.bipm.org/en/si/>.

[†]Multiply the U.S. customary unit by the factor to get the international unit. Divide the international unit by the factor to get the U.S. customary unit.

1. TABLE OF CONTENTS

1. Table of Contents	2
2. Executive Summary	4
3. Introduction	6
3.1. Amorphous Hydrogenated Boron Carbide for Neutron Detection	6
4. Results and Discussion.....	10
4.1. Film Growth and Characterization.....	10
4.2. Metal-to-a-BC:H Interface Studies	17
4.2.1. Cr, Ti, Al, and Cu	17
4.2.2. Ni and Pd	21
4.2.3. Metal–Insulator–Metal Heterostructure Characterization	27
4.2.4. Summary	29
4.3. Charge Transport Measurements	30
4.3.1. Mobility Measurements	30
4.3.2. Mobility–Lifetime Product Measurements	42
4.4. Electronic Structure and Charge Transport Models.....	47
4.4.1. Electronic Structure Model.....	47
4.4.2. Charge Transport Model.....	50
4.5. Detector Modeling	53
4.5.1. Theory.....	53
4.5.2. Calculation and Assumptions	57
4.5.3. Results and Discussion	60
5. Metrics.....	67
5.1. Personnel.....	67
5.2. Publications.....	67

5.3.	Theses/Dissertations	68
5.4.	Presentations	68
5.5.	Honors/Awards/Promotions.....	70
5.6.	Graduations	71
6.	References	71
	Appendix A.....	77

2. EXECUTIVE SUMMARY

Toward replacing current neutron detection technologies, solid-state designs offer the promise of smaller/lighter detectors with lower power needs and monetary costs. Direct-conversion detectors, in contrast to conversion-layer detectors, are capable of achieving 100% thermal neutron detection efficiencies with thermal insensitivity and lower-complexity heterostructure designs. However, as these are based on immature semiconductor technologies, they remain in the fundamental research stage. A number of authors have reported the successful fabrication of direct-conversion neutron detector heterostructures from amorphous hydrogenated boron carbide ($a\text{-B}_x\text{C:H}_y$) grown on n-Si by plasma-enhanced chemical vapor deposition (PECVD) from carborane precursors. These have been limited to devices $\sim 1 \mu\text{m}$ thick with detection efficiencies of $<1\%$. It has been found that the experimental-to-theoretical efficiency drops as the thickness of the $a\text{-B}_x\text{C:H}_y$ layer increases, which highlights the tradeoff between higher neutron capture efficiency from thicker films and decreased charge collection efficiency owing to the poor/unoptimized charge transport properties of this material. The objective of this effort has been to rigorously investigate the charge transport properties of $a\text{-B}_x\text{C:H}_y$ films to understand how both interfacial and bulk transport contribute to detector heterostructure performance, while seeking to optimize these properties.

Over a hundred $a\text{-B}_x\text{C:H}_y$ films were grown with varying PECVD conditions. Films were deposited with an extremely wide range of properties, including growth rate from 1–112 nm/min, B/C ratio from 2.8–5.0, atomic concentration hydrogen (at.% H) from 10–45%, density from 0.9–2.3 g/cm³, hardness from 1–25 GPa, Young's modulus from 10–340 GPa, Tauc optical band gap from 1.7–4.0 eV, Tauc slope parameter ($B^{1/2}$) from ~ 200 –2200 cm^{-1/2}•eV^{-1/2}, Urbach energy from

0.1–0.8 eV, dielectric constant from 2.4–7.6, and electrical resistivity from 10^8 – 10^{15} Ω·cm. Strong correlations were found between chemical composition (mainly atomic concentration hydrogen, and to some extent atomic concentration carbon) with mechanical, optical, and electronic properties.

The chemical and electronic structure of the a-B_xC:H_y-to-metal interface was studied using photoemission techniques for six different metals: Cr, Ti, Al, Cu, Ni, and Pd. It was found that Cu and Ni form clean interfaces, whereas the remaining metals form interfacial oxides. Based on band lineup arguments, it was concluded that Cu should form a reasonable ohmic contact, but that Ni or Pd may be better suited as a hole injection/electron blocking electrode. The current–voltage study of metal–insulator–metal heterostructures with various metals/semiconductors revealed that all of the materials tested (including Cu, Al, Pd, Ti, and Si), regardless of work function or interfacial oxide formation, formed ohmic contacts. This was rationalized in terms of the very high resistivity of a-B_xC:H_y (and thus ease of attaining ohmic injection) as well as its amorphous structure, with localized states within the gap capable of facilitating charge injection.

To study bulk transport properties, both steady-state and transient (dark-injection) space-charge-limited-current (SCLC) techniques were applied to measure mobility, and steady-state photoconductivity techniques were applied to measure mobility–lifetime product. Based on the steady-state SCLC measurements of a large number of samples, it was found that mobility in a-B_xC:H_y ranged across ten orders of magnitude, from 10^{-5} – 10^{-14} cm²/V·s, resistivity from 10^8 – 10^{15} Ω·cm, and charge carrier concentration from 10^{14} – 10^{18} cm⁻³. Transient SCLC measurements were completed on a subset of samples, and values determined using the technique were consistently higher than those determined using the steady-state analog. This was rationalized as a consequence of slow trapping, which is reflected in the longer time scale of the steady-state experiment. Overall, the transient experiment may be more relevant to neutron detection as it is probing a similar timescale. Mobility–lifetime product ($\mu\tau$) measurements performed on low-mobility samples yielded $\mu\tau$ values on the order of 10^{-13} – 10^{-14} cm²/V, in the same range as the mobility, which suggested a relatively long lifetime on the order of 1 s. Mobility–lifetime product determinations for higher mobility samples and/or direct measurements of carrier lifetime will be needed to verify the generality of this observation. Charge transport properties did not show a simple correlation with either hydrogen concentration or electronic structure parameters, but rather showed two distinct regimes. This was rationalized as a transition from a variable range hopping mechanism

for films with low band gap and wide band tails to a multiple trapping mechanism for films with high band gap and narrow band tails.

Modeling of charge collection efficiency and neutron detection efficiency for the specific case of a planar thin-film detector with low mobility was completed to understand what charge transport figures of merit were required in a-B_xC:H_y to achieve a target detection efficiency. A numerical method was implemented to model the effects of transport parameters, mobility, lifetime, and mobility–lifetime product, as well as experimental parameters, film thickness, electric field, and integration time. It was shown that, because in a low mobility material, the transit time of charge carriers may be long relative to the integration time, it is not only $\mu\tau$ that determined charge collection efficiency, but also the individual μ and τ parameters. Further, because boron-rich B_xC has such strong neutron absorption and very high detection efficiencies can be obtained with thin films (10–100 μm), the charge transport requirements are forgiving. For a model detector of ¹⁰B-enriched B₄C with a thickness of 15 μm and excited carrier lifetime of 1 s, under an applied electric field of 1 MV/cm and with an integration time of 1 ms, the mobility required to achieve the maximum theoretical detection efficiency (~35–40%) is $5 \times 10^{-7} \text{ cm}^2/\text{V}\cdot\text{s}$. Based on the charge transport measurements of a-B_xC:H_y films, which demonstrated that mobilities within this range are achievable, it was concluded that—despite the poor transport properties of a-B_xC:H_y in general—it should be feasible to fabricate thick (10–50 μm) detectors with high efficiencies.

Overall, this effort has produced a large body of work investigating the charge transport properties of a-B_xC:H_y films, including the experimental techniques and analysis applied to extract these results. This work sets the stage for future work to not only demonstrate that detection is possible from a boron-rich direct-conversion detector, but that neutron detectors can be made with efficiencies competitive with the state-of-the-art.

3. INTRODUCTION

3.1. Amorphous Hydrogenated Boron Carbide for Neutron Detection

In the quest to replace golden standard (i.e., ³He) and less desirable (e.g., ¹⁰BF₃ or low-flash-point liquid scintillators) neutron-sensitive materials and transduction methods, 1700 US patents, over 3100 active US patent applications, and approximately 2700 journal articles have been issued or published over the last ten years. Of these reported concepts, three real-time detector class types

have emerged in contention for commercial viability: (1) scintillator-based; (2) ^{10}B -coated gas tube/straw-based; and, (3) semiconductor-based materials and transduction methods. Of the scintillator-based methods, viable embodiments include: (a) plastic scintillators with pulse shape discrimination; (b) elpasolite materials; and (c) ^6LiF :phosphor-based screen or readout fibers. In all scintillator cases, problems with light readout, volume, intrinsic efficiency, and/or production cost have prevented these materials from being accepted as industry standard replacements. Advanced versions of the ^{10}B gas tubes/straws are serious contenders for large-area instrumentation with the benefits of position sensitivity, but are intrinsically limited in their efficiency:volume metric and not of sufficiently lower cost than ^3He . Of the semiconductor-based methods are indirect- and direct-conversion neutron detectors.¹ Modern indirect-conversion neutron detectors with microstructuring have shown great promise with verified thermal neutron detection efficiencies for a single die as high as 26%² (or as high as 42% for a double-stacked device^{3,4}), with controversial reports of efficiencies up to 48%.^{5,6} However, processing requirements and low-band-gap-based thermal sensitivity have thwarted wide acceptance of these silicon-based devices. The solution requires a reduction in the processing complexity of the devices and/or reproducing the microstructuring with higher band-gap materials that have equivalent electrical carrier transport properties. Direct-conversion devices on the other hand have had no commercial consideration and remain in the fundamental research category despite the ability to theoretically produce such devices with low complexity and with thermal insensitivity (i.e., using wide-band-gap materials) to achieve unity thermal neutron detection efficiency.

The challenge to realizing a direct-conversion neutron detection device is that there exist very few semiconductor materials that contain isotopes with adequately high neutron-capture cross sections (^3He , ^6Li , ^{10}B , ^{113}Cd , ^{157}Gd , $^{235}\text{U}/^{238}\text{U}$), and the few that are known are not well-developed from a semiconductor technology standpoint. It is generally agreed that semiconductors containing ^6Li or ^{10}B are best-suited as solid-state neutron detectors due to their combination of high neutron and low gamma-ray cross sections.^{2,7} The class of boron-rich solids in particular boasts a number of semiconductor variants potentially viable for neutron detection, including BP,⁸ BN,^{9–12} B_xC ,^{13,14} B_{12}As_2 ,¹⁵ and Mg_2B_{14} ,¹⁶ among others, and various efforts have been put forth to develop these materials toward bulk crystalline, composite, as well as thin-film solid-state detectors. Along with BN, B_xC has been the most highly studied class of boron-rich solids for neutron detection. In particular, B_xC has shown promise as a high-resistivity ($>10^{10} \Omega\cdot\text{cm}$) carborane-based PECVD-

grown a-B_xC:H_y ($x = 3\text{--}5$) film (single crystalline B_xC displays inadequately low resistivity values on the order of $10 \Omega\cdot\text{cm}$,¹⁷ which implies problematic high leakage currents in a detection device, as is the case for many other possible B_xC variants). However, a-B_xC:H_y prototype detectors have only been fabricated with very thin films (on the order of ones of microns), which implies that charge pulses (above noise) can be obtained despite potentially poor transport properties, but at these thicknesses even ideal thermal neutron detection efficiencies are very low (less than 1 to a few percent). Film thicknesses in these devices will need to be on the order of tens to hundreds of microns^{12,18} in order to approach maximal efficiencies for thermal neutrons. A major limitation to scaling up thickness are poor charge transport properties, which lead to incomplete electron–hole pair (ehp) sweepout. Although amorphous B_xC:H_y may be predicted to have particularly poor transport properties due to its disordered nature, it possesses the advantage of having a large accessible configuration space of stable stoichiometric and structural variants and therefore high potential for tuning charge transport and other material properties.

To ascertain the viability of a-B_xC:H_y for thick, high-intrinsic-efficiency thermal neutron detectors, it must be determined whether this material can possess the right combination of charge transport properties, including a high resistivity, to minimize leakage current, good electrical stability (i.e., a high breakdown voltage and therefore ability to withstand moderate-to-high electric fields), and a sufficiently high mean carrier drift length (proportional to mobility and lifetime via $\lambda = \mu\tau E$, where E is electric field), to ensure maximum charge collection efficiency for ehp's that are generated.¹⁹ Determining the charge transport properties of a-B_xC:H_y is complicated by its high-resistivity, complex and unusual electronic structure, and disordered nature. Many traditional methods for measuring semiconductor properties cannot be used in the case of high-resistivity or low-mobility solids. Analyzing a high resistance thin film pushes the limits of experimental capabilities, often requiring extremely high input impedance electronics, additional shielding, and sophisticated circuitry to surmount issues including very high input resistances, extremely low current outputs, and complicating *RC* delays. Further, even when experimental measurements are feasible, the interpretation of results is complicated by the fact that nearly all theory developed for this purpose is based on assumptions (e.g., number and type of defect levels) that only hold true for less complex materials. Many of the methods applied here to study the charge transport of a-B_xC:H_y have been developed and/or tailored over recent decades to study first a-Si:H, and later more complex materials such as organic semiconductors, and include those

where signal is actually enhanced for low-mobility materials such as photoconductivity-based methods (where low dark currents imply low background noise) and time-resolved drift-mobility-based methods (where long transit times lead to more accessible experimental timescales). Further, to accurately measure charge transport properties as well as to fabricate neutron detectors with maximal efficiencies, establishing appropriate electrical contacts is critical. Depending on the type of device (e.g., p-n or schottky diode) or the type of electrical measurement (e.g., time-of-flight drift mobility or Hall mobility), either an injecting contact or blocking contact may be required. Other requirements may also include transparency, resistance against diffusion, and environmental stability (resistance to thermal treatment, oxidation). Without having a good understanding of the electronic structure and charge transport at the metal-to-a-B_xC:H_y interface, one cannot be confident in any measurements of the bulk.

Prior to this work, only a few reports on the charge transport properties of a-B_xC:H_y were available. Lee et al. reported resistivities on the order of $\sim 10^{10}$ Ω·cm for similar a-B_xC:H_y films grown by PECVD from borane derivatives in the early 1990's,^{20,21} as part of some of the earliest work prompting interest in this material for neutron detection applications. Several publications have also reported low leakage currents (recently 10^{-5} A/cm²)¹⁴ in reverse-biased p-n diode geometries. Although it has been evident for some time that carborane-based a-B_xC:H_y has a very high resistivity, prior to this work, no rigorous studies had been reported that investigated the range of charge transport properties possible in this material. Little else is known about the charge transport properties of this solid, although based on its extremely high resistivity, it can be assumed that it must exhibit both a low mobility and low free carrier concentration. a-B_xC:H_y appears to generally behave like a p-type semiconductor based on *I*-V properties of diodes constructed from this material, as most evident in a publication by Hong et al.²² In a recent publication,¹⁴ Hong et al. proposed a carrier density of 10^{12} cm⁻³ and a mobility range of 10^{-2} – 10^{-4} cm²·V⁻¹·s⁻¹ for a-B_xC:H_y films—values that were not confirmed by measurement, but are not inconsistent with predictions.

The following report describes efforts to both understand the charge transport properties needed in an a-B_xC:H_y neutron detector heterostructure to achieve competitive efficiencies, as well as the charge transport properties achievable by varying growth conditions. Although previous work on a-B_xC:H_y has focused on p–n diode detectors, this work emphasizes a more simple planar metal–insulator–metal resistive detector. It is shown that charge collection and detection efficiency

in a realistic experimental scenario must be modeled differently for thin film heterostructures than for a typical detector based on a thicker and higher mobility material. The techniques and analyses used for investigating the electronic structure and charge transport of a-B_xC:H_y are described, the range of properties measured are reported, and correlations between them discussed. This information provides the basis for tailoring a-B_xC:H_y films specifically for neutron detection applications based on growth conditions and chemical and electronic structure.

4. RESULTS AND DISCUSSION

4.1. Film Growth and Characterization

All amorphous hydrogenated boron carbide (a-B_xC:H_y) films described in this report were grown by plasma-enhanced chemical vapor deposition (PECVD) with an *ortho*-carborane (*o*-C₂B₁₀H₁₂) precursor and argon process gas using a custom-built capacitively coupled system. Details of the thin-film deposition process are described in [Nordell et al. JAP 118 \(2015\) 035703](#).²³ Briefly, the system consists of a 12 cm diameter upper rotating anode and substrate holder/heater and a 25 cm diameter lower cathode and precursor delivery system (i.e., showerhead) housed within an 80 L chamber. RF power at a standard frequency of 13.56 MHz is applied across the plates, at a separation of 4.4 cm. To deliver the solid-state precursor to the showerhead, heated argon gas is flowed through a heated ‘bubbler’ system, which consists of a glass nipple containing *ortho*-carborane loaded on top of a stack of glass beads. The bubbler is heated to 75 °C, and the gas lines and showerhead to 90 °C. The *ortho*-carborane is sourced from Katchem, and resublimed in vacuo prior to use. The argon process gas is sourced from Airgas at a purity of <10 ppb O₂ and <20 ppb H₂O. Restek O₂ and H₂O filters are installed in line to reduce the levels of these contaminants to the ppt range. Typically, batches of films are grown on different substrates so that these may be characterized by multiple techniques including ellipsometry (thickness, optical constants), optical transmission spectroscopy (absorption coefficient, band gap, Urbach energy, Tauc parameter), photoemission spectroscopy (atomic composition, electronic structure), fourier transform infrared spectroscopy (chemical bonding), nuclear reaction analysis (atomic composition, including at.% H), nanoindentation (hardness, Young’s modulus), and current–voltage and capacitance–voltage measurements.

We have designed a number of film growth experiments to systematically test the influence of process parameters on thin-film properties. These are summarized in Table 1. Results from the B, C, D, and N series growths are described in a series of publications:

- B. J. Nordell, S. Karki, T. D. Nguyen, P. Rulis, A. N. Caruso, S. S. Purohit, H. Li, S. W. King, D. Dutta, D. Gidley, W. A. Lanford, and M. M. Paquette, ‘The Influence of Hydrogen on the Chemical, Mechanical, Optical/Electronic, and Electrical Transport Properties of Amorphous Hydrogenated Boron Carbide,’ *Journal of Applied Physics* 118 (2015) 035703. [<http://dx.doi.org/10.1063/1.4927037>]
- B. J. Nordell, C. L. Keck, T. D. Nguyen, A. N. Caruso, S. S. Purohit, W. A. Lanford, D. Dutta, D. Gidley, P. Henry, S. W. King, and M. M. Paquette, ‘Tuning the Properties of a Complex Disordered Material: Full Factorial Investigation of PECVD-Grown Amorphous Hydrogenated Boron Carbide,’ **Submitted to Materials Chemistry and Physics, August 19 2015, MATCHEMPHYS-D-15-01944.**
- M. M. Paquette, J. W. Otto, W. A. Lanford, B. J. Nordell, S. Karki, S. W. King, and A. N. Caruso, ‘Thermal Treatment and Depth Profile Studies of Thin-Film Carborane-Based Amorphous Hydrogenated Boron Carbide Growth by Plasma-Enhanced Chemical Vapor Deposition,’ **(2015), To be submitted.**

Table 1. A selection of PECVD a-B_xC:H_y film growth experiments.

Series	No films	Description	Growth temp (C)	RF Power (W)	Pressure (Torr)	Total flow rate (sccm)	Partial flow rate	Anneal conditions
B	5	Temp dependence	300–500	30	200	50	0.2	–
C	7	Anneal dependence	350	30	200	50	0.2	Variable
D	24	Power/temp	25–450	5–30	200	50	0.2	–
N	37	2 ⁵ factorial	50, 400	10, 40	0.2, 4	50, 100	0.1, 0.5	–
Q	45	One at a time	75–400	10–40	0.4–8	10–200	0.1–2*	Variable
P	10	Anneal dependence	400	40	0.4	100	0.5	Variable

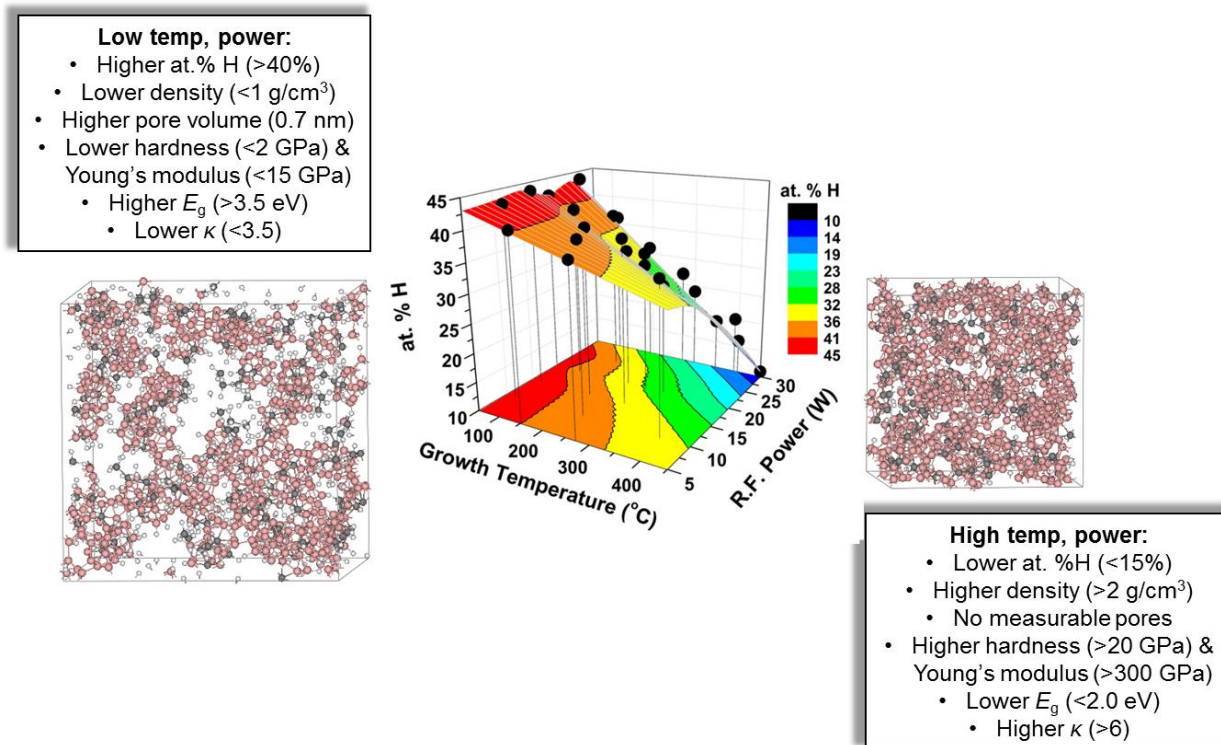


Figure 1. Atomic concentration hydrogen (at.% H) in a-B_xC:H_y films as a function of varying temperature and R.F. power during PECVD growth demonstrating how a-B_xC:H_y can range from low-density hydrogen-rich to high-density hydrogen-deficient films. [Figure adapted from [Nordell et al. JAP 118 \(2015\) 035703²³](#)].

The first publication, which covers a series of a-B_xC:H_y films deposited with varying growth temperature and power (i.e., the “D” series), emphasizes the influence of hydrogen concentration on thin-film properties. We found that we were able to produce films with an extremely wide range of properties, including H concentration from 10–45%, density from 0.9–2.3 g/cm³, hardness from 1–25 GPa, Young’s modulus from 10–340 GPa, Tauc optical band gap from 1.7–3.8 eV, Tauc slope parameter ($B^{1/2}$) from ~200–1600 cm^{-1/2}•eV^{-1/2}, Urbach energy (E_U) from 0.1–0.7 eV, dielectric constant from 3.2–7.6, and electrical resistivity from 10¹⁰–10¹⁵ Ω•cm (Figure 1). Hydrogen concentration was found to correlate directly with thin-film density, and both were used to map and explain the other material properties (Figure 2). Hardness and Young’s modulus exhibit a direct power law relationship with density above ~1.3 g/cm³ (or below ~35% H), below which they plateau, providing evidence for a rigidity percolation threshold. An increase in band gap and decrease in dielectric constant with increasing H concentration were explained by a decrease in

network connectivity as well as mass/electron density. An increase in disorder, as measured by the parameters E_U and $B^{1/2}$, with increasing H concentration was explained by the release of strain in the network and associated decrease in structural disorder. All of these correlations in a-B_xC:H_y were found to be very similar to those observed in amorphous hydrogenated silicon (a-Si:H), which suggests parallels between the influence of hydrogenation on their material properties and possible avenues for optimization.

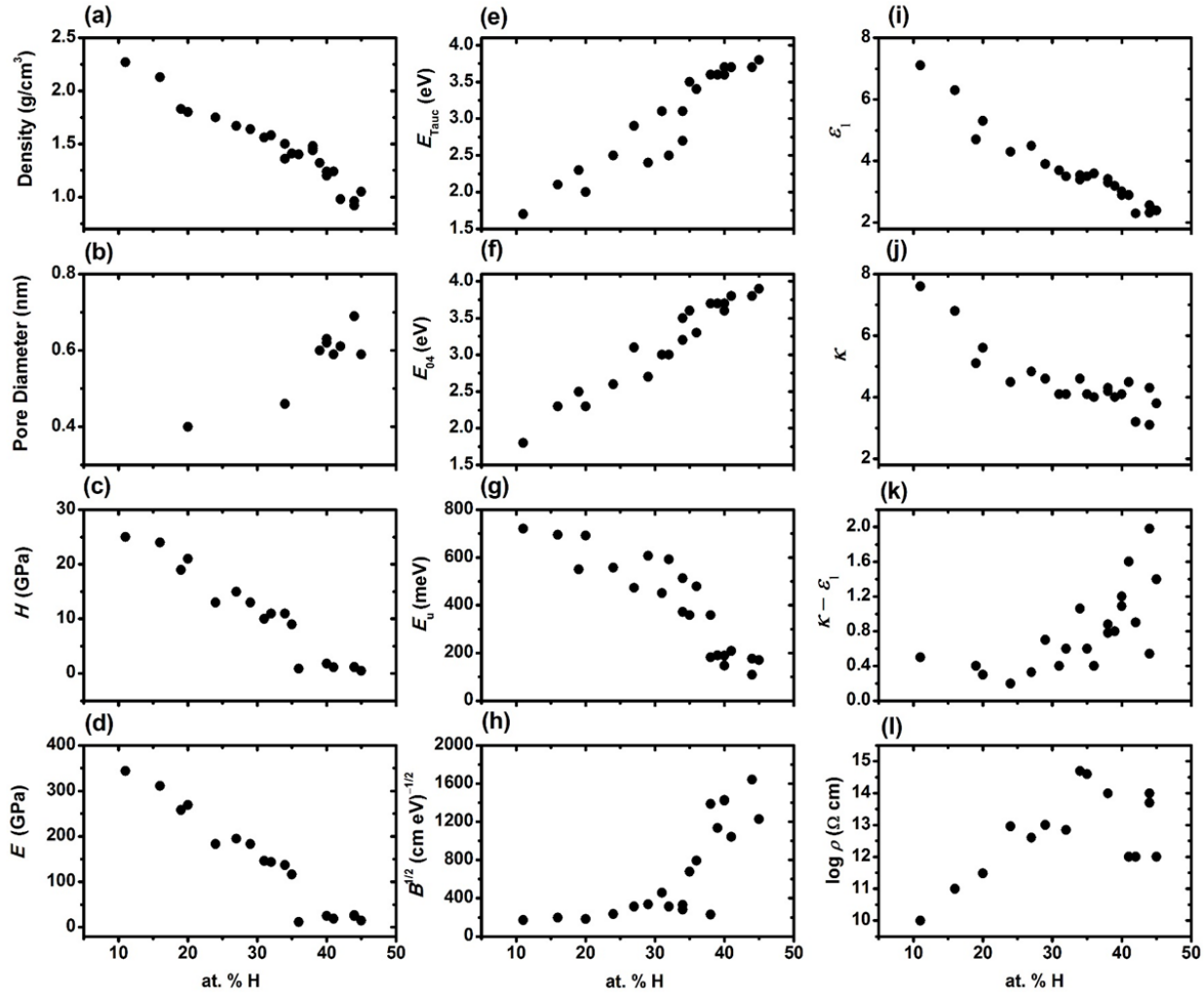


Figure 2. Correlations between a series of material properties and atomic concentration hydrogen in a-B_xC:H_y films: (a) density, (b) pore diameter, (c) hardness (H), (d) Young's modulus (E), (e) Tauc optical band gap (E_{Tauc} , $n = 2$), (f) E_{04} optical band gap, (g) Urbach energy (E_U), (h) Tauc slope parameter ($B^{1/2}$, $n = 2$), (i) high-frequency dielectric constant (ϵ_1), (j) total (low-frequency) dielectric constant (κ), (k) $\kappa - \epsilon_1$, and (l) electrical resistivity (ρ). [Figure from Nordell et al. JAP 118 (2015) 035703²³].

The second publication is based on a 2^5 full factorial experiment. This is an experiment in which all unique combinations of each of five process parameters at two levels, “low” and “high,” are tested, which allows for a statistically sound evaluation of both the effect of each parameter as well as any interactions between parameters, while minimizing the number of growths required. This study expanded upon the previous work looking at growth temperature and power, to include the effects of other major PECVD process parameters: pressure, total flow rate, and partial precursor flow rate. Ultimately, the films produced demonstrated a similar range of properties; however, from the results we were able to extract a more thorough understanding of the effects of process parameters on thin-film properties.

One of the important results highlighted in this publication was the wide range of growth rates possible, which extended from 1–112 (± 5) nm/min. Pressure and partial precursor flow rate were found to have the greatest effect on growth rate, with low pressure and high partial flow rate conditions yielding the highest growth rates; this can be explained by the higher delivery rate of reactive species to the substrate surface under these conditions. Power and total flow rate also demonstrated smaller, yet still statistically significant, effects. Temperature did not show any effect, which—combined with the above results—suggests that growth rate is primarily limited by mass transport rather than reaction rate. These results are important in the context of neutron detection, since higher growth rates are desirable toward producing relatively thick (50–100 μm vs $<1 \mu\text{m}$) a-B_xC:H_y films.

A second important result concerns the influence of growth conditions on thin-film properties. Hydrogen concentration and density were found to be influenced primarily by temperature and power, consistent with the previous study. However, the optical and electronic structure properties were found to be influenced not only by temperature, but also by a significant power*pressure interaction effect. As a result, the direction of the power effect depends on whether one is operating at high or low pressure and vice versa. Thus, two opposing growth regimes can be identified—high power and high pressure or low power and low pressure—which are both able to produce films with similar optical and electronic properties.

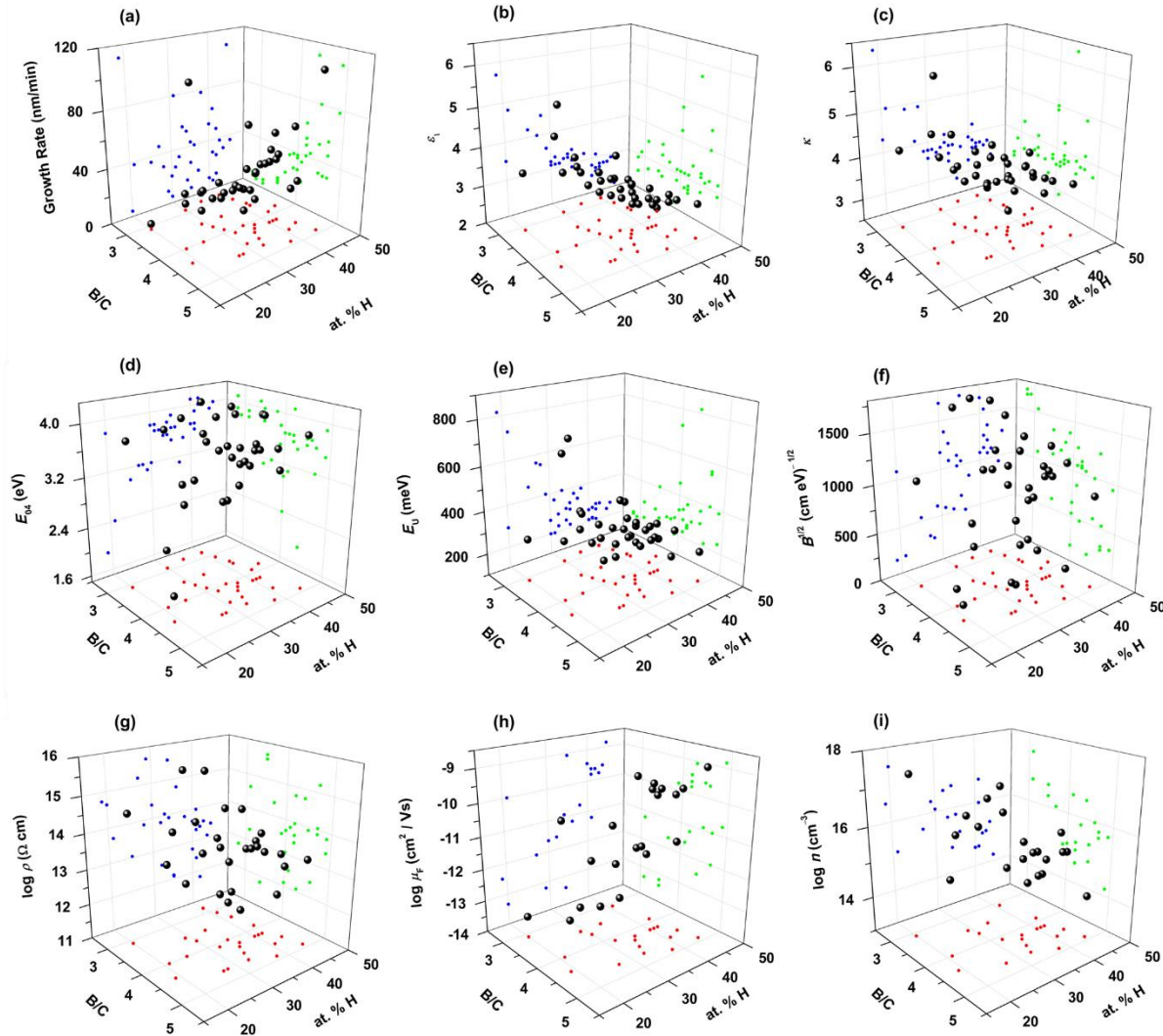


Figure 3. A series of properties in a-B_xC:Hy films vs atomic concentration hydrogen and B/C ratio: (a) growth rate, (b) high-frequency dielectric constant, ϵ_1 , (c) low-frequency (total) dielectric constant, κ , (d) band gap, E_{04} , (e) Urbach energy, E_U , (f) Tauc parameter, $B^{1/2}$, (g) electrical resistivity ($\log \rho$), (h) field-dependent mobility ($\log \mu_F$), and (i) charge carrier concentration ($\log n$). [Figure from [Nordell et al. \(2015\) submitted, MATCHEMPHYS-D-15-01944](#)].

A third result deals with a deeper look at carbon concentration, which was more variable in this second study. The metric reported, B/C ratio, was influenced by temperature, power, pressure, and the power*pressure interaction. Interestingly, it was found that B/C ratio correlated strongly to growth rate, but was completely independent from hydrogen concentration. Through an analysis of correlations between material properties (optical, electronic, electrical) and chemical

composition, it was found that the majority correlated strongly to atomic concentration hydrogen and weakly-to-moderately to B/C ratio (Figure 3). Thus, although H concentration (i.e., network connectivity/density) appears to be the strongest determiner of electronic and optical properties, the C concentration still has some effect. In fact, all of the optical and electronic structure parameters investigated showed the best correlation to a combined parameter, the product of at.% H and B/C ratio. Unexpectedly, the charge transport properties did not show a clear correlation with electronic structure, which suggests that the mechanism cannot be explained by a simple model such as multiple trapping. This will be discussed further in Section 4.4.

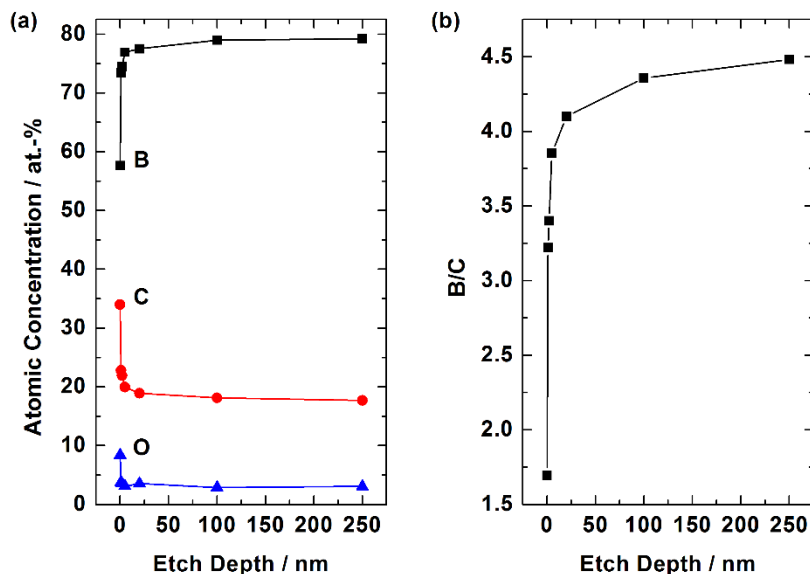


Figure 4. (a) X-ray photoemission spectroscopy depth profile data for a low-density film ($\text{B}_{4.3}\text{CO}_{0.9}:\text{H}_{4.8}$, $1.1 \text{ g}/\text{cm}^3$). (b) B/C ratio as a function of etch depth obtained from data in (a).

The third publication describes the effect of annealing time on B/C ratio, at.% H and density in a- $\text{B}_x\text{C:H}_y$ films, where it is found that these properties continue to change over long annealing times (multiple hours) when annealed at 350°C . As such, the at.% H and at.% C decrease, while the density increases. Additionally, this publication describes the results of an XPS depth profile study on a- $\text{B}_x\text{C:H}_y$ films (Figure 4), which leads to two main conclusions: (1) that the oxide layer is constrained to the top few nm's of the film, even after the prolonged atmospheric exposure of a relatively low-density film, and (2) that an extended carbon gradient exists, where the surface is carbon rich with stoichiometry of $\sim\text{a-B}_3\text{C:H}_y$, and a stable “bulk” composition is not achieved until $>100 \text{ nm}$ into the film. The consequence of (2) is that the surface and bulk properties, which are

known to correlate to chemical composition, may differ, and that surface-sensitive characterization techniques (e.g., XPS), may not accurately reflect the character of the bulk.

4.2. Metal-to-a-BC:H Interface Studies

4.2.1. Cr, Ti, Al, and Cu

The electronic and chemical structure of the metal-to-a-B_xC:H_y interface was studied using valence band and core level X-ray and ultraviolet photoemission spectroscopies (XPS and UPS) for a series of low-work-function metals (Cr, Ti, Al, and Cu). These were chosen as they had comparable work functions to a-B_xC:H_y, with Cr in particular being a metal that had been used previously as a contact in studies of a-B_xC:H_y neutron detector devices. Films were grown as described in [Nordell et al. JAP 118 \(2015\) 035703](#)²³ with a growth temperature of 350 °C, power of 30 W, pressure of 200 mTorr, total flow rate of 36 sccm, and partial flow rate of 0.5. These growths were not deposited under ultra-strict oxygen mitigation conditions, and used research grade Ar gas without additional filters. The thermally treated sample was heated at 475 °C for 60 min. XPS and UPS measurements were first done on the a-B_xC:H_y films to determine atomic composition, work function, and valence band character. The films measured were found to have a composition of ~a-B₃C_{0.5}:H_y (~10% oxygen), work function of 4.7 eV, and valence band maxima of 0.8 eV. A band gap value of 2.4 eV was obtained via a Tauc analysis of optical absorption spectra. Two main studies were performed to investigate the extent of interfacial diffusion, new chemical species formed, and interfacial electronic structure (Figure 5).

- (i) A metal overlayer was evaporated onto a sputter-cleaned a-B_xC:H_y film to a given thickness, and core level and valence band photoemission spectra, sensitive to the top several nm's of the sample, were subsequently acquired. This process was repeated for metal thicknesses of 0.5, 1, 2, 5, 10, 150, and ~250 Å.
- (ii) A 5 Å thick metal overlayer was evaporated onto a sputter-cleaned a-B_xC:H_y film, and core level and valence band photoemission spectra were acquired first for the sample as-is, and then after 6, 12, and 18 min of Ar⁺ etching.

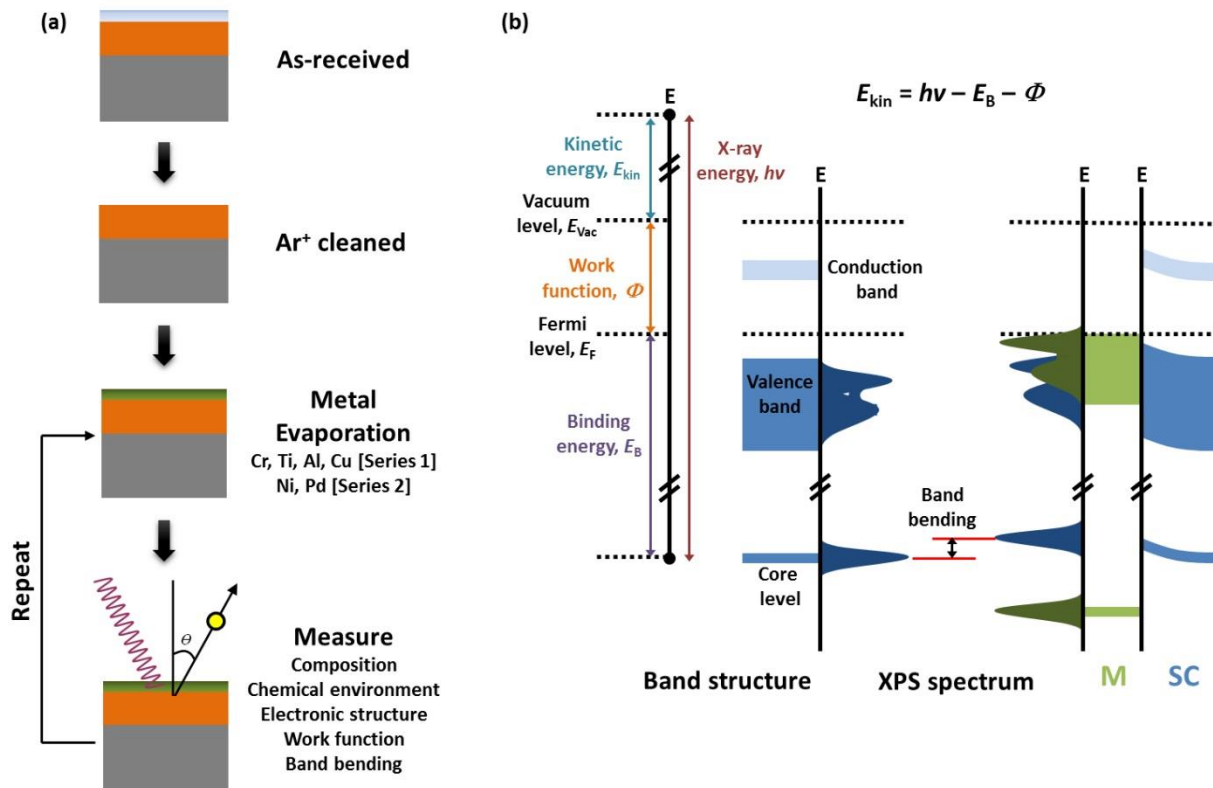


Figure 5. (a) Schematic of photoemission experiment conducted to study the metal-to-a-B_xC:H_y interface, and (b) representation of band bending analysis by monitoring core level shift.

Full details for these measurements and analyses are described in [Driver et al. JPCM 24 \(2012\) 445001](#).²⁴ The major conclusion was that Cr, Ti, and Al all formed interfacial oxides. These are anticipated to perturb the injection barrier and the local electric field at the interface. Cu, however, forms a clean metallic interface. Examples of metal core level spectral and valence band spectra for Cr and Cu are given in Figure 6 and Figure 7, respectively. Tentative band diagrams for each of the interfaces were proposed (Figure 8). Band bending was monitored by following the shift in B 1s core level energy as a function of metal overlayer coverage, and the shifts were generally consistent with those predicted for the metal or metal oxide interfaces.

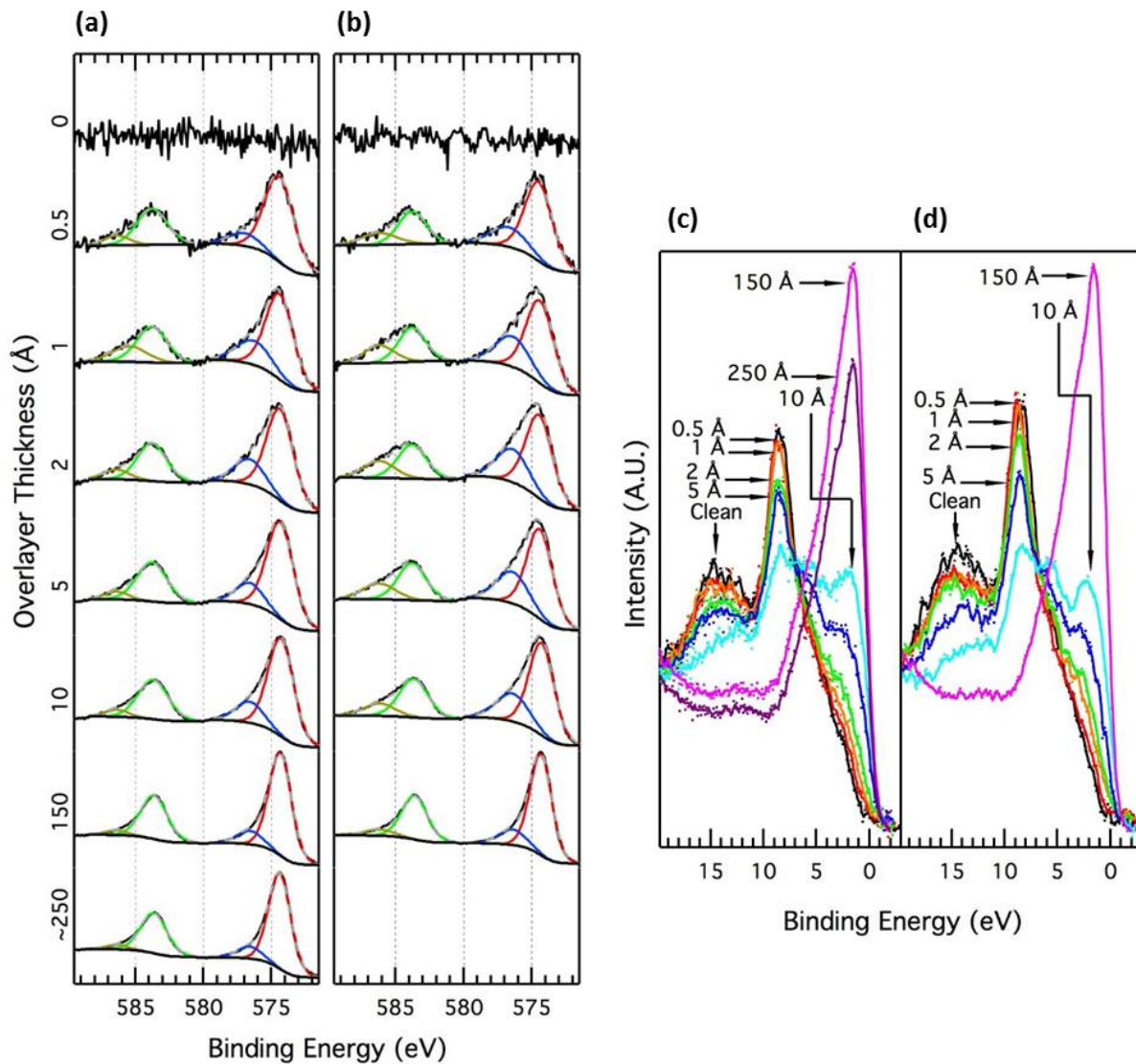


Figure 6. Cr 2p core level photoemission spectra [(a) as-deposited and (b) thermally treated] and valence band photoemission spectra [(c) as-deposited and (d) thermally treated] for a-B₃CO_{0.5}:H_y films with Cr overlayers as a function of overlayer thickness. [Figures from [Driver et al. JPCM 24 \(2012\) 445001²⁴](#)].

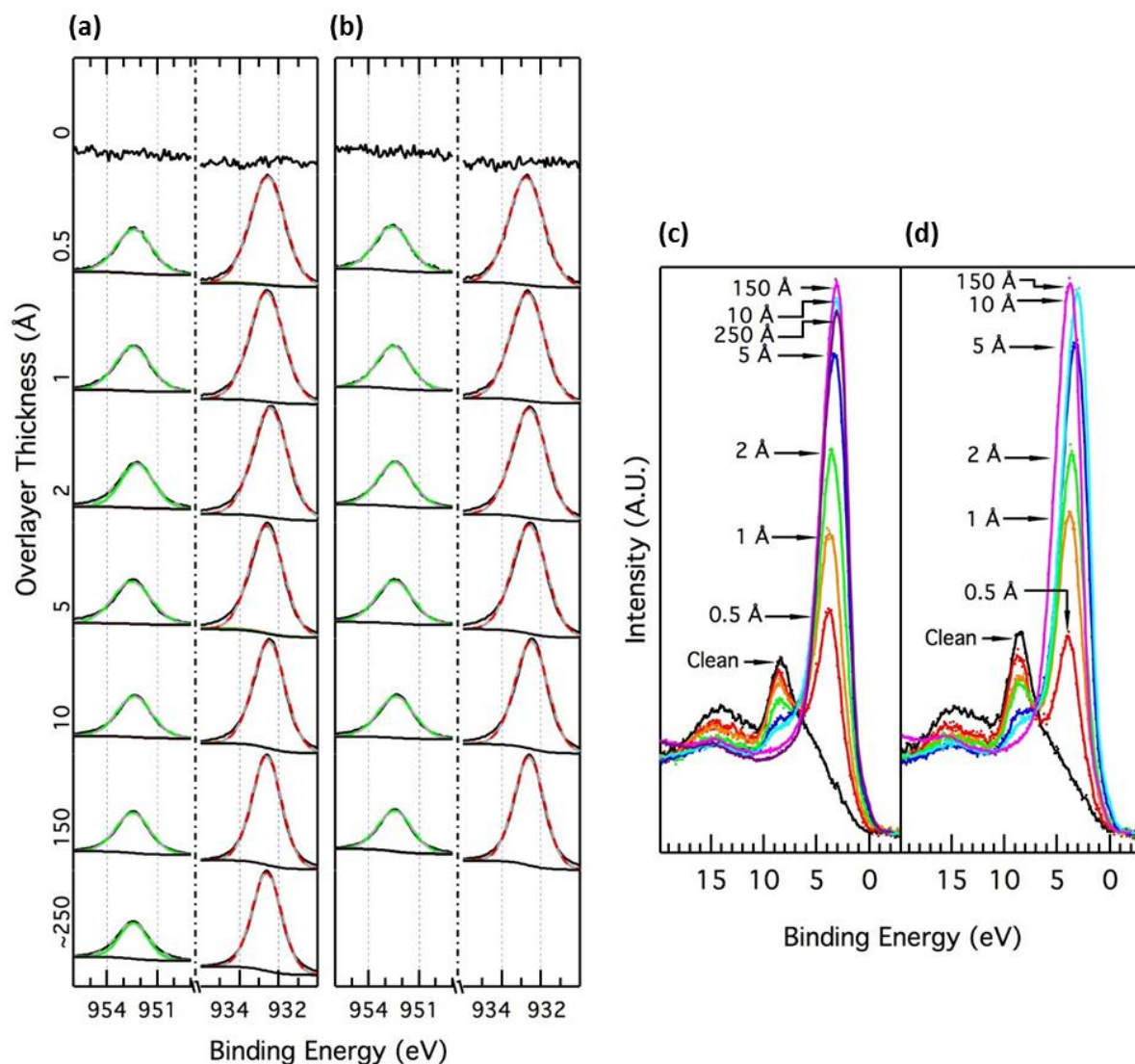


Figure 7. Cu 2p core level photoemission spectra [(a) as-deposited and (b) thermally treated] and valence band photoemission spectra [(c) as-deposited and (d) thermally treated] for a-B₃CO_{0.5}:H_y films with Cu overlayers as a function of overlayer thickness. [Figures from **Driver et al. JPCM 24 (2012) 445001**²⁴].

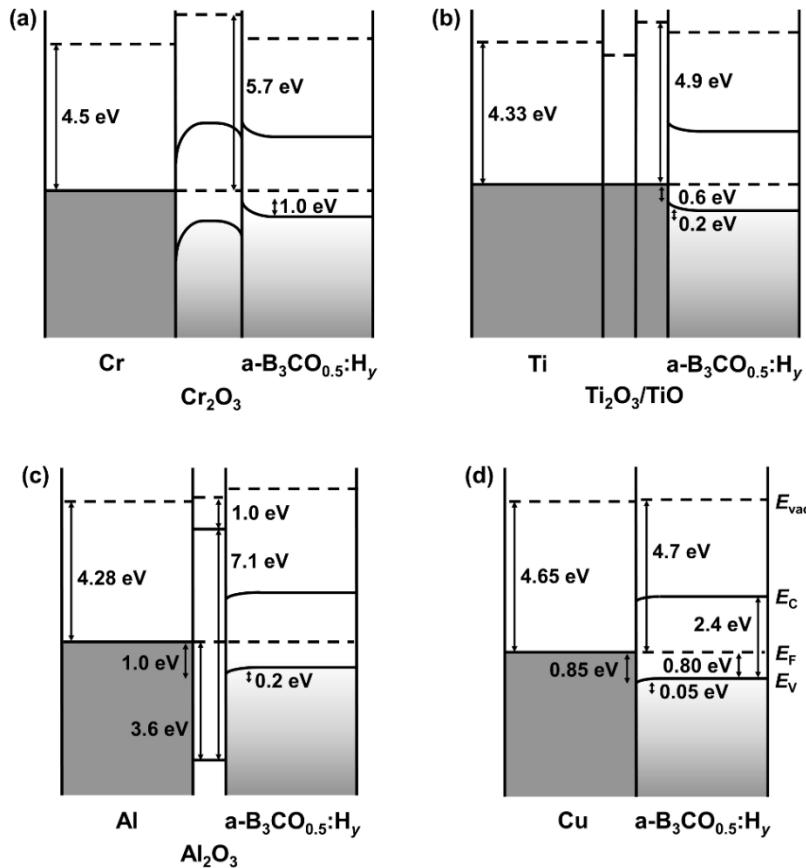


Figure 8. Band diagrams for the metal-to-a-B₃CO_{0.5}:H_y interface for Cr (a), Ti (b), Al (c), and Cu (d) taking into account interfacial oxide layers observed by XPS. [Figure from [Driver et al. JPCM 24 \(2012\) 445001²⁴](#)].

4.2.2. Ni and Pd

Based on the results from the first series of metals, additional metals were chosen that had higher work functions such that a lower barrier to hole injection and higher barrier to electron injection could be achieved. Specifically, we elected to test Ni (work function of 5.15 eV) and Pd (work function of 5.12 eV).²⁵ Metal overlayer experiments were performed in a similar fashion as for the previous series of metals. The overlayers of Ni were applied to a film of composition a-B_{4.1}CO_{0.3}N_{0.2}:H_y (i.e., 6 at.% O and 3 at.% N), which had been Ar-ion-etched for 2 h to remove ~20 nm of material. The Ni 2p core level spectra were deconvoluted into six peaks to model its complex satellite structure (Figure 9), as per Grosvenor et al.²⁶ The spectrum at 10 Å coverage appears identical to that of metallic Ni, both in terms of energy and peak envelope, with the main peak falling at 852.6 eV, identical to the literature value.^{26,27} Reported energies and peak envelopes for nickel oxides are quite distinct from those of metallic Ni.^{28,29} At lower coverages, the Ni 2p

core level peak is shifted to slightly higher energies (e.g., 853.4 eV at 2 Å coverage). However, no evidence for the presence of NiO, with an expected peak maximum at 854.0 eV and a prominent shoulder at ~856 eV, is observed. In addition, no evidence for NiO is observed from the O 1s spectrum in the form of a diagnostic peak at 529.6 eV; the spectrum looks identical to that typically observed for a-B_xC:H_y films with a small amount of oxygen contamination.

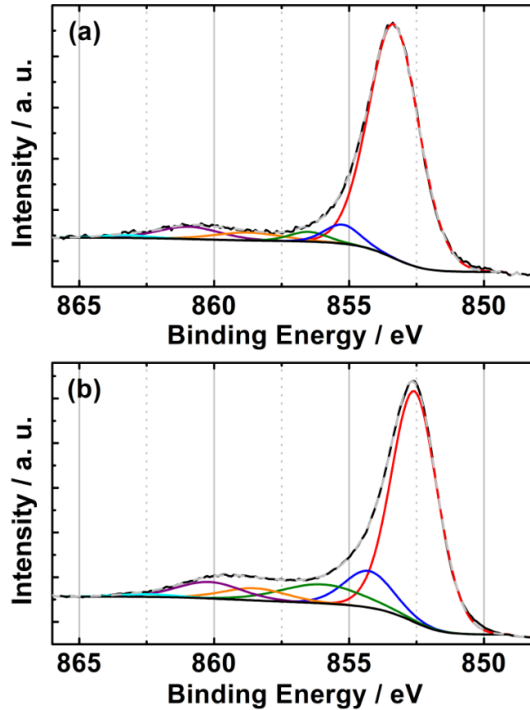


Figure 9. Ni 2p core level photoemission spectra for an a-B_{4.1}CO_{0.3}N_{0.2}:H_y film with 2 Å (a) and 10 Å (b) Ni overlayers.

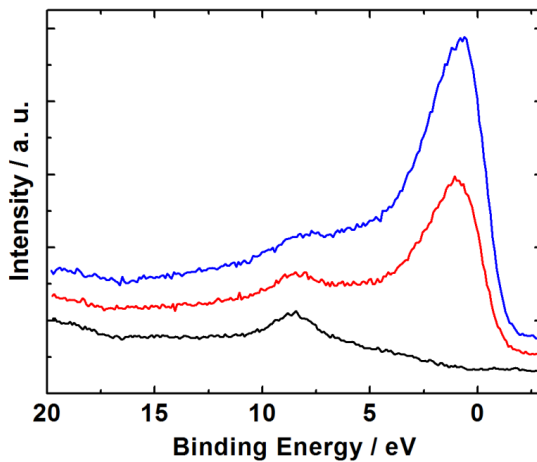


Figure 10. Valence band photoemission spectrum for an a-B_{4.1}CO_{0.3}N_{0.2}:H_y film with 0 Å (bottom trace, black), 5 Å (middle trace, red), and 10 Å (top trace, blue) of Ni.

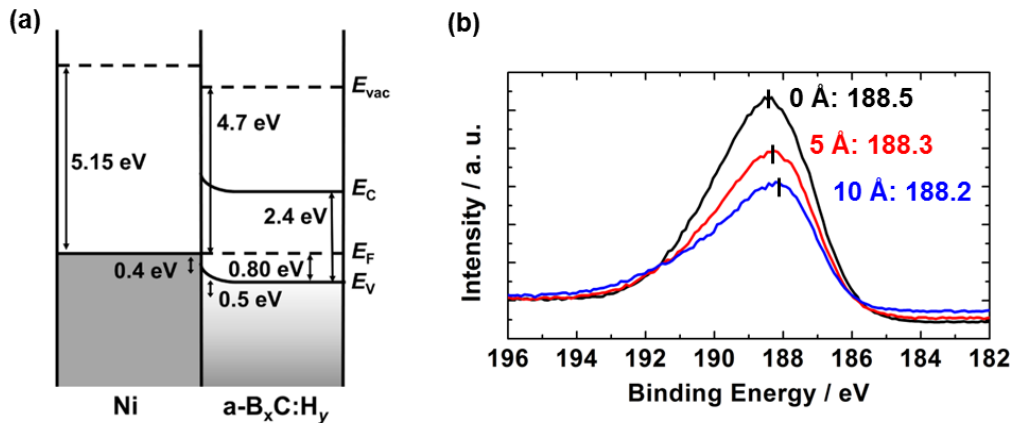


Figure 11. (a) Band diagram for a clean Ni-to-a-B_{4.1}CO_{0.3}N_{0.2}:H_y interface. (b) B 1s core level photoemission spectrum displaying shift in peak maximum from 188.5 eV at 0 Å coverage to 188.2 eV at 10 Å coverage.

The valence band spectrum (Figure 10) is also diagnostic of metallic Ni being formed immediately at the a-B_{4.1}CO_{0.3}N_{0.2}:H_y-to-nickel interface.³⁰ A tentative band diagram for a clean a-B_{4.1}CO_{0.3}N_{0.2}:H_y-to-Ni interface is given in Figure 11(a). Because the work function of Ni (5.15 eV) is slightly higher than that of amorphous hydrogenated boron carbide (4.7 eV), an accumulation-type contact is expected (desirable for hole transport from the semiconductor to the metal) with a low Schottky barrier. A small shift in the energy of the B 1s core level from 188.5 eV at 0 Å coverage to 188.2 eV at 10 Å coverage [(Figure 11(b))] is consistent with the expected direction of band bending, and therefore supports this model.

The relative atomic concentrations of B, C, O, N, and Pd in the sampled layer for an a-B_{4.1}CO_{0.3}N_{0.2}:H_y film with palladium overlayers were determined. Because the Pd 3p3/2 and O 1s core level peaks overlap, the quantification of oxygen requires the deconvolution of the two; palladium may be quantified via the Pd 3d level. The results are shown in Figure 12. As Pd overlayers are applied, the concentration of Pd increases while that of B decreases, as expected, but importantly, the concentration of O increases relative to that in the bulk. This behavior is similar to that observed in the cases of Cr, Ti, and Al overlayers on a-B_xC:H_y, which formed interfacial metallic oxides, suggesting that a similar phenomenon is occurring for Pd. Indeed, in the Pd 3d core level spectrum [Figure 13(a) and (c)], at 0.5 Å coverage, palladium monoxide (PdO, Pd²⁺) spectral contributions make up ~85% of the total peak area, with another ~10% assigned to

PdO_2 (Pd^{4+}), and <5% to metallic Pd^0 .³¹ At higher coverages, an increased contribution from metallic Pd is observed in the Pd 3d spectrum, reaching ~65% by 20 Å coverage [the remaining ~35% originating from PdO (~30%) and PdO_2 (<5%)]. An accurate analysis of contributions to the O 1s core level spectrum is impeded by the existence of at least five different components at nearly the same energy (O 1s B–O, O 1s C–O, O 1s PdO , Pd 3p3/2 Pd^0 , and Pd 3p3/2 Pd^{2+}). Interestingly, in the B 1s spectrum [Figure 13(b) and (d)], as overlayers are applied, a distinct peak at ~193 eV appears. While it is common to observe a peak at 190–191 eV in the B 1s spectrum of a- $\text{B}_x\text{C:H}_y$ films with oxygen contaminants, which we have assigned to boron suboxides ($\text{B}^{1+}/\text{B}^{2+}$), the peak at 193 eV has not previously been observed for any of the a-BCO:H films we have grown, nor at the a-BCO:H-to-metal interface for any of the metals studied (including Cr, Ti, Al, Cu, and Ni) and can be assigned to boron oxides in the 3+ oxidation state, namely B_2O_3 or H_3BO_3 .^{32,33} It is possible that Pd uniquely catalyzes a boron oxidation reaction.

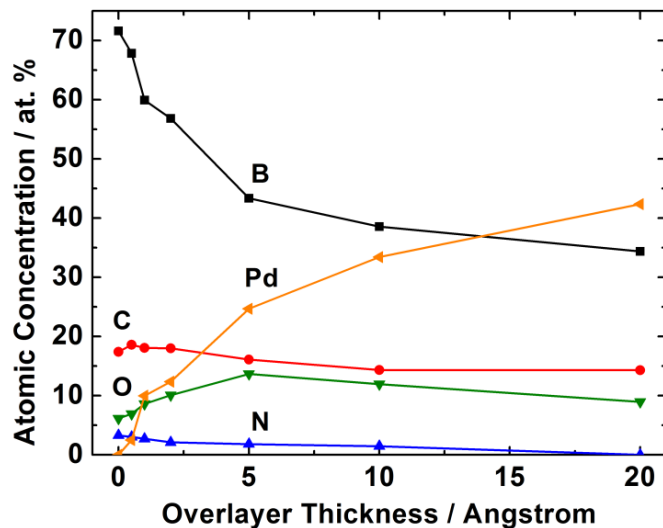


Figure 12. Relative atomic concentrations of B, C, O, N, and Pd (at.%) in the sampled layer (i.e., the top several nm's of the sample) determined from normalized XPS core level spectral intensities (for the B 1s, C 1s, O 1s, N 1s, and Pd 3d core levels) for an a- $\text{B}_{4.1}\text{CO}_{0.3}\text{N}_{0.2}:\text{H}_y$ film with Pd overlayers as a function of overlayer thickness.

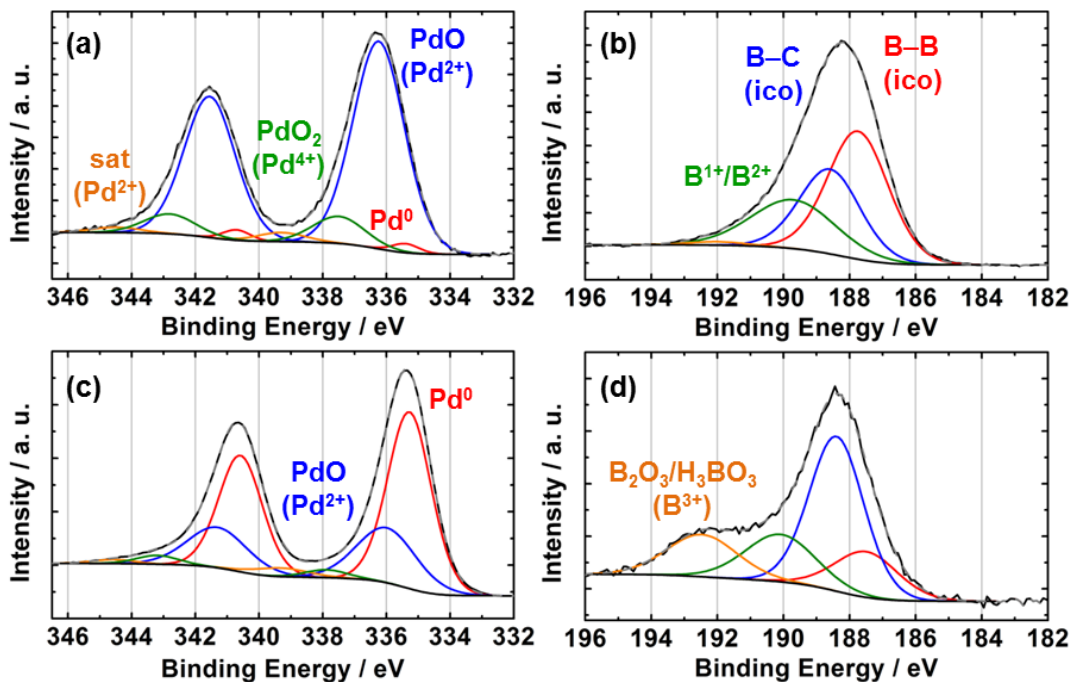


Figure 13. Pd 3d and B 1s core level photoemission spectra for an a-B_{4.1}CO_{0.3}N_{0.2}:H_y film with Pd overlayers at 0.5 Å coverage [(a) and (b), respectively] and at 20 Å coverage [(c) and (d), respectively].

The formation of PdO at the immediate a-B_{4.1}CO_{0.3}N_{0.2}:H_y-to-Pd interface is corroborated by the valence band spectrum (Figure 14), wherein the maximum for the Pd 3d peak shifts from ~2.6 eV at 0.5 Å coverage, diagnostic of the formation of PdO at low coverages, to ~1.6 eV at 20 Å coverage, diagnostic of metallic Pd at thicker coverages.^{34,35} A tentative band diagram for an a-BCO:H-to-Pd interface with an interfacial PdO layer is given in Figure 15. Little information is available in the literature regarding the electronic structure of PdO. A work function of 5.9 eV and band gap of ~1 eV were used to construct the diagram,^{34,36} although it must be noted that these values are not rigorously established. Assuming they are adequate estimates, it may be concluded that the PdO layer will lead to significant band bending and space-charge region formation in the a-B_xC:H_y layer. It is possible, given that the PdO layer is relatively thin (1–2 nm) and that PdO is a narrow-band-gap semiconductor, that its presence will not significantly impede charge transport at the junction. As regards an experimental determination of band bending through photoemission spectroscopy, no shift was observed for the B 1s core level, which suggests that band bending may be much less than implied in Figure 15.

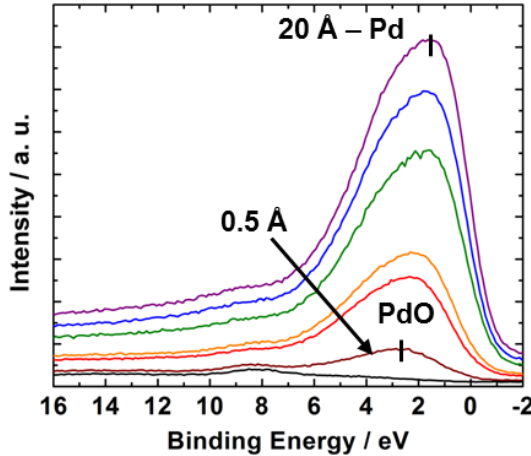


Figure 14. Valence band photoemission spectrum for an $a\text{-B}_{4.1}\text{CO}_{0.3}\text{N}_{0.2}\text{:H}_y$ film with Pd overlayers as a function of overlayer thickness (0, 0.5, 1, 2, 5, 10, 20 Å).

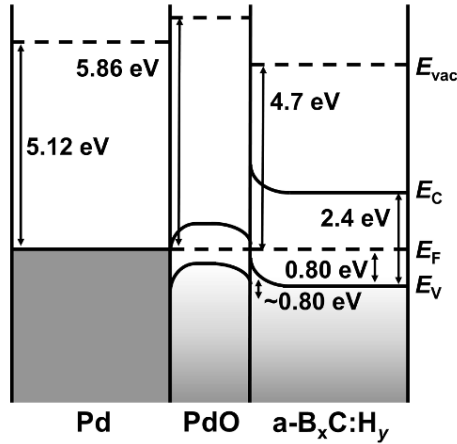


Figure 15. Band diagram for a Pd-to- $a\text{-B}_{4.1}\text{CO}_{0.3}\text{N}_{0.2}\text{:H}_y$ interface with an interfacial PdO layer.

In summary, Ni appears to form a clean interface to $a\text{-B}_{4.1}\text{CO}_{0.3}\text{N}_{0.2}\text{:H}_y$, with no evidence for the formation of new chemical species. On the basis of band alignment predictions, and consistent with experimentally observed band bending, Ni would be expected to make a good ohmic contact to $a\text{-B}_x\text{C:H}_y$, similarly to Cu. Palladium, on the other hand, forms a thin interfacial oxide layer, made up predominantly of PdO. A band diagram for the oxidized Pd-to- $a\text{-B}_x\text{C:H}_y$ interface is proposed, though it is uncertain whether this layer will prove advantageous or disadvantageous for charge transport at the junction due to the scarcity of electronic structure information for PdO.

4.2.3. Metal–Insulator–Metal Heterostructure Characterization

Metal–insulator–metal (MIM) heterostructures were fabricated to determine whether a given metal formed an ohmic junction to a-B_xC:H_y. This may be evaluated through an analysis of the *I*–V behavior of the heterostructure, which, if ohmic, will be linear (i.e., obey Ohm’s law, $I = V/R$). MIM heterostructures were fabricated successfully using various combinations of Cu, Al, Ti, and Pd contacts. The fabrication of Ni/a-B_xC:H_y/Ni heterostructures was unsuccessful due to the a-B_xC:H_y films consistently delaminating from the base evaporated Ni layer. The fabrication of Cu/a-B_xC:H_y/Ti heterostructures was also unsuccessful due to the delamination of Ti from the a-B_xC:H_y. Additional work on adhesion layers may be needed to further develop these metals as contacts.

Current–voltage measurements were completed in ‘loops’ in order to investigate a possible hysteresis effect. The current was thus measured from 0 V → x V → $-x$ V → 0 V, where x was varied from low to high voltage (0.5, 1, 2, 5, 10, 15, 20 V) until erratic behavior was observed. For each voltage range, three full cycles were measured to verify electrical stability.

I–V curves for a series of devices are shown in Figure 16: Cu/a-B_xC:H_y/Cu, fabricated entirely *in situ* (a); Cu/a-B_xC:H_y/Cu, with the bottom contact exposed to atmosphere (b), Cu/a-B_xC:H_y/Pd, with the bottom contact exposed to atmosphere (c), and Al/a-B_xC:H_y/Al, again with the bottom contact exposed to atmosphere (d). It can be seen that the devices containing different metal contacts, fabricated both *in situ* and *ex situ*, display similar curve shapes and current magnitudes (within the same order of magnitude); the differences are subtle. All of the curves display hysteresis, and all appear to display linear behavior ($I \propto V$) at low voltages/fields, and curvature ($I \propto V^{n>1}$) at higher voltages/fields (see Section 4.3.1 for a more detailed discussion of *I*–V behavior). In comparing Cu/a-B_xC:H_y/Cu devices fabricated *in situ* and *ex situ* [(a) and (b)], the devices exhibit very similar behavior; and in fact, the device prepared partially *ex situ* appears to display ‘cleaner’ behavior (i.e., the current overlaps at each voltage range). The Al/a-B_xC:H_y/Al device (d), expected to possess an insulating Al₂O₃ interfacial layer due to *ex situ* preparation, also shows very similar behavior (except that it breaks down above 10 V), which suggests that charge can easily tunnel through the oxide barrier. We have additionally tested MIS heterostructures, with Si as the semiconductor, and in some cases a temporary mercury contact (using a Hg probe) as the metallic electrode. A comparison of *I*–V traces is shown in Figure 17, where Cu/a-B_xC:H_y/Cu, Si/a-B_xC:H_y/Hg (with both degenerate and 1–15 Ω·cm Si), and Si/a-B_xC:H_y/Cu heterostructures all

exhibit relatively similar I - V behavior. Ohmic behavior has also been observed in Cu/a-B_xC:H_y/Ti/Cu, Cu/a-B_xC:H_y/oxide/Pd (a-B_xC:H_y exposed to atmosphere before deposition of top contact), Pd/a-B_xC:H_y/Pd, and ITO (indium tin oxide)/a-B_xC:H_y/ITO heterostructures.

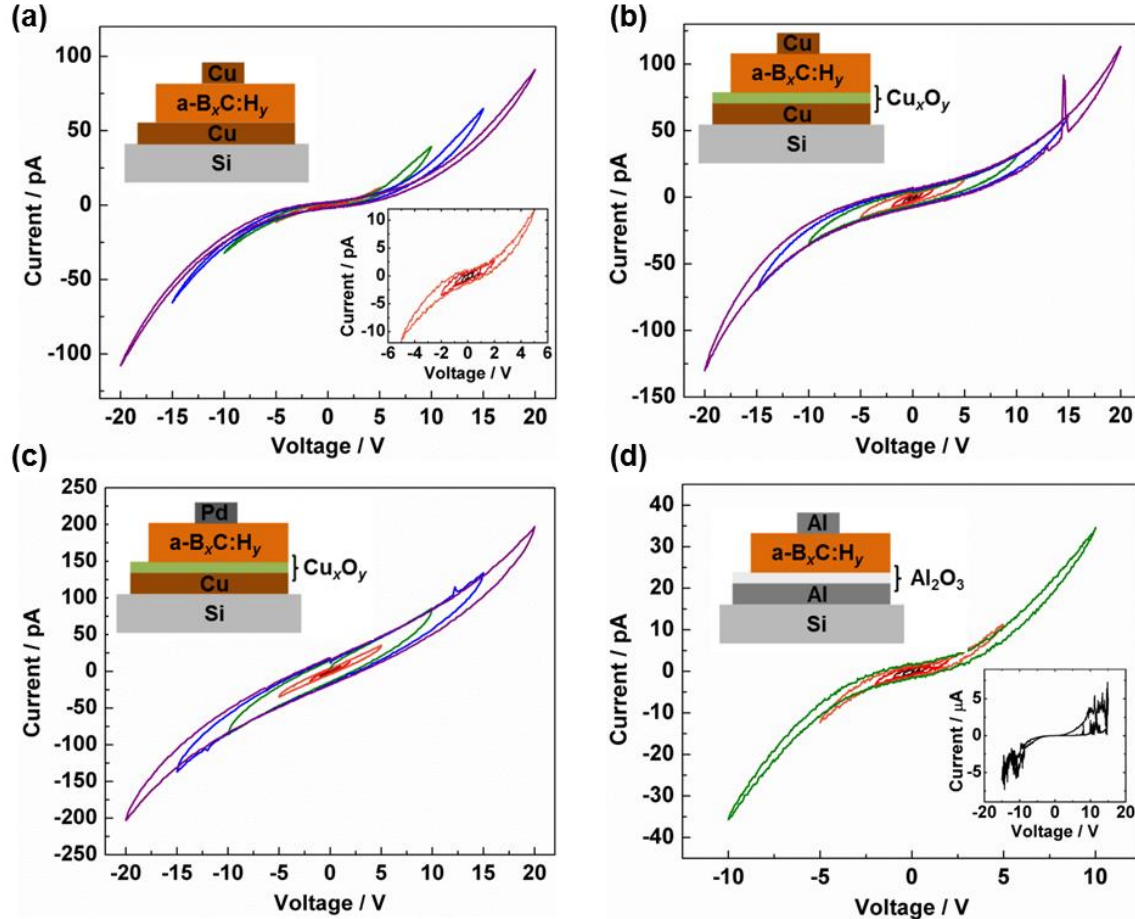


Figure 16. I - V curves for four different a-B_xC:H_y-based metal–insulator–metal devices showing the effects of different metals and *in situ* vs *ex situ* processing.

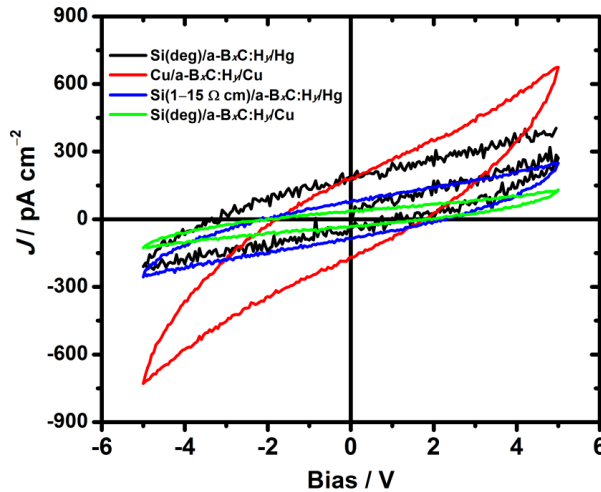


Figure 17. I - V traces for four different $a\text{-B}_x\text{C:Hy}$ MIM heterostructures.

Overall, we conclude that the contact type, which includes the possibility of a metal or a semiconductor (e.g., Si) with or without the presence of an interfacial oxide layer, does not have a significant effect on the general I - V behavior of the devices at low/moderate fields. This does not necessarily mean that the contact does not have any effect on the device performance. At very high fields, the injection mechanism may change from ohmic to schottky, where the electric field leads to an increase in barrier while necessitating greater current injection to sustain ohmic-based transport. The reason for this is two-fold: (1) the extremely high resistivity of $a\text{-B}_x\text{C:Hy}$ implies that very little charge injection is needed to supply sufficient current to the device. Thus, even in the presence of a barrier, ohmic injection is sustained with very little charge injection; and (2) the amorphous nature of $a\text{-B}_x\text{C:Hy}$, which leads to the presence of band tails consisting of localized tail states presents the possibility of charge injection via the more accessible mid-gap states rather than via the conduction/valence band alone.

4.2.4. Summary

The tendency to form metallic oxides at the metal-to- $a\text{-B}_x\text{C:Hy}$ interface suggests that oxygen levels in $a\text{-B}_x\text{C:Hy}$ films will play an important role in device performance, not only in affecting the bulk $a\text{-B}_x\text{C:Hy}$ properties, but also in modifying heterostructure interfaces. The incorporation of oxygen into $a\text{-B}_x\text{C:Hy}$ films during growth is ubiquitous, consistent with the strong oxygen-gettering tendencies of boron carbide. We hypothesize that bulk oxygen will remain an issue even with lower oxygen concentrations (3–5%), which are usually still present in films with the lowest

oxygen content. If a non-oxygen-gettering metal contact is required, Cu or Ni are viable options. Although interfacial oxides will very likely have some sort of effect on heterostructure performance, in terms of gross I - V behavior, these appear to have little influence on the low-field ohmic injection mechanism observed in the case of the majority of the MIM heterostructures measured. The ease of forming ohmic contacts for a- $B_xC:H_y$ has been rationalized in terms of its high resistivity and the presence of localized mid-gap states arising from its amorphous structure.

4.3. Charge Transport Measurements

4.3.1. Mobility Measurements

Measuring mobility in low-mobility materials is a nontrivial task.³⁷ Not only is the concept of a precise mobility value nebulous due to the fact that mobility is dependent on experimental conditions (e.g., device thickness, electric field) and ultimately on the distribution of charge carriers within the density of states over the course of the experiment (and therefore the portion of the density of states in which the mobility is being probed),³⁸ but experiments devised to measure mobility all necessitate that a different specific set of requirements be met in order to ensure accuracy—oftentimes these requirements cannot easily be tested and can only be assumed.³⁹ A recent paper by Blakesley et al. demonstrating the wide variability in mobility values calculated for the same materials serves as a cautionary note.³⁷

Of the methods available for measuring mobility, drift-mobility-based methods are particularly suitable for high-resistivity (low-mobility) solids, as they ultimately scale with transit time, which increases with decreasing mobility and thus becomes easier to measure. In contrast, in Hall methods, the Hall voltage decreases with decreasing mobility, and renders measurements increasingly challenging. By measuring the transit time, t_{tr} , of charge carriers through a material, mobility can be extracted through the relationship of t_{tr} to drift velocity, v , which is in turn related to mobility, as per Equation 1, where d represents film thickness and E , electric field.

$$t_{\text{tr}} = \frac{d}{v} = \frac{d}{\mu E} \quad [1]$$

While the light-based time-of-flight (TOF) method may be the most commonly applied drift-mobility method, the transient (or dark-injection) space-charge-limited current (DI-SCLC) method presents several advantages in our case, including the use of injecting contacts, thinner films, and

greater compatibility with dispersive transport. A short list of additional mobility determination techniques for high-resistivity/low-mobility materials includes charge extraction by linearly increasing voltage (CELIV), impedance/admittance spectroscopy, field effect transistor methods, and steady-state space-charge-limited current (SS-SCLC) methods.³⁹ Blakesley et al.³⁷ argue that for benchmarking purposes, the steady-state space-charge-limited current method is the optimum choice, but this may simply be due to its relative simplicity and ease of standardization (precision) rather than its accuracy. Weiß et al.⁴⁰ argue that the corollary DI-SCLC method is superior in terms of determining absolute values, as it measures the drift mobility more directly via a direct measure of transit time and does not involve the ambiguity related to trapping inherent in SS-SCLC analyses. Ultimately, however, there are so many unknowns (e.g., dominant charge carrier, density of states, trap profile, etc.), particularly when dealing with a complex material such as a-B_xC:H_y that has been minimally studied, that the use of a series of methods should provide the most information regarding the validity and advantages/disadvantages of the different techniques. Both steady-state and transient SCLC techniques have been applied to a-B_xC:H_y samples.

The complete theory, results, and analysis of this work is described in detail in the following thesis:

- Christopher L. Keck, ‘Electrical Carrier Mobility Measurements of Amorphous Hydrogenated Boron Carbide Using Space-Charge-Limited Current Techniques,’ M.Sc. Thesis, University of Missouri-Kansas City (2015).
[\[https://mospace.umsystem.edu/xmlui/handle/10355/46545\]](https://mospace.umsystem.edu/xmlui/handle/10355/46545)

4.3.1.1. Steady-State Space-Charge-Limited Current

In an insulating solid, we expect to observe space-charge-limited current effects.⁴² When an electric field is applied to an insulator or semi-insulator sandwiched between conducting electrodes, ohmic behavior ($I \propto V$) will typically be observed at low field. In this regime, the contact is supplying sufficient charge to replace that within the solid. In this scenario, a contact may be referred to as ‘injecting’ or ‘ohmic,’ which does not necessarily imply good band lineup or accumulation layer formation (typical markers of injecting/ohmic contacts), but rather a low contact resistance relative to bulk resistance, which is a much easier requirement to meet in the case of a high-resistivity solid. As the electric field is increased, the I - V behavior begins to take on a superlinear relationship with $I \propto V^2$ [Figure 18(a)]. At this point, injected charge accumulates

within the insulator adjacent to the electrode faster than it can be transported through the device, causing a buildup of space charge and modification of I - V dependence, which now follows Child's law:

$$J_{SCLC} = \frac{9}{8} \mu \epsilon \frac{V^2}{d^3} \quad [2]$$

where $\epsilon = \epsilon_0 \epsilon_r$, with ϵ_0 representing the absolute permittivity of free space and ϵ_r the relative dielectric constant of the material. The distinct transition between ohmic and SCLC transport regimes can be understood as the field at which dielectric relaxation time, τ_d ($= \epsilon/\sigma$), which effectively allows for neutralization of excess injected charge, becomes longer than the transit time, t_{tr} ($= d/v = d/\mu E$) (t_{tr} in Figure), which becomes shorter with increasing electric field proportionally to mobility [Figure 18(b)].⁴¹ The presence of the mobility term in Child's law allows for a determination of this property from a fitting of the I - V (or J - V or J - E) curve within the SCLC regime. The downfall of this method is that Child's law assumes a perfect solid with no trapping as well as field-independent mobility, which are both not the case in the majority of insulators, particularly those exhibiting disorder. Corrections to the expression to account for trapping and for field-dependent mobility exist, but traditional treatments are still oversimplifications.⁴³ Aware of the limitations of the model, we have opted to apply the Murgatroyd⁴⁴ treatment which takes into account the field-dependent mobility:

$$\mu_F = \mu_0 \exp(\gamma \sqrt{E}) \quad [3]$$

and approximates SCLC current density, J_{SCLC} , as:

$$J_{SCLC} = \frac{9}{8} \mu_0 \epsilon \frac{V^2}{d^3} \exp\left(0.89\gamma \sqrt{\frac{V}{d}}\right) \quad [4]$$

where μ_0 represents the limit of mobility at zero electric field and γ describes its field-dependence. While the field dependence cannot account for all trapping profiles, it can approximate shallow trapping effects. We have applied the protocol outlined by Blakesley et al.³⁷ in the hopes of, if not obtaining 100% accurate mobility values, at least obtaining consistent and precise mobility values that can be compared to each other, and to others reported in the literature obtained by a similar protocol. It is reasonable to assume that the mobility thus obtained can represent a lower limit on this property.⁴⁰

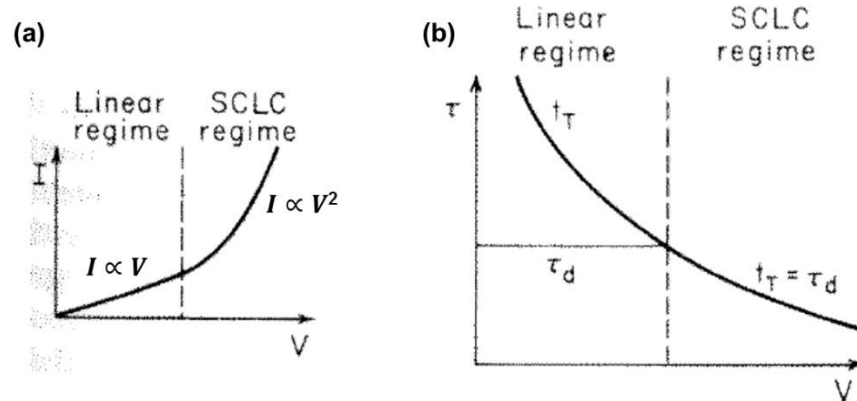


Figure 18. (a) Ohmic and SCLC I - V regimes; and (b) distinction between regimes as a function of transit time and dielectric relation time constant (adapted from ref⁴¹).

Steady-state current–voltage traces were obtained on two types of heterostructures, Cu/aB_xC:H_y/Cu and Si/a-B_xC:H_y/Hg (Hg represents a temporary mercury contact), which both demonstrate very similar I - V curves. The advantage of Hg probe measurements is the ease of fabricating simple thin-film Si/a-B_xC:H_y heterostructures relative to MIM sandwich devices, and therefore the possibility of high throughput for property correlations. Voltage is typically varied cyclically from 0 V → x V → $-x$ V → 0 V, while increasing voltage limits, x , in increments until erratic behavior is observed, and repeating each cycle three times to allow the device to stabilize and ensure reproducibility. As observed in Figure 19, the I - V curves exhibit hysteresis, hypothesized to be caused by charge trapping/detrapping which induces a displacement current due to changing capacitance in addition to the expected resistive current.^{45–47} The nonlinearity of the I - V curves is consistent with SCLC effects:¹⁵ a log–log plot of the data (Figure 20) highlights two relatively linear regions with $I \propto V^n$ with $n = 1$ (ohmic) and $n = 2$ (SCLC).

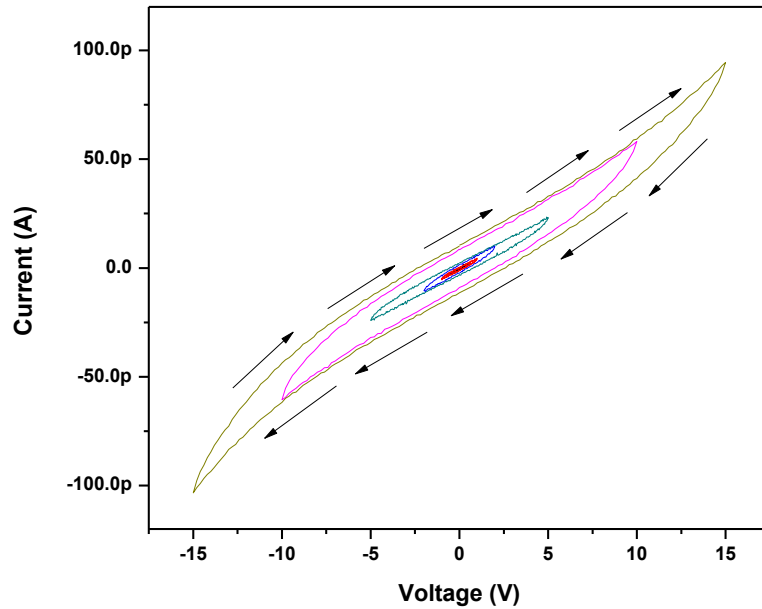


Figure 19. Example *IV* plot of an $a\text{-B}_x\text{C:}\text{H}_y$ MIM test device displaying hysteresis. [Figure from [Keck M.Sc. Thesis \(2015\)](#)].

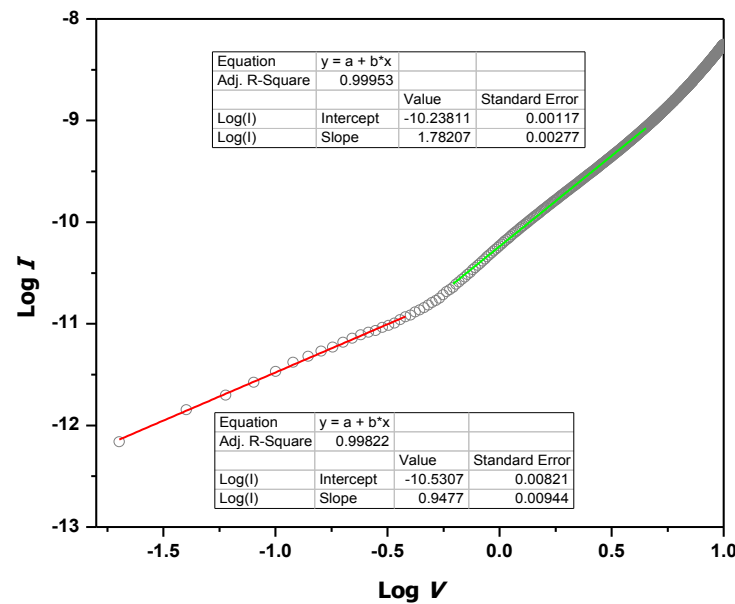


Figure 20. Example log–log *IV* plot for a $\text{Hg}/a\text{-B}_x\text{C:}\text{H}_y/\text{Si}$ test device (N4) demonstrating two distinct linear regions. A linear fit to the low-field region yields a slope of 0.95, consistent with ohmic behavior. A linear fit to the higher-field region yields a slope of 1.8, consistent with SCLC behavior. [Figure from [Keck M.Sc. Thesis \(2015\)](#)].

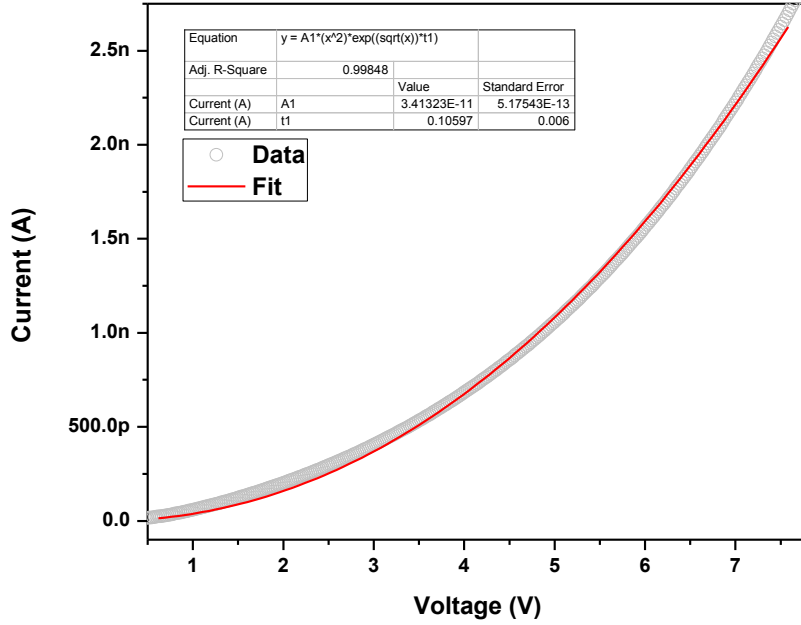


Figure 21. Fit of the SCLC region from the data shown in Figure 20 to Murgatroyd's expression.
[Figure from [Keck M.Sc. Thesis \(2015\)](#)].

The ohmic region of the curve can be fit to obtain resistivity via the standard expression, where ρ is resistivity, V is the applied voltage, I is the measured current, A is the contact area, and d is the sample thickness:

$$\rho = \frac{VA}{Id} \quad [5]$$

Fitting the SCLC region of the curve to the Murgatroyd expression (via the Blakesley protocol³⁷) in the form:

$$I_{SCLC} = A_1 V^2 \exp(t_1 \sqrt{V}) \quad [6]$$

$$A_1 = \frac{9A\mu_0\epsilon}{8d^3} \quad [7]$$

$$t_1 = \frac{0.891\gamma}{\sqrt{d}} \quad [8]$$

yielded parameters A_1 and t_1 , from which μ_0 and γ could be calculated. Inserting these terms into Equation 3 yields the field-dependent mobilities.

Resistivity (ρ), mobility (μ), and free carrier concentration (n) (obtained via $\rho = 1/en\mu$) were measured for a large number of samples. Because ρ , μ , and n are related via $\rho = 1/en\mu$, we expect a correlation between variables. Indeed, there is a strong linear correlation between $\log(\mu_F)$ and $\log(\rho)$ [Figure 22(a)] as well as a definite correlation between $\log(\mu_F)$ and $\log(n)$ [Figure 22(b)] and $\log(n)$ and $\log(\rho)$ [Figure 22(c)]. In the latter two cases, however, the $\log(\mu_F)$ – $\log(n)$ and $\log(n)$ – $\log(\rho)$ scatter plot appears to define a plane rather than a line. Indeed, when all three variables are plotted against one another in 3D space, this plane is clearly defined [Figure 22(d)] by four extremes: low μ (10^{-14}), high n (10^{17}) and high ρ (10^{16}); high μ (10^{-5}), low n (10^{15}), and low ρ (10^8); low μ (10^{-13}), very high n (10^{19}), and moderate ρ (10^{13}); and moderate μ (10^{-9}), low n (10^{14}), and moderate ρ (10^{13}). Overall, this large data set demonstrates the extreme tunability of a- $B_xC:H_y$, with mobility for example ranging across ten orders of magnitude, and allows us to understand the combinations of charge transport properties possible.

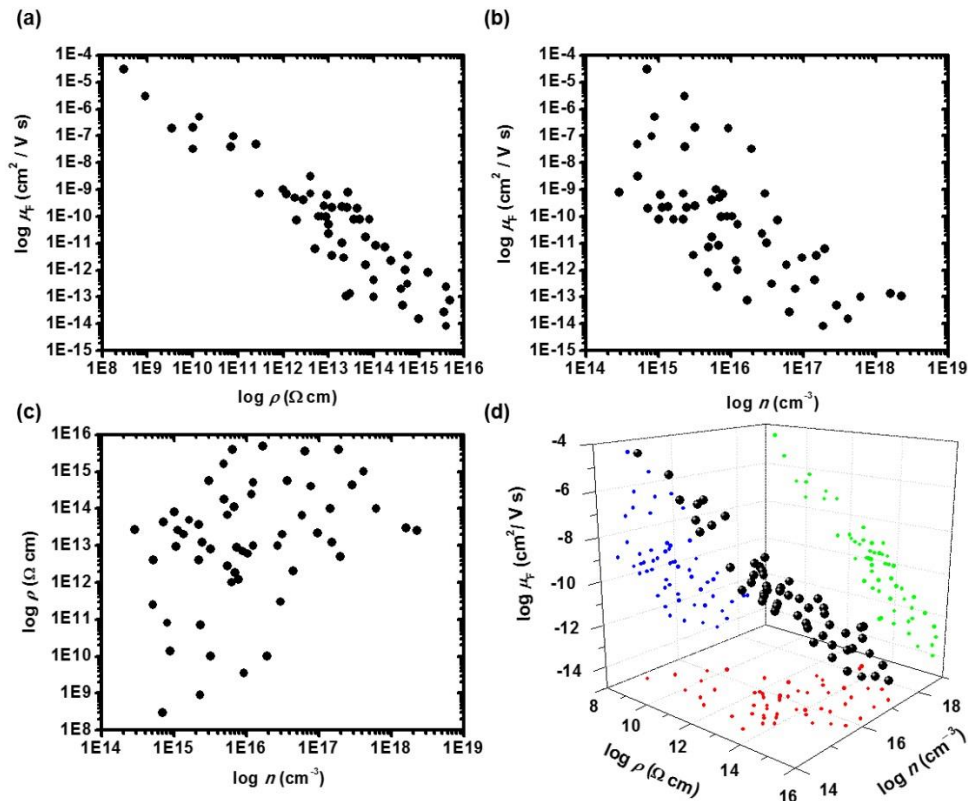


Figure 22. Correlations between (a) mobility (μ_F , at 0.1 MV/cm) and electrical resistivity (ρ), (b) μ_F and charge carrier concentration (n), (c) ρ and n , and (d) all three variables (all plotted as logarithmic values).

4.3.1.2. Dark-Injection Transient Space-Charge-Limited Current

In the DI-SCLC method, a voltage pulse is applied to a sandwich-geometry unipolar heterostructure (i.e., the material is either majority electron/hole or has injecting contacts for one type of carrier and blocking contacts for the other), and the time-dependent current response recorded (Figure 23). The voltage pulse generates electron–hole pairs at the surface of the device, effectively creating a ‘sheet’ of charge carriers that induces a transient current response in the external circuit as it is swept across the device under an applied electric field. The current transient will display a maximum at time $t = \tau$, which is related to the transit time of the sheet of charge, t_{tr} , by:⁴⁸

$$\tau = 0.787t_{\text{tr}} \quad [9]$$

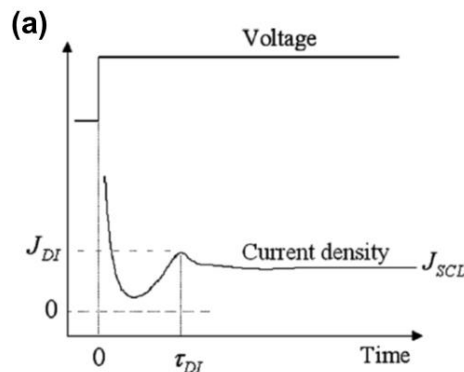


Figure 23. Idealized transient current response from a DI-SCLC experiment. [Figure adapted from ref⁴⁹].

One of the challenges to implementing the DI-SCLC method for a high-resistivity solid such as a-B_xC:H_y is surmounting RC time delay issues. To convert current into a measurable voltage, measuring across a resistor with a sufficiently large resistance is necessary. The result is a voltage decay that masks the desired signal [Figure 24(a) and (b)]. While Scott et al.⁵⁰ originally proposed to rectify this with a bridge circuit [Figure 24(c)], we have opted to implement a transimpedance amplifier circuit [Figure 24(d)], more recently described by Szymanski et al.⁵¹ Here, current is directed into the negative input of an op amp. A resistor is connected across the op amp’s negative

input and output while the positive input is grounded. An oscilloscope measures the voltage from the op-amp's output. By placing the resistor across the op-amp, its resistance is removed from the circuit. This reduces the series resistance of the circuit and results in a smaller RC time constant that will not override the current transient peak.

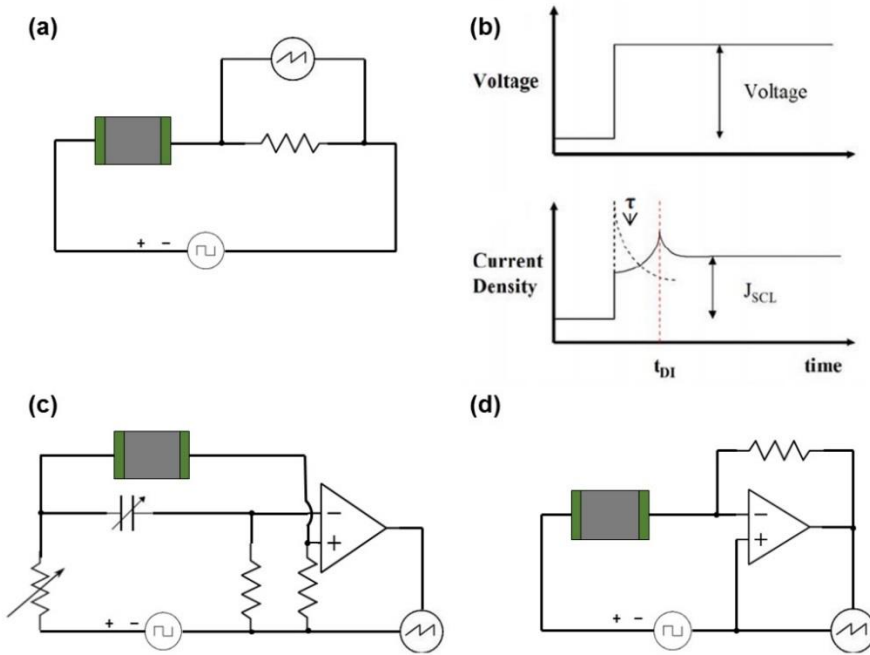


Figure 24. (a) simple resistor circuit; (b) effect of RC voltage delay (dotted line) swamping out desired signal (solid line) [figure from ref⁵²]; (c) bridge circuit; (d) transimpedance amplifier circuit.

Transient current measurements were completed on a subset of samples. Not all samples yielded usable results, typically because of either electrical breakdown or insufficient output current. Representative data is shown in Figure 25. From the current transients, peak time, τ , was extracted by taking the derivative of a polynomial fit, and the mobility calculated based on transit time obtained from Equation 9. Since the mobility in $a\text{-B}_x\text{C:H}_y$ exhibits a field dependence, the zero-field mobility (μ_0) and gamma factor (γ) were extracted by fitting a plot of μ_F vs $E^{1/2}$ (Figure 26). Results for both steady-state and transient measurements are compiled in Table 2, and illustrated for select samples in Figure 27.

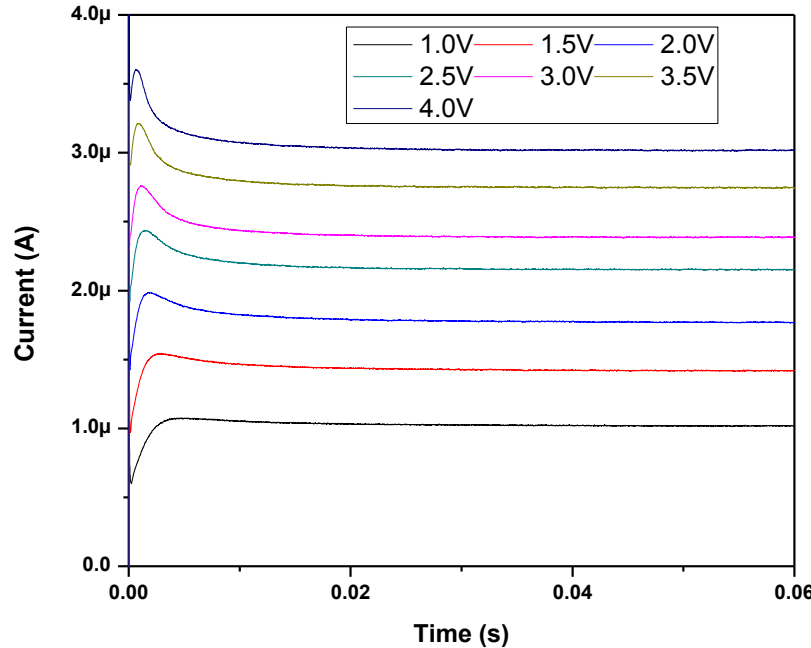


Figure 25. DI-SCLC current transients for a Hg/a-B_xC_y/Si heterostructure (N16) at varying fields. [Figure from [Keck M.Sc. Thesis \(2015\)](#)].

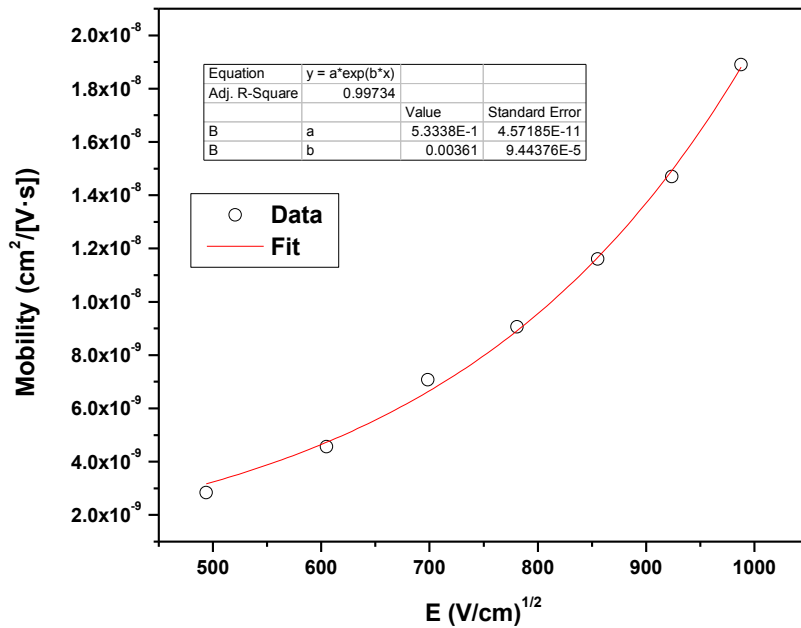


Figure 26. Mobility vs $E^{1/2}$ for the data from Figure 24. [Figure from [Keck M.Sc. Thesis \(2015\)](#)].

Table 2. Comparison of mobility metrics obtained from transient (dark-injection) and steady-state mobility measurements.

	DI-SCLC					SS-SCLC				
	γ (cm/V) ^{1/2}	μ_0 (cm ² /V·s)	μ_F (0.5 MV/cm) (cm ² /V·s)	μ_F range (cm ² /[V·s])	E range (kV/cm)	γ (cm/V) ^{1/2}	μ_0 (cm ² /V·s)	μ_F (0.5 MV/cm) (cm ² /V·s)	μ_F range (cm ² /V·s)	E range (kV/cm)
A	-1.1×10^{-2}	2.4×10^{-5}	3.2×10^{-8}	5.0×10^{-6} – 2.2×10^{-6}	23–56	-3.2×10^{-3}	2.7×10^{-7}	2.8×10^{-8} ^a	1.7×10^{-7} – 1.3×10^{-7}	23–78
N16	3.6×10^{-3}	5.3×10^{-10}	3.2×10^{-9}	2.8×10^{-9} – 1.9×10^{-8}	244–976	5.6×10^{-4}	7.5×10^{-11}	1.1×10^{-10} ^a	1.5×10^{-10} – 1.8×10^{-10}	1460–2440
N28b	-8.6×10^{-4}	8.9×10^{-9}	5.8×10^{-9}	6.0×10^{-9} – 4.9×10^{-9}	134–470	-1.1×10^{-3}	8.3×10^{-7}	3.8×10^{-7}	6.2×10^{-7} – 4.1×10^{-7}	67–393
2N32	1.9×10^{-2}	2.2×10^{-13}	3.5×10^{-10}	2.6×10^{-10} – 6.8×10^{-10}	134–175	1.1×10^{-3}	1.3×10^{-13}	2.8×10^{-13}	1.9×10^{-13} – 2.0×10^{-13}	103–155
N40	-1.6×10^{-2}	1.8×10^{-6}	2.2×10^{-11}	4.4×10^{-11} – 3.1×10^{-11}	436–473	-2.0×10^{-5}	7.4×10^{-9}	7.3×10^{-9}	7.3×10^{-9} – 7.3×10^{-9}	303–909
Q14	-1.3×10^{-3}	6.0×10^{-10}	3.1×10^{-10}	2.7×10^{-10} – 1.8×10^{-10}	339–847	-1.6×10^{-4}	8.1×10^{-14}	7.2×10^{-14}	7.7×10^{-14} – 7.5×10^{-14}	76–254
Q19	-2.6×10^{-4}	3.7×10^{-10}	3.1×10^{-10}	3.1×10^{-10} – 3.1×10^{-10}	460–540	-5.5×10^{-4}	9.6×10^{-14}	6.5×10^{-14}	7.4×10^{-14} – 6.4×10^{-14}	230–550
Q26	-1.6×10^{-3}	1.5×10^{-9}	6.7×10^{-10}	7.2×10^{-10} – 6.0×10^{-10}	216–333	-2.2×10^{-3}	4.5×10^{-14}	9.5×10^{-14}	2.5×10^{-14} – 1.3×10^{-14}	69–314
Q28	-4.6×10^{-3}	2.5×10^{-9}	4.2×10^{-10}	7.3×10^{-10} – 2.2×10^{-10}	71–286	3.8×10^{-3}	7.8×10^{-12}	1.2×10^{-11}	2.2×10^{-11} – 2.9×10^{-11}	79–125

^aElectric field range did not actually extend to 0.5 MV/cm

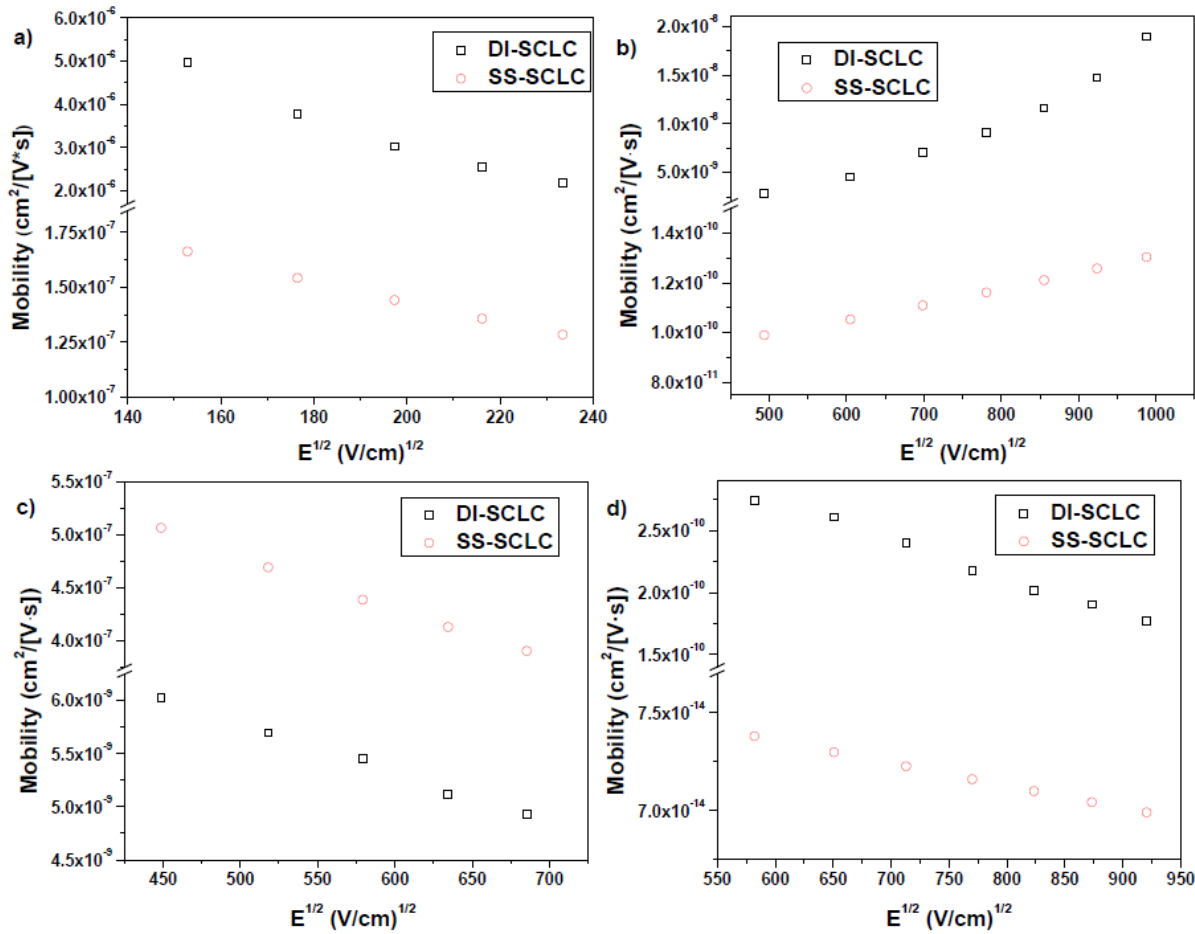


Figure 27. Comparison of DI-SCLC and SS-SCLC field-dependent mobility for select samples:
 (a) A (Cu/a-B_xC:H_y/Cu), (b) N16 (Hg/a-B_xC:H_y/Si), (c) N28b (Hg/a-B_xC:H_y/Si), and (d) Q14
 (Hg/a-B_xC:H_y/Si). [Figure from [Keck M.Sc. Thesis \(2015\)](#)].

The mobility values obtained from transient measurements were found to be higher than those obtained from steady-state measurements, by between one and four orders of magnitude, but the trends were generally the same. Weiß et al.⁴⁰ obtained a similar result, and ascribed it to the fact that, while transient experiments measure transit time directly, slow trapping can have a significant effect on steady-state measurements. Obtaining negative values for γ is also an unusual result, but may be associated with disorder in amorphous solids.⁵³

Overall we conclude that steady-state space-charge-limited current measurements appear to be an efficient technique for high-throughput mobility measurements on a-B_xC:H_y thin films, as transient measurements were found to be fairly demanding to implement consistently for all types

of films (e.g., different thicknesses, mobilities, contact types). The trends in mobility values were supported by both steady-state and transient techniques, with the transient techniques yielding systematically higher values. A more rigorous analysis of the transient data may lead to additional details regarding charge trapping/detrapping and relevant timescales.

4.3.2. Mobility–Lifetime Product Measurements

Steady-state photoconductivity (SS-PC) experiments are commonly applied to determine the mobility–lifetime, $\mu\tau$, product of a material. Steady-state photocurrent density, J_{ph} , is dependent on photon energy/wavelength (λ) and applied field (E)/voltage (V), as:⁵⁴

$$J_{ph}(\lambda, V) = e\Phi \int_0^d \eta_g(\lambda, x)\eta_c(x, V)dx \quad [10]$$

where e is elementary charge, Φ photon flux, η_g charge carrier generation efficiency, and η_c charge collection efficiency. At low electric fields, photoconductivity, σ_{ph} ($\Delta\sigma = \sigma_{illuminated} - \sigma_{dark}$), can be related directly to $\mu\tau$ via:

$$\sigma_{ph} = \Delta\sigma = \sigma_{ill} - \sigma_{dark} = e\Delta n\mu = eG\mu\tau \quad [11]$$

Here, the change in free charge carrier concentration, Δn that occurs upon steady-state illumination is dependent on the balance between the charge carrier generation rate, G , and the relaxation (trapping/recombination) rate, defined by the lifetime, τ (note that in the above equation, n , μ , and τ represent values for either holes or electrons). Generation rate can be determined relatively straightforwardly from knowledge of the photon flux, Φ , and optical response of the device via:

$$G = \eta_g\Phi(1 - R)\frac{(1 - \exp^{-\alpha d})}{d} \quad [12]$$

Where d represents film thickness, and α and R the absorption coefficient and reflectivity of the film, respectively. In this analysis, η_g can either be determined independently, assumed to be 1, or incorporated into the mobility–lifetime term as $\eta_g\mu\tau$.

Another treatment involves fitting the voltage (V)/field (E)-dependent photocurrent (I_{ph})/photocurrent density (J_{ph}), where ultimately the charge carrier generation rate/efficiency term becomes absorbed into a saturation photocurrent term, J_{ph0} , which can be treated as a fitting parameter. If sufficiently high fields are probed, and under the assumption of uniform light absorption throughout the thickness of the film, J_{ph} can be fit⁵⁵ as a function of V :

$$J_{ph}(V) = J_{ph0} \frac{\mu\tau V}{d^2} \left[1 - \frac{\mu\tau V}{d^2} \left(1 - \exp^{\frac{-d^2}{\mu\tau V}} \right) \right] \quad [13]$$

Note that if absorption is assumed to be primarily at the surface of the device, the Many equation^{55,56} is used:

$$J(V) = \frac{J_0 \frac{\mu\tau_b V}{d^2} \left[1 - \exp^{\frac{-d^2}{\mu\tau_b V}} \right]}{1 + \frac{d s}{V \mu}} \quad [14]$$

which takes into account a surface recombination velocity term, s/μ (here τ_b represents the lifetime within the bulk). Additional corrections can be applied if non-uniform electric fields are expected.⁵⁷

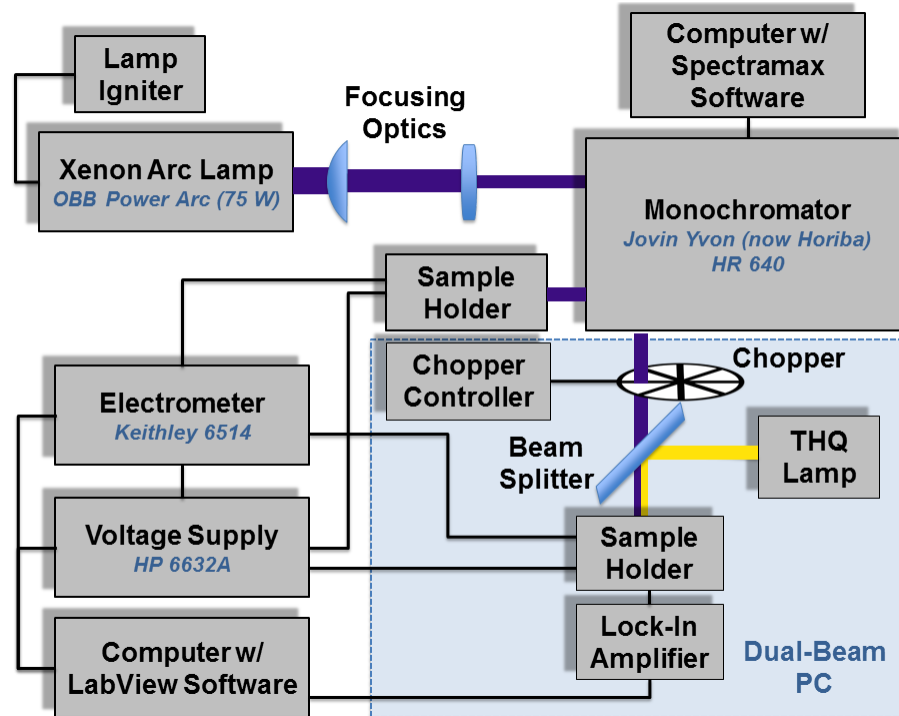


Figure 28. Schematic of steady-state photoconductivity and dual-beam photoconductivity experimental setups.

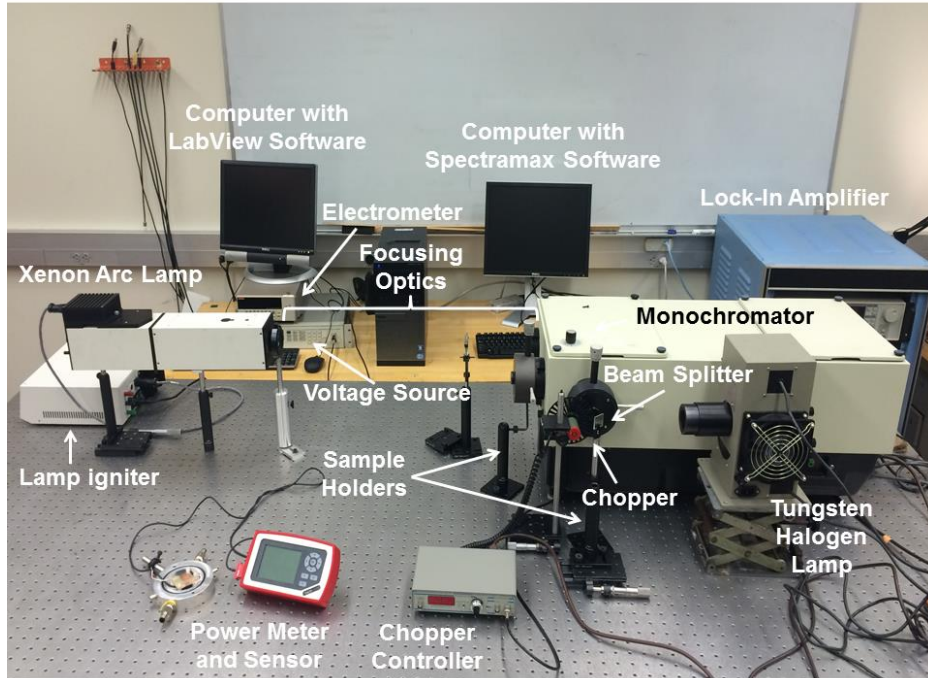


Figure 29. Photoconductivity experimental setup.

An experimental SS-PC apparatus was installed (Figure 28 and Figure 29) based on an OBB PowerArc 75 W Xe arc lamp light source coupled to a Jobin Yvon (now Horiba) HR 640 monochromator to produce a monochromatic beam. A focused beam is guided to a sample holder containing the device under test, which is connected to an HP 6632A voltage source and Keithley 6514 electrometer. The experimental setup was also adapted for dual-beam photoconductivity (DB-PC) experiments. Here, the PowerArc Xe lamp is used as a monochromatic chopped light source, and a second tungsten–halogen–quartz (THQ) lamp is used as a DC bias light source.

Custom Faraday cages were machined and assembled for the experiment [Figure 30(a)]. These have an airtight seal and are fitted with valves to allow the inner space to be filled (and pressurized) with dry nitrogen gas such that the devices may be kept under an inert atmosphere. They further shield the samples from outside light and electromagnetic interference. A 9 mm diameter hole in the bottom of the cage allows light to be directed onto the device. The opening is sealed with a 1 mm thick sapphire window, which allows UV–NIR wavelengths to pass with minimal reflectance/absorbance, while maintaining an airtight space. BNC adapters allow for connection to external electrical circuitry.

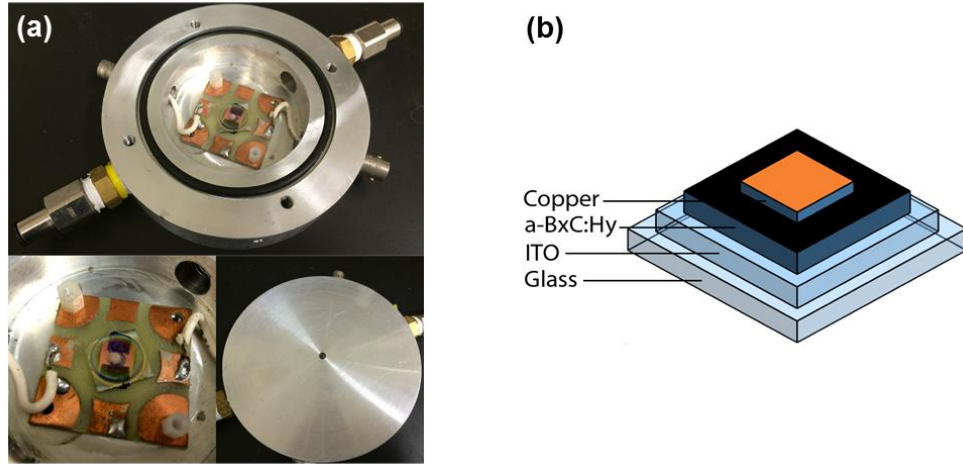


Figure 30. (a) Faraday cage containing device under test; and (b) heterostructure geometry for photoconductivity experiments.

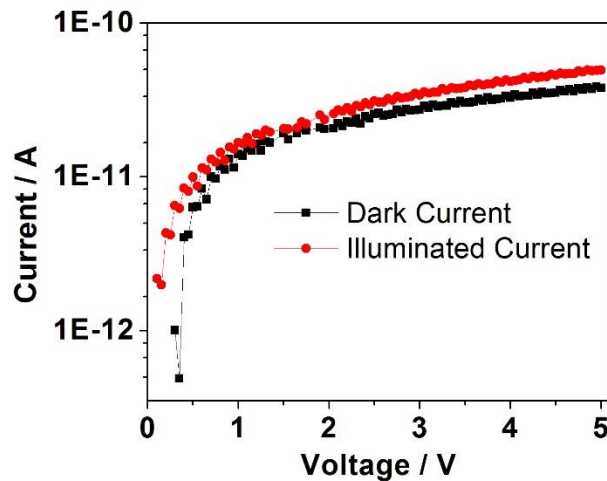


Figure 31. Dark and illuminated current as a function of voltage for a glass/ITO/a-B_xC:H_y/Cu heterostructure under ~0.2 mW/cm² illumination at 450 nm.

Heterostructures for measurement were fabricated by depositing a-B_xC:H_y onto a glass/indium tin oxide (ITO) substrate, and then depositing a top Cu contact by sputtering [Figure 30(b)]. Films used in the results shown here were grown at a temperature of 300 °C 10 W, 0.4 Torr, 200 sccm total flow, and a partial Ar + orthocarbon pressure of 1 for 30 min, resulting in films with a thickness of 750 nm. The devices were then mounted to Cu-coated FR board with silver paint/gold wire, and soldered to the BNC connections within the Faraday cage. Using the above-described

setup, dark and illuminated current were measured as a function of wavelength from 300 to 800 nm and of voltage from 0 to 5 V. Photocurrent was taken as the difference between the two, from which was extracted photoconductivity via:

$$\sigma_{ph} = \frac{dI}{VA} \quad [15]$$

Generation rate was calculated via Equation 12. Photon flux was calculated from a measurement of power output at the sample position (after the Faraday cage to take into account losses due to the sapphire window), which was normalized to irradiation spot size. Quantum efficiency was assumed to be 1. Absorption coefficient, α , was determined from UV–Vis absorbance data [Figure 32(a)], and reflectivity, R , assumed to be 0. Note that both the quantum efficiency and reflectivity assumptions are oversimplifications of the analysis. Mobility–lifetime product calculated based on this generation rate using Equation 11 varies as a function of wavelength, peaking at ~ 2.8 eV (450 nm), at which point it was calculated to be 2×10^{-14} cm²/V. A qualitative snapshot of photoconductivity as a function of illumination energy is provided by the σ_{ph}/Φ curve [Figure 32(b)], wherein it can be seen that it roughly mirrors the absorption curve, though the photoconductivity onset is at about 1 eV lower energy. SS-PC measurements on a number of samples grown under similar conditions yielded consistent $\mu\tau$ values on the order of 10^{-13} – 10^{-14} cm²/V. Mobility measurements on similar films yielded μ of the same order of magnitude, suggesting lifetimes on the order of 1 s.

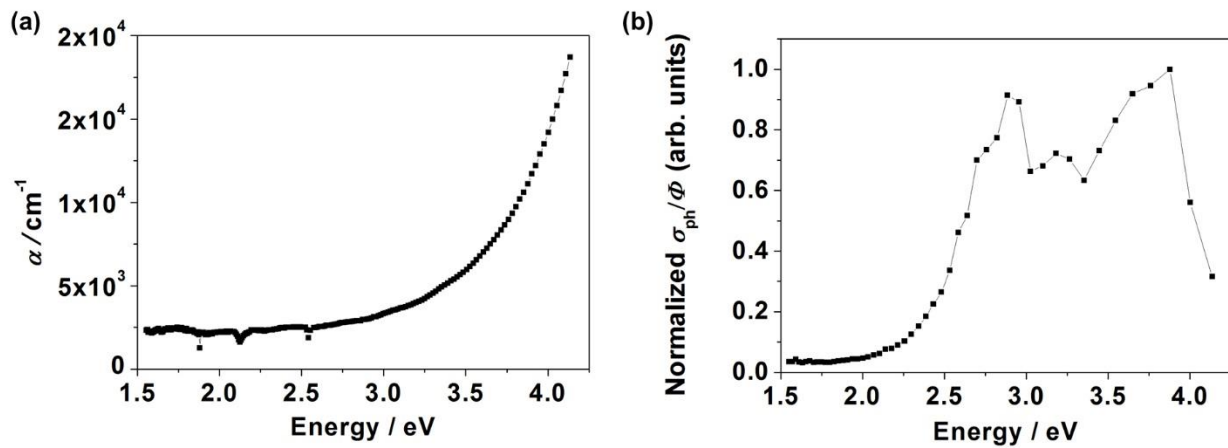


Figure 32. (a) Absorption coefficient for a-B_xC:H_y on glass/ITO. (b) Photoconductivity (normalized to photon flux) as a function of energy.

4.4. Electronic Structure and Charge Transport Models

4.4.1. Electronic Structure Model

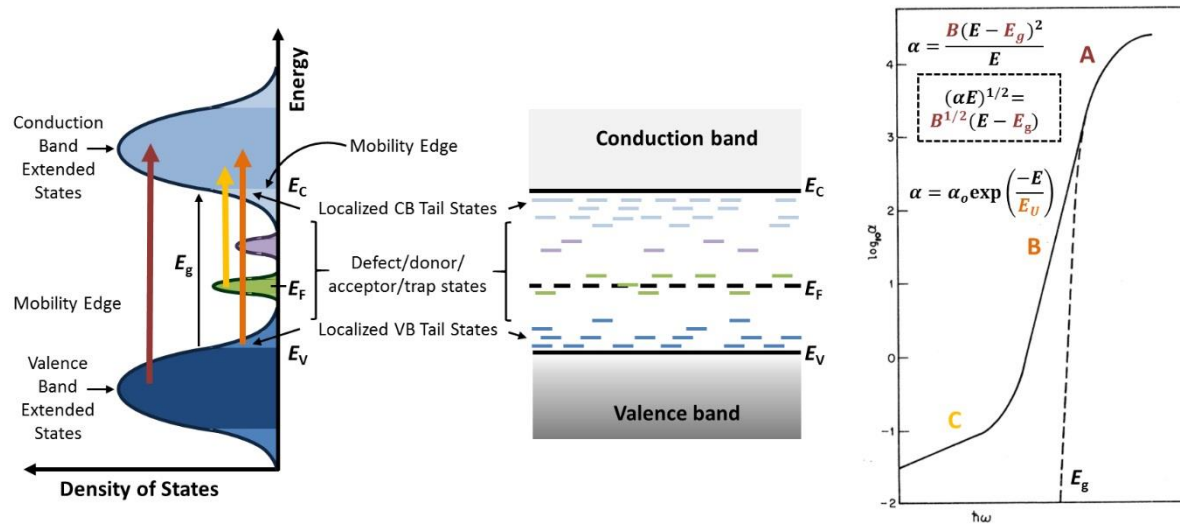


Figure 33. Schematic for the density of states, band diagram, and absorption spectrum for an amorphous solid.

Toward understanding the charge transport properties of a material, it is instructive to analyze its electronic structure (Figure 33). Amorphous semiconductors are unique from crystalline semiconductors in that they exhibit band tails arising from disorder-induced localized states. These exponential band tails, known as Urbach tails, are separated from the conduction and valence bands by the mobility edges, which define the mobility gap—analogous to the band gap in crystalline solids. While the localized states that comprise the Urbach tails can be thought of as a set of shallow traps, amorphous solids may also contain deep traps or mid-gap states. A powerful technique for investigating electronic structure is optical absorption spectroscopy, where the absorbance spectrum represents a superposition of optical transitions between combinations of extended, localized, and mid-gap states.^{58,59} In a plot of absorption coefficient vs energy, three main regions can be identified: region A, at higher energies and with higher absorption intensities, is associated with transitions between extended states; region B, at moderate energies and absorption intensities, is associated with transitions to or from localized tail states, and has been shown to be primarily defined by transitions between localized valence band states and extended conduction band states;⁶⁰ and region C, at the lowest energy and absorption intensities, is

associated with transitions involving mid-gap defect states. Tauc showed that region A can be modeled by a power law according to:

$$\alpha = \frac{B(E - E_g)^n}{E} \quad [16]$$

which can be rearranged to (with n defined as 2, as is typical for most amorphous solids):

$$(\alpha E)^{\frac{1}{2}} = B^{\frac{1}{2}}(E - E_{Tauc}) \quad [17]$$

such that the Tauc optical band gap, E_{Tauc} , and the Tauc parameter, $B^{1/2}$, can be extracted from a plot of $(\alpha E)^{1/2}$ vs E as the intercept and slope of the linear region, respectively. Other methods have been employed to determine the optical band gap of amorphous solids,⁶¹ including the isoabsorption method,^{60–62} where a gap is empirically defined at a given absorption coefficient value (typically E_{04} at $1 \times 10^4 \text{ cm}^{-1}$), as well as the use of alternative values for “ n ” in the Tauc expression (typically 3, as may be appropriate for boron-rich solids).^{63,64} Region B can be fit to the expression:

$$\alpha = \alpha_0 \exp\left(\frac{-E}{E_U}\right) \quad [18]$$

where the Urbach energy, E_U , can be obtained as the slope of the curve for a plot of $\ln(\alpha)$ vs $\ln(E)$.

An analysis of the absorbance spectra for a large number of a-B_xC:H_y films was completed. Details of the analysis are described in [Nordell et al. JAP 118 \(2015\) 035703](#), and a subset of the results can be found in this publication as well as a subsequent one [Nordell et al. \(2015\) submitted, MATCHEMPHYS-D-15-01944](#). Three different methods were applied to extract optical band gap: a Tauc treatment with $n = 2$ and $n = 3$ as well as an isoabsorption treatment with E_{04} defined as the energy at which $\alpha = 1 \times 10^4 \text{ cm}^{-1}$. It was found that E_{Tauc} ($n = 2$) and E_{04} values were relatively close, and could both serve as appropriate measures of optical band gap [see Figure 34(a) for a comparison of the three]. The three electronic structure parameters, E_g , $B^{1/2}$, and E_U were found to range widely as a function of thin-film preparation and composition, with optical band gap ranging from 1.7–4.1 eV, $B^{1/2}$ from 100–2200 eV^{-1/2} cm^{-1/2}, and E_U from 100–800 meV.

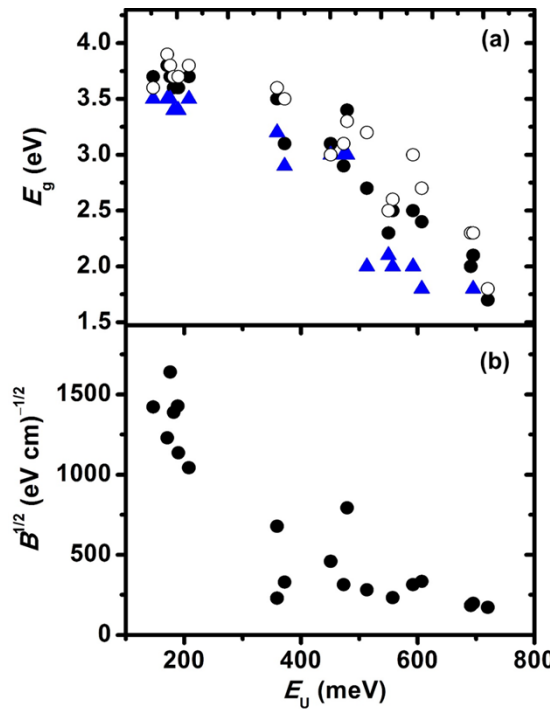


Figure 34. Correlation between (a) band gap values, E_{Tauc} [$n = 2$ (filled circle) and $n = 3$ (blue triangle) and E_{04} (open circle), and Urbach energy and (b) Tauc slope parameter, $B^{1/2}$, and Urbach energy, for a series of a-BC:H films [Figure from [Nordell et al. \(2015\) submitted, MATCHEMPHYS-D-15-01944](#)].

Band gap is correlated to hydrogen concentration (Figure 2 and Figure 3), where a hydrogen-rich low-density film has a high band gap and vice versa. This is the same behavior observed in a-Si:H, one explanation for which pertains to the decrease in network connectivity associated with the incorporation of one-fold-coordinate hydrogen atoms. The Urbach energy and Tauc parameter, both measures of disorder in an amorphous solid, are also correlated with hydrogen concentration: Urbach energy decreases with increasing hydrogen concentration ($B^{1/2}$ shows the opposite trend, but for this parameter high values indicate low disorder), which is the same behavior observed in a-Si:H, and can be explained by a decrease in network strain associated with hydrogen incorporation, and thus decrease in structural disorder.^{59,65} We also found in [Nordell et al. \(2015\) submitted, MATCHEMPHYS-D-15-01944](#) that the carbon content plays a smaller role in defining electronic structure, even though the major trends can be associated with hydrogen content. Finally, we see that band gap and Urbach energy are inversely correlated to one another in a linear fashion [Figure 34(a)], with larger band gaps associated with smaller band tails, and vice versa.

Overall, we have found a remarkable correlation between electronic structure parameters and chemical composition over a wide range of stoichiometries. Although relatively simple, this electronic structure model provides a framework for interpreting gross trends in charge transport in order to zero in on the regime appropriate for fabricating a-B_xC:H_y detectors.

4.4.2. Charge Transport Model

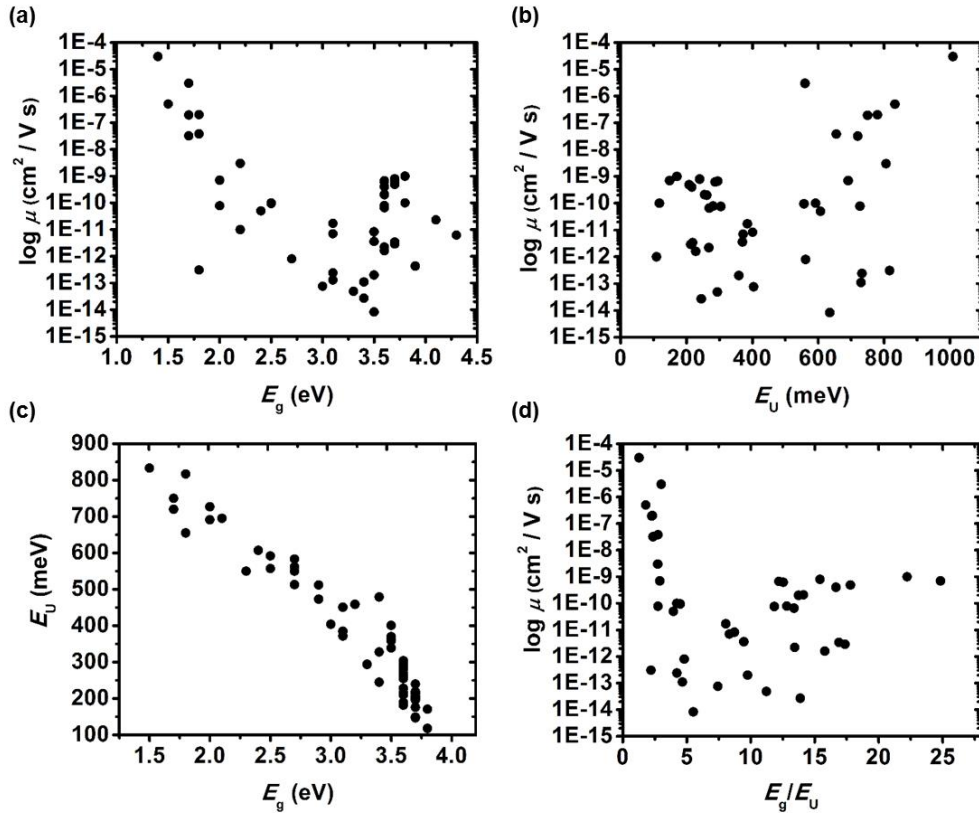


Figure 35. Correlations between (a) mobility and Tauc band gap ($n = 2$), (b) mobility and Urbach energy, (c) Tauc band gap and Urbach energy, and (d) mobility and E_g/E_U .

The charge transport parameters were compared against electronic structure parameters to investigate correlations. These correlations were discussed in some detail for a subset of films in [Nordell et al. \(2015\) submitted, MATCHEMPHYS-D-15-01944](#). What we observed is that the charge transport parameters do not show smooth correlations with electronic structure and chemical composition properties, but rather appear to exhibit different correlated regimes. In Figure 35(a), we observe that mobility exhibits a relatively strong inverse linear correlation with band gap below ~ 3 eV, and what appears to be a weaker direct linear correlation above this value.

The same type of behavior is observed in the mobility vs Urbach energy curve, with a threshold of ~500 meV [Figure 35(b)]. We have already discussed how Urbach energy and band gap are inversely linearly correlated. This is illustrated in Figure 35(c) for a much larger set of samples. Figure 35(d) demonstrates how μ_F can be correlated to both parameters via a joint term E_g/E_U —in the low E_g /high E_U region, the correlation is particularly clear.

Unlike other thin-film properties explored, which tend to exhibit linear correlations with each other and with chemical composition, the unique trends demonstrated by the charge transport properties may suggest the existence of more than one relevant transport mechanism. We initially hypothesized that mobility would trend with Urbach energy, specifically decreasing with increasing E_U and thereby increasing film disorder, as in the case of amorphous hydrogenated silicon. However, we find that maximum mobility values are found at maximum E_U values, and that, at low band gap, mobility decreases with decreasing E_U . Two different charge transport mechanisms can be considered for an amorphous semiconductor. In a multiple trapping (MT) and release mechanism, charge transport occurs via extended band states, and mobility is reduced through trapping by localized states. In this scenario, a higher Urbach energy would imply wider band tails, greater trapping, and thus lower mobility. In variable range hopping (VRH) conduction, charge transport occurs due to transitions between localized states within the gap, and conductivity is thus related to the transition probability for hopping between sites, and can ultimately be related to the concentration of sites.

Figure 36 distinguishes three different electronic structure regimes. Films with high band gaps also have low Urbach energies. This regime is associated with lower-density, hydrogen-rich films, which should have low strain and low disorder—hence the narrow band tails. In this regime, decreases in E_g and increases in E_U are associated with a trend—albeit scattered—toward lower mobilities. This trend would be consistent with a multiple trapping mechanism, where a greater number of localized states leads to increased trapping and therefore decreased mobility. Films with low band gaps have very high Urbach energies. In fact, the band tail width relative to band gap implies that the exponential distribution of localized states fills the entire gap. This regime is associated with high-density, hydrogen-deficient films. From rigidity theory arguments,⁶⁵ these amorphous films would be expected to be significantly overconstrained, and thus highly strained, which would explain the very high disorder parameters. In this electronic structure regime, increases in E_g and decreases in E_U are associated with a trend toward lower mobilities. One explanation for this would be that a variable range hopping transport mechanism dominates, where

the main conduction pathway is via localized rather than band states. This is reasonable due to the high density of localized states within the gap. In this case, mobility would increase with a greater density of localized states, as opposed to in a MT scenario. These transport models are still very crude, but they provide an initial framework for thinking about the structure–property relationships in a-B_xC:H_y films. For example, a goal to “increase mobility by decreasing Urbach energy,” as would be the case in a-Si:H, would not hold in higher density a-B_xC:H_y where mobility—and Urbach energy—are highest. In this region, it may be important to attempt to distinguish types of traps (e.g., shallow vs deep) or types of disorder (e.g., structural vs substitutional) in thinking about further optimizing charge transport properties. Overall, more studies will be needed to confirm hypothesized models (e.g. variable temperature conductivity measurements) and trapping profiles.

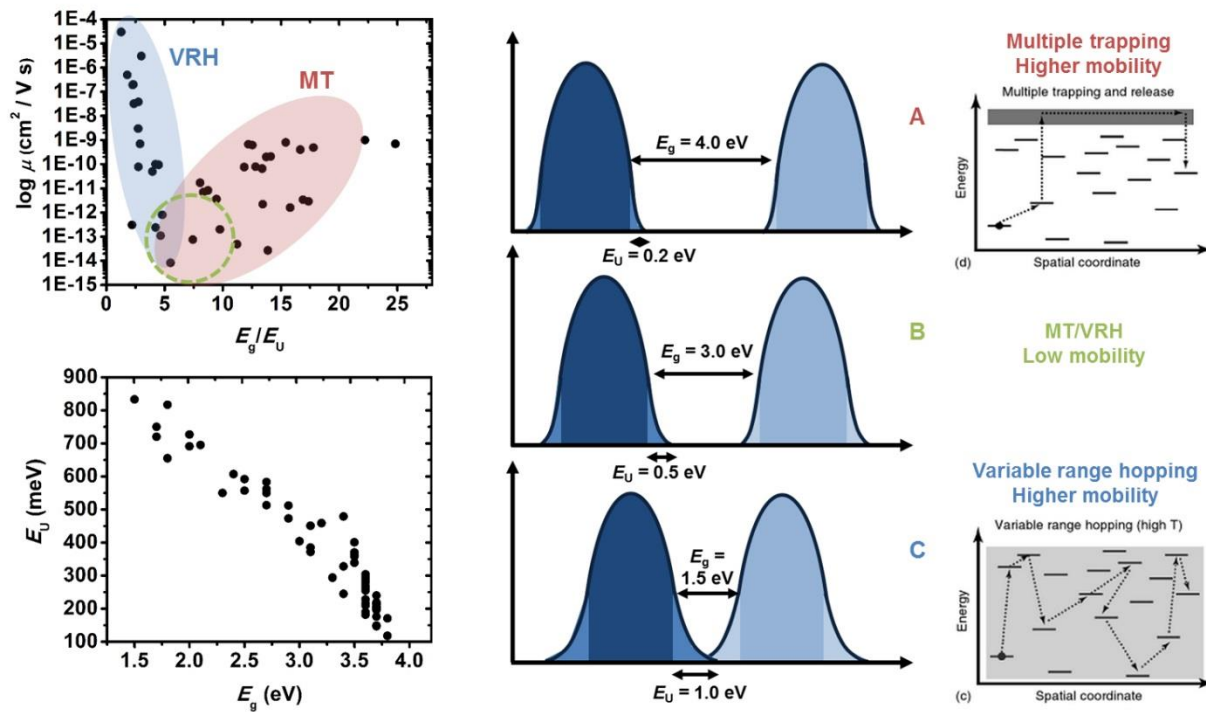


Figure 36. Three different proposed electronic structure models and associated charge transport mechanisms in a-B_xC:H_y: (A) high band gap and low Urbach energy associated with a multiple trapping mechanism, (C) low band gap and high Urbach energy associated with a variable range hopping mechanism, and (B) an intermediate regime.

4.5. Detector Modeling

4.5.1. Theory

Our goal was to model the detection efficiency, specifically for the case of a thin-film detector with relatively low mobility, in order to determine: (a) what detector specifications and a-B_xC:H_y figures of merit are needed to achieve a targeted efficiency, and/or (b) given known detector specifications and a-B_xC:H_y figures of merit, what maximum detection efficiency is theoretically possible. Because detectors are traditionally based on greater thicknesses of bulk material with higher mobilities, the associated theory and assumptions cannot necessarily be applied to the type of device proposed here and must be reviewed.

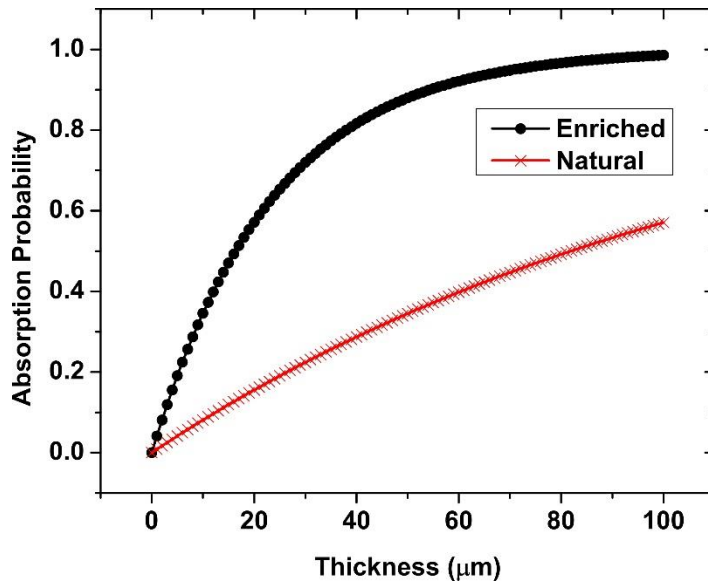


Figure 37. Absorption probability of thermal neutrons as a function of B₄C thickness.

The first step in determining detection efficiency involves understanding the interaction of neutrons with a material. The macroscopic cross section, defined as the interaction probability per unit length of an incident particle in a medium, can be calculated for any composition of matter based on the microscopic cross sections of the atomic constituents. For a boron-based detector, we are interested in the interaction between ¹⁰B and thermal neutrons (i.e., those with an energy of ~0.025 eV, the energy corresponding to room temperature), where ¹⁰B has a very high microscopic thermal neutron cross section of 3840 barn⁶⁶ (1 barn = 10⁻²⁴ cm²). If we assume a material with a stoichiometry of B₄C and density of 2.52 g/cm³,⁶⁷ the macroscopic cross-section for a naturally

abundant sample (~20% of ^{10}B) is 84.38 cm^{-1} and for an enriched sample (100% ^{10}B) is 421.92 cm^{-1} . The corresponding penetration depths (i.e., the reciprocal of the macroscopic cross section) are $118.5 \mu\text{m}$ and $23.7 \mu\text{m}$, respectively. The absorption probability for thermal neutrons as a function of B_4C thickness are given in Figure 37. It is evident that for an enriched sample, nearly maximal neutron absorption can be achieved for thin $100 \mu\text{m}$ films, and only $30 \mu\text{m}$ of material is sufficient for ~75% absorption.

After neutron absorption, the next phenomenon that must be considered is the fate of the neutron capture reaction charged particle products. The absorption of a neutron by a ^{10}B nucleus results in the emission of a positively charged alpha particle and a negatively charged lithium ion. About 94% of this interaction leaves the Li ion in the excited state with the energy distribution $E_{\text{Li}} = 0.84 \text{ MeV}$ and $E_{\alpha} = 1.47 \text{ MeV}$, and the remaining 6% interaction leaves the Li ion in the ground state with the energy distribution $E_{\text{Li}} = 1.02 \text{ MeV}$ and $E_{\alpha} = 1.78 \text{ MeV}$.⁶⁶ Because of the negligible momentum of the incident thermal neutron relative to that of the emitted particles, the emitted particles move opposite to one another with a random emission angle. As long as the emitted particles move within the detector material (B_4C), they excite electron–hole pairs along their paths. If U is the total energy deposited by the emitted particles and E_p is the energy required to create an electron–hole pair, the number of electron–hole pairs (N_{ehp}) generated will be:

$$N_{\text{ehp}} = \frac{U}{E_p} \quad [19]$$

If an electric field E is applied across a detector material in a capacitor geometry, the excited e–h pairs are displaced against the field and induce a current in the external measurement circuit given as:^{68,69}

$$I = \frac{q\mu E}{d} \quad [20]$$

where $q = Ue/E_p$ is the charge deposited (charge of excited electrons/holes), μ is the charge carrier mobility in the detector material, and d is the detector thickness (i.e., electrode spacing). The current can then be integrated for a certain time, t , with the total charge collection represented by:

$$Q_{\text{coll}} = \int_0^t Idt = q \frac{\mu t E}{d} \quad [21]$$

In a real detector, the excited charge carriers are distributed along the detector thickness according to the energy deposited by the emitted Li ion and α particle. The number of excited carriers decreases exponentially with time as a result of carrier trapping and/or recombination, and the carrier concentration at any time t is given as:

$$n(x + vt, t) = n(x, 0) \exp\left(-\frac{t}{\tau}\right) \quad [22]$$

where $n(x, 0)$ is the initial excited carrier concentration at x and τ is the carrier lifetime. Because of the decreasing carrier concentration, the induced current also decays exponentially and the collected charge corresponding to the charge deposited in a small thickness dx at x within the integration time t becomes:

$$dQ_{\text{coll}} = \int_0^t q(x, 0) dx \frac{\mu E}{d} \exp\left(-\frac{t}{\tau}\right) dt \quad [23]$$

where $q(x, 0)dx$ is the charge deposited within a small thickness dx and is obtained from the stopping power, $S(x)$, of the detector material for α particles and Li ions as:

$$q(x, 0) = \frac{S(x)}{E_p} e \quad [24]$$

The total charge collected is then obtained as:

$$Q_{\text{coll}} = \frac{\mu E}{d} \int_{x_{\min}}^{x_{\max}} q(x, 0) dx \int_0^t \exp\left(-\frac{t}{\tau}\right) dt \quad [25]$$

where $x_{\max} - x_{\min}$ is the range within which the charge carriers are excited by the neutron absorption event.

To collect the maximum deposited charge, the minimum integration time must be equal to or greater than the carrier transit time, $t_{\text{tr}} = d/\mu E$. Detectors based on higher mobility materials (e.g., Si) can have low integration times (e.g., on the order of microseconds) because of the short transit time of the carriers even in the case of thick detectors (e.g., on the order of ones of millimeters). For low mobility materials, the transit time becomes long, which sets a higher minimum on the required integration time. However, the integration time cannot always be increased beyond a certain limit. This limit might be set by the time gap between successive detection events—that is, if the charge is integrated over too long of a period, two or more detection events may result in an

overlapped signal pulse (note that this may not be a problem in all detection scenarios, but to obtain a neutron detection efficiency, individual neutrons must be counted). For spectroscopic studies, the match up of integration and transit time is also important. Additionally, from a practical experimental standpoint, the integration time may be limited by the electronics available, which are typically tailored to higher mobility materials and shorter timescale. Thus, because it may be necessary or desirable to use an integration time smaller than the transit time, one must take into account the incomplete charge collection that results from this scenario. If the integration time used is less than the transit time, a boundary is created at:

$$x_0 = d - \mu t E \quad [26]$$

where all the charge carriers generated at $x \geq x_0$ can reach the collecting electrode within the integration time t , whereas those generated at $x < x_0$ can cover a maximum distance of $\mu t E$. Thus the distance that a charge carrier travels becomes smaller than the detector thickness in both of these cases and leads to incomplete charge collection. The total charge collected in a typical case of $x_{\min} < x_0 < x_{\max}$ can therefore be written as the sum of two terms as:

$$Q_{\text{coll}} = \frac{\mu \tau E}{d} \left[1 - \exp \left(-\frac{t}{\tau} \right) \right] \int_{x_{\min}}^{x_0} q(x) dx + \frac{\mu \tau E}{d} \int_{x_0}^{x_{\max}} q(x) dx \left[1 - \exp \left(-\frac{d-x}{\mu t E} \right) \right] \quad [27]$$

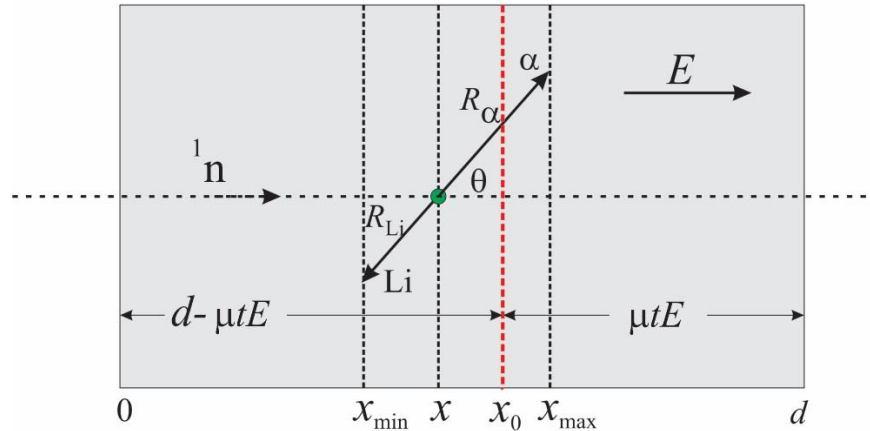


Figure 38. Schematic of neutron detection in a thin-film device.

On the basis of the above theory, a numerical calculation scheme for the detection efficiency of an $a\text{-B}_x\text{C:H}_y$ detector was implemented using Python. In setting up the detection scenario, we assume that neutrons are incident normally on the surface of a planar thin-film detector of thickness d , and a neutron is absorbed by a ^{10}B nucleus at a distance x from the incident surface with a probability density $P(x)$ determined by the macroscopic cross-section (Figure 38). If an alpha particle is emitted at an angle θ with respect to the field direction, a Li ion is emitted at an angle $\pi + \theta$. The charge carriers are thus generated between x_{\min} and x_{\max} determined by the emission angle θ and the ranges R_α and R_{Li} of the α particle and Li ion, respectively. If this range lies inside the detector, the total energy of the reaction products is deposited and leads to the excitation of charge carriers; however, if the reaction products escape the detector, only a fraction of the total energy is deposited.

4.5.2. Calculation and Assumptions

The detection efficiency calculation comprises the following general steps:

1. A random number x is generated with probability density:

$$P(x) = \Sigma \exp(-\Sigma x); \quad x > 0 \quad [28]$$

where Σ is the macroscopic cross-section. The random number x represents the interaction position of an incident neutron with ^{10}B inside the detector. Any values with $x > d$ are discarded and the event is counted as not detected.

2. Another random number $\theta \in [0, \pi]$ is generated, which represents the emission angle of the alpha particle from the interaction position x .
3. The range $x_{\min} - x_{\max}$ over which the energy of the α particle and Li ion is deposited is calculated based on the interaction position x and emission angle θ .
4. The boundary x_0 is calculated based on the defined values of mobility, μ , integration time, t , and applied electric field, E .
5. The charge deposited per unit distance, $q(x)$, is calculated based on the known stopping power of the detector material and the emission angle θ .
6. The charge collected by the external circuit is calculated using the following expressions:

For $x_{\min} > x_0$:

$$Q_{\text{coll}} = \frac{\mu\tau E}{d} \int_{x_{\min}}^{x_{\max}} q(x) dx \left[1 - \exp\left(\frac{x-d}{\mu\tau E}\right) \right] \quad [29]$$

For $x_{\max} < x_0$:

$$Q_{\text{coll}} = Q \frac{\mu\tau E}{d} \left[1 - \exp\left(-\frac{t}{\tau}\right) \right] \quad [30]$$

For $x_{\min} < x_0 < x_{\max}$:

$$Q_{\text{coll}} = \frac{\mu\tau E}{d} \left[1 - \exp\left(-\frac{t}{\tau}\right) \right] \int_{x_{\min}}^{x_0} q(x) dx + \frac{\mu\tau E}{d} \int_{x_0}^{x_{\max}} q(x) dx \left[1 - \exp\left(\frac{x-d}{\mu\tau E}\right) \right] \quad [31]$$

Here, for a hole-only device where the mobile holes are moving along the x -axis (i.e., along the electric field axis), $t_{\text{tr}} = (d-x)/\mu E$ and Q is the total charge deposited.

7. The collected charge is compared against the minimum detection threshold: if it exceeds the threshold, the event is counted as detected.
8. The total detection efficiency is then calculated as:

$$\text{Detection Efficiency} = \frac{\text{Number of detected counts}}{\text{Total number of incident neutrons}} \times 100\% \quad [32]$$

For the calculation of the detection efficiency in an a-B_xC:H_y detector, the following specific assumptions were applied. We note that these assumptions are expected to provide a close approximation to the true behavior of an a-B_xC:H_y device, but can be modified in a plug-and-play fashion to reflect new information regarding the properties of the material/device under test and/or the specific experimental setup and limitations.

1. The detector material was assumed to have a composition of B₄C and density of 2.52 g/cm³. In reality, the material used will have a B/C ratio between 3.5 and 5, 5–20% hydrogen concentration, and a density between 1.8 and 2.4 g/cm³. Future treatments can be modified to include the precise composition of the bulk detector material.

2. The energy deposition for an α particle and a Li ion in the B_4C material was obtained using the SRIM (Stopping and Range of Ions in Material)⁷⁰ simulation package. The stopping powers (i.e., the energy deposited per unit distance) for the particles are shown in Figure 39.

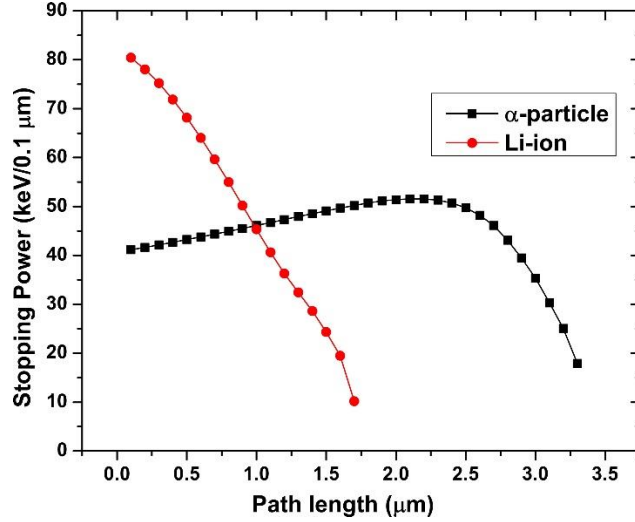


Figure 39. Bragg curves for a 1.47 MeV α particle and a 0.84 MeV Li ion in B_4C .

From the SRIM calculation, the range for an α -particle in B_4C was found to be 3.32 μm and for a Li ion to be 1.69 μm . For simplicity, the stopping power of the α particle was approximated to be uniform over its range by:

$$S_{\alpha}(x) = 440.12 \frac{\text{keV}}{\mu\text{m}} \quad [33]$$

and that of the Li ion was approximated by a linear equation as:

$$S_{\text{Li}}(x) = -433.2x + 884 \frac{\text{keV}}{\mu\text{m}} \quad [34]$$

3. The average energy required to produce one e–h pair is given by:⁷¹

$$E_p = \frac{14}{5} E_g + r; \quad 0.5 \leq r \leq 1.0 \text{ eV} \quad [35]$$

where E_g is the band gap of the material. Based on a representative band gap value of 3–3.5 eV, the energy cost per e–h pair was approximated to be 10 eV.

4. Only one type of charge carrier—specifically, holes—was assumed to be mobile, and the direction of the applied electric field, and thus carrier drift, are in the direction of the incident

neutrons. The choice of holes as mobile carriers is supported by evidence of p-type conductivity in crystalline⁷² and amorphous²² boron carbide, and has been consistent with charge transport measurements within our group. This should represent a lower minimum on collection efficiency for the thin-film case.

5. The minimum charge required for detection is set at 10 fC within an integration time of 1 ms. This leads to an average minimum current of 10 pA through the detector which should be detectable with sensitive electronics.
6. The range of parameters used for the calculations were:
 - Drift velocity (μE): $5 \times 10^{-3} - 50$ cm/sec with 20 data points per decade
 - Lifetime (τ): 10^{-5} –1 sec with 1 data point per decade
 - Thickness (d): 1–20 μm in equal intervals of 1 μm
7. The collected charge for the long lifetime case depends on the integration time, that is:

$$Q_{\text{coll}} = \frac{\mu t E}{d} Q_{\text{deposited}} \quad [36]$$

In order to truncate the calculation, combinations of μE , t , and d , for which $\mu t E/d < 0.1$ were not used as these combinations yield a charge collection value well below the threshold for detection. Similarly for the short lifetime case, the combinations for which $\mu t E/d < 0.1$ were also discarded.

8. The calculation is based on 10,000 neutrons incident on the detector, and the area of the detector is assumed to be very large.
9. The charge collection efficiency was calculated based on the total energy collected relative to the total energy deposited (for all 10,000 neutrons), however the detection efficiency was calculated independently for each individual case.

4.5.3. Results and Discussion

Figure 40 shows the charge collection efficiency as a function of carrier drift velocity (μE) for different detector thicknesses and carrier lifetimes. For short lifetimes, the charge collection efficiency increases slowly and saturates with increasing drift velocity because charge carrier trapping on timescales faster than the integration time leads to incomplete charge collection. For longer lifetimes, the charge collection efficiency saturates at a higher rate because most of the deposited charges are collected before they are trapped. Further, it is evident that the drift velocity

must be increased in proportion with the thickness to obtain equivalent charge collection efficiency, that is, either mobility or electric field needs to increase.

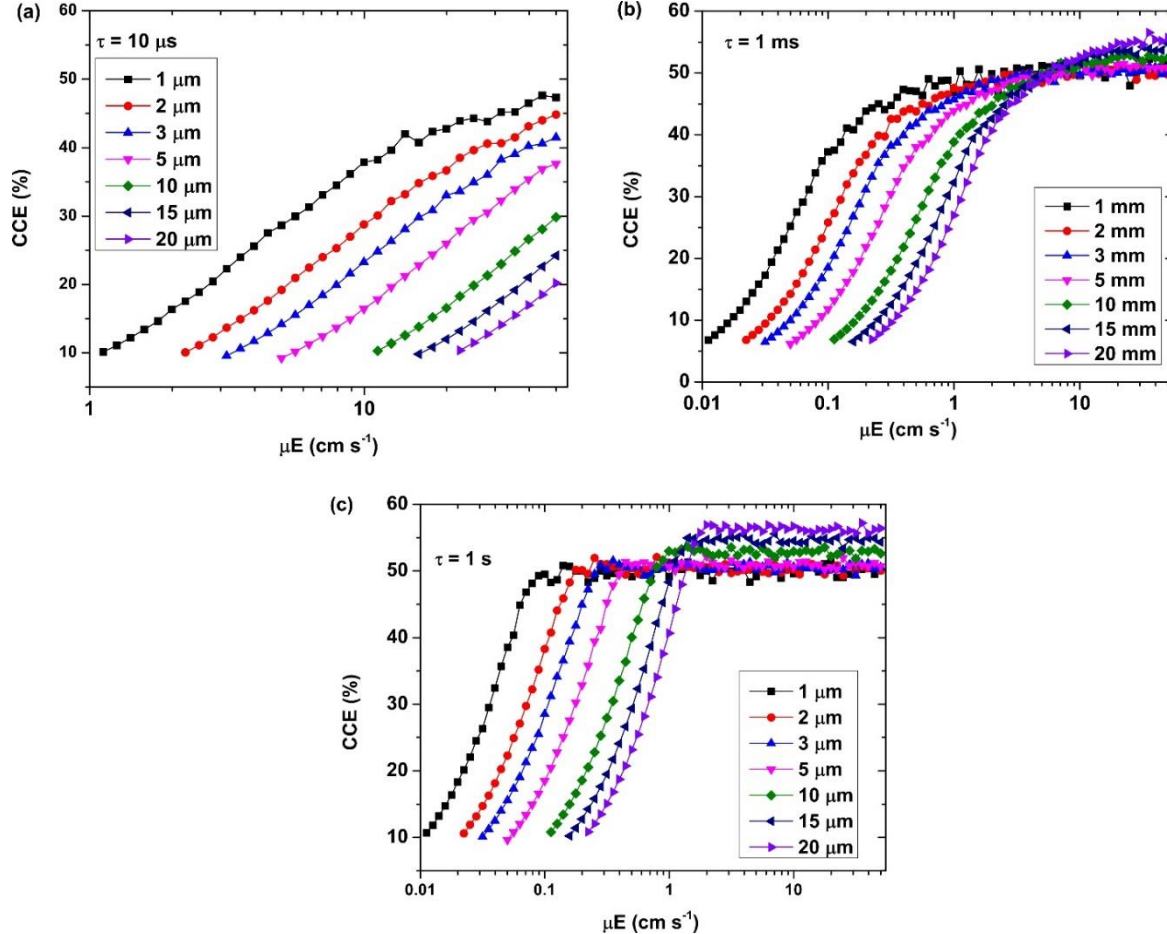


Figure 40. Charge collection efficiency (CCE) as a function of drift velocity ($v = \mu E$) for a range of $a\text{-B}_x\text{C}_y\text{:H}_z$ thicknesses at different lifetimes: (a) $10 \mu\text{s}$, (b) 1 ms , and (c) 1 s .

It is also evident from Figure 40 that the charge collection efficiency saturates at 50% for thin films, and gradually increases above this value with increasing film thickness. For thin films, the charge collection efficiency determined here is very closely approximated by the charge collection efficiency for the uniform absorption treatment in steady-state photocurrent theory:

$$CCE = \frac{\mu\tau E}{d} \left(1 - \frac{\mu\tau E}{d} \left(1 - \exp \left(-\frac{d}{\mu\tau E} \right) \right) \right) \quad [37]$$

where the maximum theoretical efficiency is limited to 50% for high $\mu\tau E/d$ (because we have assumed single-carrier transport). In the uniform absorption case, those carriers generated near the incident surface and drifting the full length of the detector will result in 100% charge collection, whereas those generated at the far surface with negligible distance to travel before reaching the collection electrode will result in 0% charge collection—thus, giving an average of 50% collection. When the thickness of the detector medium becomes very large compared to the penetration depth of the incident particles, the surface approximation treatment may be applied, which predicts a charge collection efficiency of 100% (i.e., all carriers are generated at the incident surface, and drift the full length of the detector to yield 100% charge collection). In the detector simulations presented here, the system moves away from a purely uniform absorption scenario towards a surface absorption scenario, but even for the thickest films modeled (20 μm), the maximum CCE remains much lower than 100%.

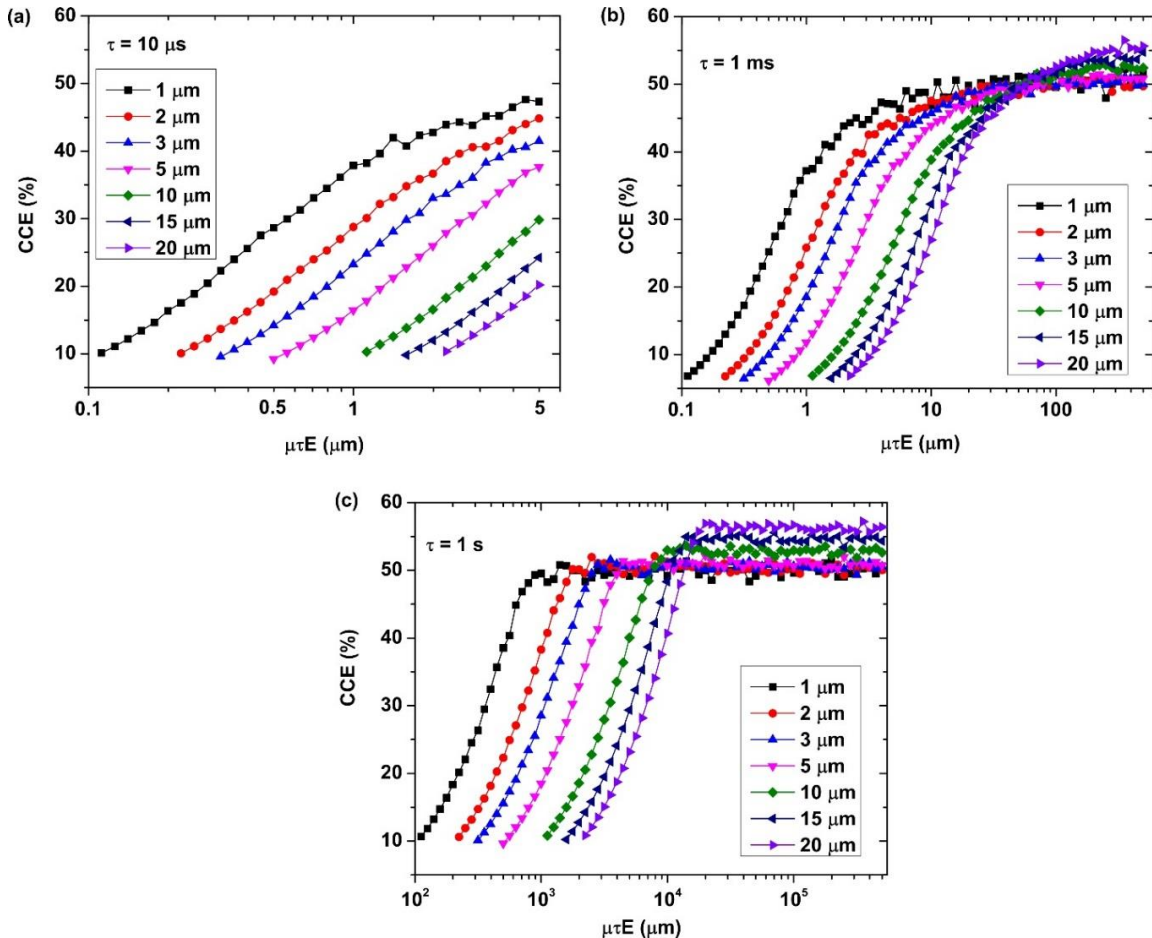


Figure 41. Charge collection efficiency (CCE) as a function of mean carrier drift length ($\lambda = \mu\tau E$) for a range of a-B_xC:H_y thicknesses at different lifetimes: (a) 10 μs , (b) 1 ms, and (c) 1 s.

Figure 41 shows the variation of charge collection efficiency as a function of mean carrier drift length ($\lambda = \mu\tau E$) for different lifetimes. These graphs are very similar to those in Figure 40, but here it is made clear that a higher value of mobility–lifetime product ($\mu\tau$) is not necessarily sufficient for maximum charge collection in all detection scenarios, although it is generally the case for conventional detectors with high mobility materials requiring short integration times. Here, for short lifetimes [Figure 41(a) and (b)], there is little variation in charge collection efficiency with drift length. However in the case of long lifetimes [Figure 41(c)], due to a corresponding low mobility, the actual distance travelled by the carriers within the integration time is in fact less than the drift length, which makes the charge collection efficiency low even for large values of λ . In other words, drift length—the average distance that the carriers can travel if they are allowed sufficient time—does not necessarily represent the true distance that carriers travel within a specified integration time less than their lifetime, so higher drift length (i.e., higher $\mu\tau$ product) does not guarantee high charge collection and one must also consider the values of μ and τ independently.

Because we are interested in detection efficiency, achieving 100% charge collection efficiency is not necessarily the goal, but rather we seek to achieve a CCE sufficient to meet the minimum threshold for registering a detection event. In Figure 42, detection efficiency is plotted as a function of CCE for a range of detector thicknesses at different carrier lifetimes. A common feature in the plots is the onset of a detection threshold at a little over 20% CCE. Once the threshold is crossed, the detection efficiency increases slowly to the saturation value for thin detectors and short carrier lifetimes and rises quickly to the saturation value for thick detectors and long carrier lifetimes.

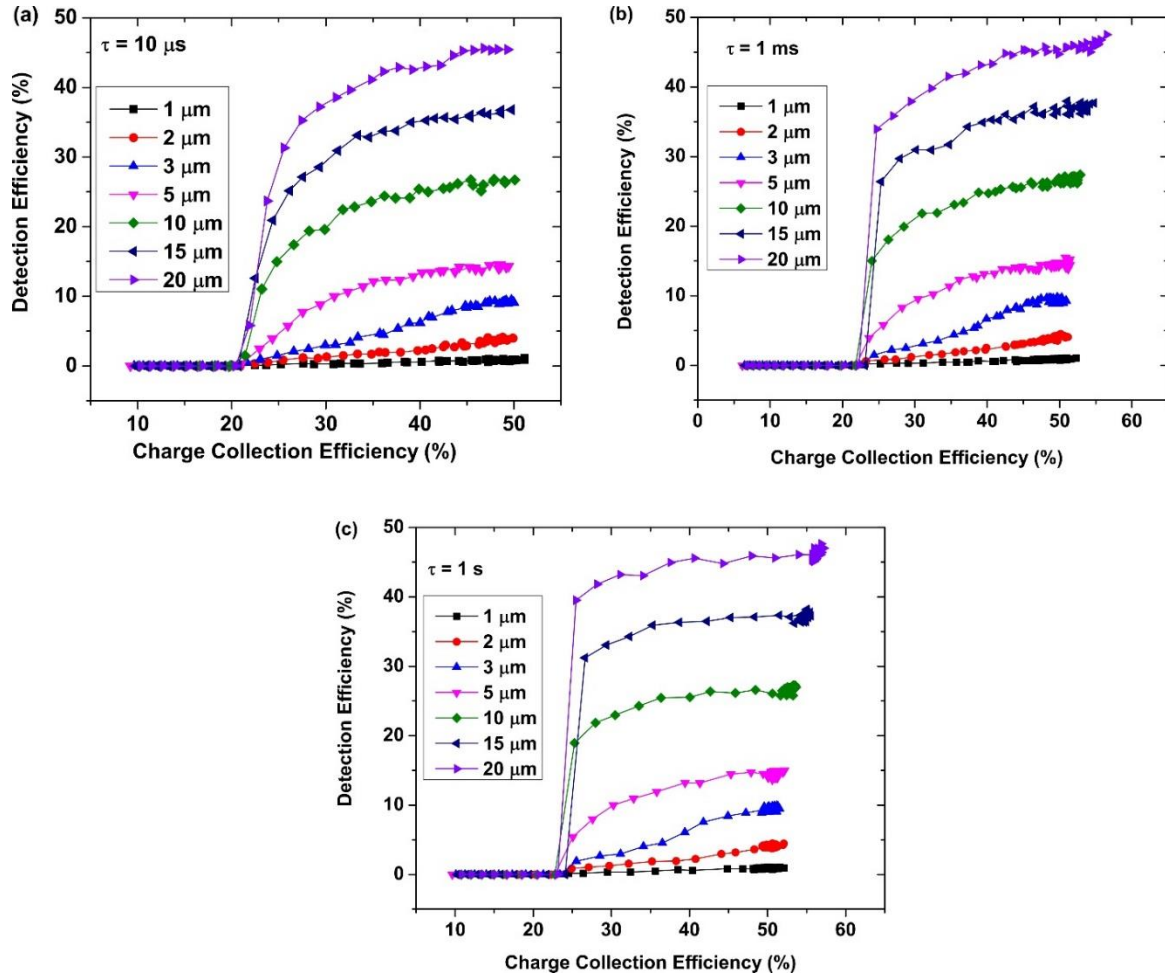


Figure 42. Detection efficiency as a function of charge collection efficiency for a range of detector thicknesses at different lifetimes: (a) 10 μs , (b) 1 ms, and (c) 1 s.

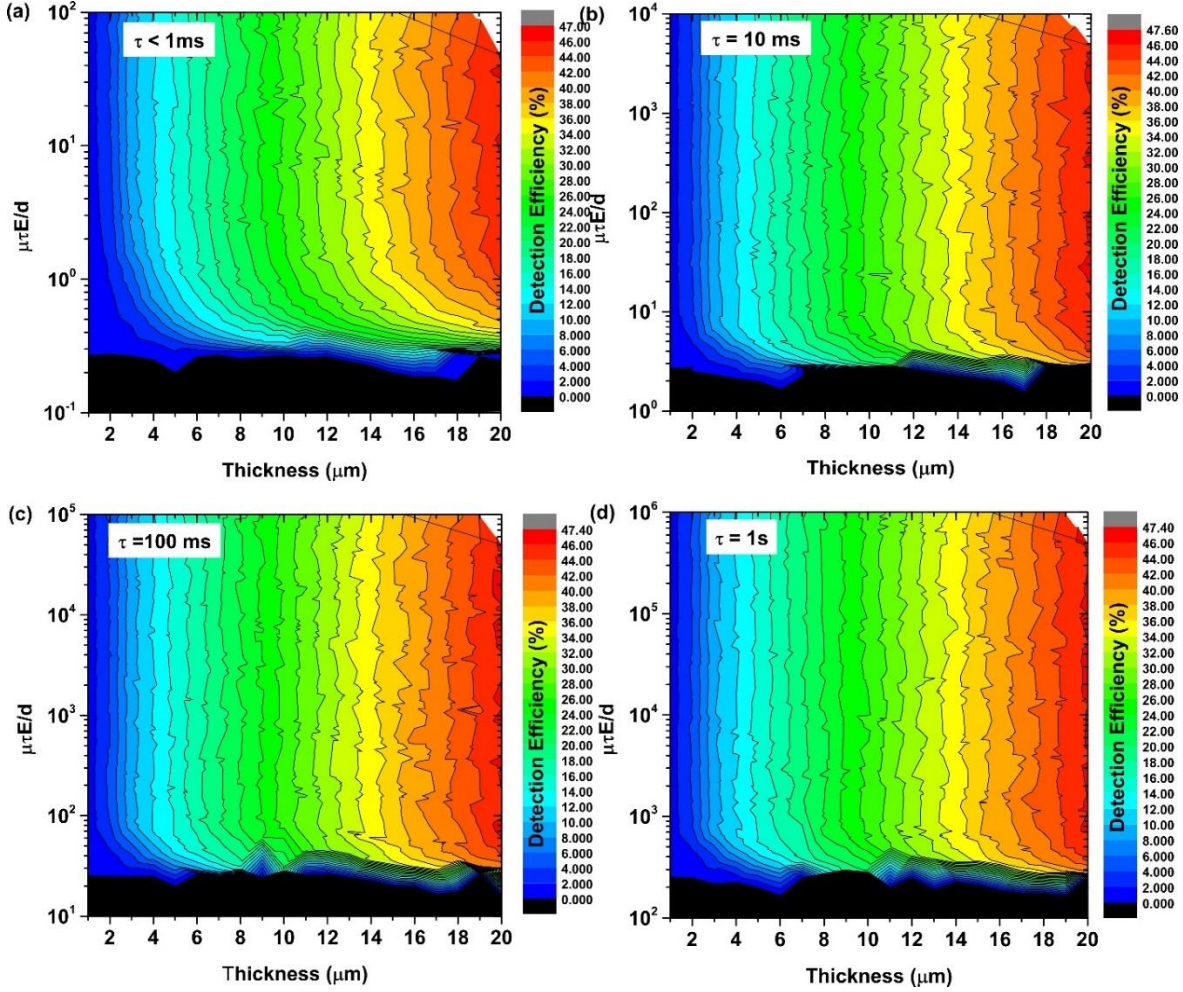


Figure 43. Detection efficiency as a function of $\mu\tau E/d$ and thickness at different lifetimes: (a) $\tau < 1$ ms, (b) $\tau = 10$ ms, (c) $\tau = 100$ ms, and (d) $\tau = 1$ s.

Figure 43 shows the detection efficiency as a function of $\mu\tau E/d$ and thickness for different carrier lifetimes. For small lifetimes ($\tau \leq t$), the detection onset occurs when $\mu\tau E/d \approx 0.35$. For lifetimes greater than the integration time ($\tau \geq t$), the detection onset occurs when $\mu E/d \approx 350$, which yields a current of ~ 13 pA for the maximum possible charge collected. The approximate mobility required to achieve neutron detection is then:

$$\mu > 350 \times \frac{d}{E} \quad [38]$$

If we assume values likely in a detection scenario, $E = 100$ V/ μ m (1 MV/cm), $d = 15$ μ m and $\tau > 10$ ms, the minimum mobility required is therefore 5.0×10^{-7} cm 2 /V·s.

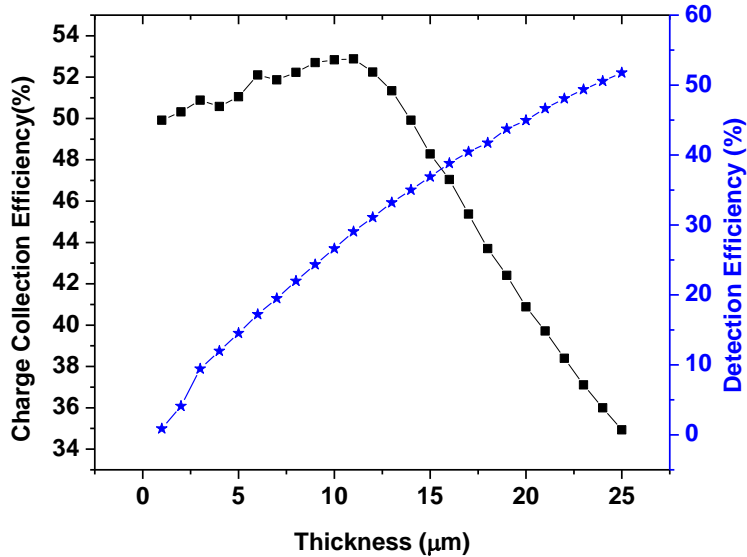


Figure 44. Charge collection efficiency and detection efficiency as a function of detector thickness for $\mu = 10^{-6} \text{ cm}^2/\text{V}\cdot\text{s}$, $E = 1 \text{ MV/cm}$, and $\tau = 1 \text{ s}$.

In Figure 44, charge collection efficiency and detection efficiency are plotted for a planar thin-film detector with $\mu = 10^{-6} \text{ cm/Vs}$, $\tau = 1 \text{ s}$, and $E = 1 \text{ MV/cm}$. The charge collection efficiency increases with thickness up to $10 \mu\text{m}$ (this corresponds to the distance traveled by the charge carriers in the integration time) and then decreases. The initial rise is due to an increase in neutrons being absorbed near the incident surface. As the thickness increases, the $\mu\tau E/d$ ratio decreases, which leads to a drop in charge collection efficiency. The detection efficiency, however, continues to increase with thickness, proportionally to neutron absorption as the charge collection efficiency threshold is still maintained within the range shown in the graph.

5. METRICS

5.1. Personnel

Name	Role	Affiliation	Person Months Worked	Period
Anthony N. Caruso	Professor, PI	UMKC	5	2010–2015
Michelle M. Paquette	Assistant Research Professor	UMKC	15	2011–2015
M. Sky Driver	Graduate student	UMKC	30	2010–2013
Bradley Nordell	Graduate student	UMKC	10	2010–2015
Brent Rogers	Undergraduate student	UMKC	1	2012
Sudarshan Karki	Undergraduate student	UMKC	10	2010–2013
Joseph Otto	Technician	UMKC	6	2013
Mahbube Siddiki	Postdoctoral associate	UMKC	1	2013
Christopher L. Keck	Undergraduate/graduate student	UMKC	25	2012–2015
Emeshaw Ashenafi	Graduate student	UMKC	1	2014
Es-Sakhi Azzedin	Graduate student	UMKC	1	2014
Justin D. Hurley	Undergraduate/graduate student	UMKC	15	2013–2015
Thuong D. Nguyen	High school/undergrad student	UMKC	15	2013–2015
Joe Crow	Postdoctoral associate	UMKC	1	2014–2015
Shailesh Dhungana	Graduate student	UMKC	3	2015
Gyanendra Bhattarai	Graduate student	UMKC	10	2014–2015

5.2. Publications

- (1) J. E. Bevins, J. W. McClory, J. C. Petrosky, and A. N. Caruso, ‘Theoretical Performance of a p-type B₅C:H_x Thin Film on n-Si Neutron Detector,’ in *Am. Nuc. Soc. Trans.* 103 (2010) 212–213.
- (2) Michelle M. Paquette, Wenjing Li, M. Sky Driver, Sudarshan Karki, A. N. Caruso, and N. A. Oyler, “The local physical structure of amorphous hydrogenated boron carbide: insights from magic angle spinning solid-state NMR spectroscopy,” *Journal of Physics: Condensed Matter* 23 (2011) 435002. [<http://dx.doi.org/10.1088/0953-8984/23/43/435002>]
- (3) J. E. Bevins, K. R. Dahl, J. W. McClory, J. C. Petrosky, and A. N. Caruso, “Bulk Radiation Damage Effects of a p-type B₅C:H_x Thin Film on n-Si Heterojunction Diode,” *J. Rad. Effects Res. and Engr.* 30 (2012) 33.
- (4) M. Sky Driver, Michelle M. Paquette, S. Karki, B. J. Nordell, and A. N. Caruso, “The electronic and chemical structure of the a-B₃CO_{0.5}:H_y-to-metal interface from photoemission spectroscopy: implications for Schottky barrier heights,” *Journal of Physics: Condensed Matter* 24 (2012) 445001. [<http://dx.doi.org/10.1088/0953-8984/24/44/445001>]
- (5) B. J. Nordell, S. Karki, T. D. Nguyen, P. Rulis, A. N. Caruso, S. S. Purohit, H. Li, S. W. King, D. Dutta, D. Gidley, W. A. Lanford, and M. M. Paquette, ‘The Influence of Hydrogen on the Chemical, Mechanical, Optical/Electronic, and Electrical Transport Properties of Amorphous

Hydrogenated Boron Carbide,’ *Journal of Applied Physics* 118 (2015) 035703. [<http://dx.doi.org/10.1063/1.4927037>]

(6) B. J. Nordell, C. L. Keck, T. D. Nguyen, A. N. Caruso, S. S. Purohit, W. A. Lanford, D. Dutta, D. Gidley, P. Henry, S. W. King, and M. M. Paquette, ‘Tuning the Properties of a Complex Disordered Material: Full Factorial Investigation of PECVD-Grown Amorphous Hydrogenated Boron Carbide,’ *Submitted to Materials Chemistry and Physics, August 19 2015, MATCHEMPHYS-D-15-01944.*

(7) M. M. Paquette, J. W. Otto, W. A. Lanford, B. J. Nordell, S. Karki, S. W. King, and A. N. Caruso, ‘Thermal Treatment and Depth Profile Studies of Thin-Film Carborane-Based Amorphous Hydrogenated Boron Carbide Growth by Plasma-Enhanced Chemical Vapor Deposition,’ *Journal (2015), To be submitted.*

5.3. Theses/Dissertations

(1) J. E. Bevins, ‘Characterization of a boron carbide heterojunction neutron detector,’ M.Sc. Thesis, Air Force Institute of Technology, Ohio (2011). [<http://www.dtic.mil/cgi/tr/fulltext/u2/a538569.pdf>]

(2) Thomas P. McQuary, ‘Neutron Detection Using Amorphous Boron Carbide Heterojunction Diodes,’ M.Sc. Thesis, Air Force Institute of Technology (2012). [<http://www.dtic.mil/cgi/tr/fulltext/u2/a558329.pdf>]

(3) M. Sky Driver, “The Bulk and Interfacial Electronic and Chemical Structure of Amorphous Hydrogenated Boron Carbide, Ph.D. Dissertation, University of Missouri-Kansas City (2013). [<https://mospace.umsystem.edu/xmlui/handle/10355/41502>]

(4) Christopher L. Keck, ‘Electrical Carrier Mobility Measurements of Amorphous Hydrogenated Boron Carbide Using Space-Charge-Limited Current Techniques,’ M.Sc. Thesis, University of Missouri-Kansas City (2015). [<https://mospace.umsystem.edu/xmlui/handle/10355/46545>]

5.4. Presentations

(1) J. E. Bevins, J. W. McClory, A. Bickley, J. C. Petrosky, and A. N. Caruso, ‘Theoretical Performance of a p-type B₅C:H_x Thin Film on n-Si Neutron Detector,’ *American Nuclear Society Meeting*, Las Vegas, NV, **11/2010**.

(2) A. N. Caruso, ‘Introduction to Solid State Neutron Detection and Spectrometry,’ Invited Talk, *Missouri State University Colloquium*, Springfield, MO, **11/2010**.

(3) J. E. Bevins, J. W. McClory, K. R. Dahl, S. Karki, J. C. Petrosky, A. N. Caruso, ‘Bulk Radiation Damage Effects of a p-type B₅C:H_x Thin Film on n-Si Heterojunction Diode,’ *Hardened Electronics and Radiation Effects Technology Conference*, Orlando, FL, **03/2011**.

(4) M. M. Paquette, ‘Curiosities and Conundrums in the Fabrication, Characterization, and Applications of Thin-Film Boron Carbide,’ *University of Missouri-Kansas City, Department of Physics Colloquium*, Kansas City, MO, **04/2011** (Talk).

(5) M. S. Driver, S. Karki, and A. N. Caruso, ‘Electrical, Physical, and Chemical Properties of the Metal to Amorphous Hydrogenated Boron Carbide Interface,’ *American Vacuum Society 58th International Symposium and Exhibition*, Nashville, TN, **10/2011** (Poster).

(6) M. M. Paquette, W. Li, M. S. Driver, S. Karki, N. A. Oyler, and A. N. Caruso, ‘Investigating the Local Physical Structure of Amorphous Hydrogenated Boron Carbide,’ *American Vacuum Society 58th International Symposium and Exhibition*, Nashville, TN, **10/2011** (Talk).

(7) N. A. Oyler, W. Li, M. M. Paquette, and A. N. Caruso, ‘Local physical structure in hydrogenated boron carbide materials,’ *46th Midwest 39th Great Lakes Joint Regional ACS Meeting*, Saint Louis, MO, **10/2011** (Talk).

(8) W. Li, M. M. Paquette, M. S. Driver, S. Karki, B. J. Nordell, A. N. Caruso, and N. A. Oyler, ‘Molecular structural study of thin-film boron carbide,’ *46th Midwest 39th Great Lakes Joint Regional ACS Meeting*, Saint Louis, MO, **10/2011** (Poster).

(9) R. Cramm Horn, A. Caruso, M. Paquette, P. Rulis, ‘Creating a model of amorphous boron carbide using the LAMMPS molecular dynamics package,’ *XSEDE12*, Chicago, **07/2012** (poster).

(10) M. M. Paquette, J. W. Otto, S. Karki, B. J. Nordell, M. S. Driver, T. D. Nguyen, C. L. Keck, B. J. Rogers, A. Kitahara, S. W. King, W. A. Lanford, S. Purohit, W. Li, C. Zhang, N. A. Oyler, and A. N. Caruso, ‘Establishing Electrical Contacts for Amorphous Hydrogenated Boron Carbide,’ *Materials Research Society Spring Meeting*, San Francisco, CA, **04/01/2013** (Poster)

(11) C. L. Keck, M. M. Paquette, B. J. Nordell, T. D. Nguyen, E. Ashenafi, and A. N. Caruso, ‘Charge Transport in PECVD-Grown Amorphous Hydrogenated Boron Carbide,’ *Materials Research Society Spring Meeting*, San Francisco, CA, **04/01/2013** (Poster).

(12) C. L. Keck, M. M. Paquette, B. J. Nordell, T. D. Nguyen, E. Ashenafi, and A. N. Caruso, ‘Charge Transport in PECVD-Grown Amorphous Hydrogenated Boron Carbide,’ *Nanofrontiers Symposium*, Columbia, MO, **06/06/2013** (Poster).

(13) J. D. Hurley, M. K. Siddiki, C. L. Keck, T. D. Nguyen, B. J. Nordell, M. M. Paquette, and A. N. Caruso, ‘Characterization of PECVD-Grown Thin-Film Amorphous Hydrogenated Boron Carbide using Steady-State Photoconductivity Methods,’ *Nanofrontiers Symposium*, Columbia, MO, **06/06/2013** (Poster).

(14) T. D. Nguyen, S. Karki, C. L. Keck, B. J. Nordell, M. M. Paquette, and A. N. Caruso, ‘The Growth and Characterization of MIM and MIS Amorphous Hydrogenated Boron Carbide Devices,’ *Nanofrontiers Symposium*, Columbia, MO, **06/06/2013** (Poster).

(15) R. Cramm Horn, A. Caruso, M. Paquette, A. Kitahara, and P. Rulis, ‘A Multi-Method Approach to Modeling Amorphous Boron Carbide,’ *International Conference and Exposition on Advanced Ceramics and Composites*, Daytona, FL, **01/29/2013** (Poster).

(16) M. M. Paquette, C. L. Keck, B. J. Nordell, T. D. Nguyen, S. Karki, P. Rulis, N. A. Oyler, S. W. King, and A. N. Caruso, ‘Why Such High Electrical Resistivity in PECVD-Grown Amorphous Hydrogenated Boron Carbide?’ *25th International Conference on Amorphous and Nano-crystalline Semiconductors*, Toronto, Canada, **08/20/2013** (Oral).

- (17) M. M. Paquette, C. L. Keck, B. J. Nordell, T. D. Nguyen, J. D. Hurley, S. Karki, E. Ashenafi, R. Cramm Horn, P. Rulis, S. Purohit, N. A. Oyler, S. W. King, and A. N. Caruso, ‘Exploring Charge Transport in PECVD-Grown Amorphous Hydrogenated Boron Carbide,’ *57th Midwest Solid State Conference*, Lawrence, KS, **09/29/2013** (Oral).
- (18) J. D. Hurley, M. K. Siddiki, C. L. Keck, B. J. Nordell, T. D. Nguyen, A. N. Caruso, and M. M. Paquette, ‘Mobility-lifetime Product Measurement in Amorphous Hydrogenated Boron Carbide Using the Steady-State Photoconductivity Method,’ *57th Midwest Solid State Conference*, Lawrence, KS, **09/29/2013** (Poster).
- (19) C. L. Keck, B. J. Nordell, T. D. Nguyen, J. D. Hurley, A. N. Caruso, and M. M. Paquette, ‘Mobility Measurements of Amorphous Hydrogenated Boron Carbide Utilizing the Dark-Injection Space-Charge-Limited Current Method,’ *57th Midwest Solid State Conference*, Lawrence, KS, **09/29/2013** (Poster).
- (20) B. J. Nordell, S. Karki, T. D. Nguyen, C. Keck, S. W. King, S. Purohit, A. N. Caruso, and M. M. Paquette, ‘Controlling the Dielectric and Electronic Properties of PECVD-Grown Amorphous Hydrogenated Boron Carbide Films,’ *57th Midwest Solid State Conference*, Lawrence, KS, **09/29/2013** (Poster).
- (21) R. Cramm Horn, A. Caruso, M. Paquette, and P. Rulis, ‘A Multi-method Approach to Modeling Amorphous Hydrogenated Boron Carbide,’ *57th Midwest Solid State Conference*, Lawrence, KS, **09/29/2013** (Poster).
- (22) J. D. Hurley, T. D. Nguyen, B. J. Nordell, C. L. Keck, A. N. Caruso, and M. M. Paquette, ‘Mobility-Lifetime Measurements of Amorphous Hydrogenated Boron Carbide Using Steady-State Photoconductivity,’ *American Physical Society March Meeting*, Denver, CO, **03/06/2014** (Oral).
- (23) C. L. Keck, B. J. Nordell, T. D. Nguyen, J. D. Hurley, A. N. Caruso, and M. M. Paquette, ‘Mobility Determination of Amorphous Hydrogenated Boron Carbide from Dark-Injection Space-Charge-Limited Current Method,’ *American Physical Society March Meeting*, Denver, CO, **03/06/2014** (Oral).
- (24) B. J. Nordell, M. M. Paquette, T. D. Nguyen, S. W. King, S. S. Purohit, and A. N. Caruso, ‘Leakage Current Mechanisms in PECVD-Grown Amorphous Hydrogenated Boron Carbide Thin Films,’ *American Physical Society March Meeting*, Denver, CO, **03/06/2014** (Oral).

5.5. Honors/Awards/Promotions

- (1) Anthony N. Caruso – Promotion to associate professor with tenure, **2011**.
Early promotion four years after beginning tenure track appointment.
- (2) Anthony N. Caruso – UM President’s Award for Early Career Excellence, **2012**.
This award recognizes faculty who exhibit exceptional promise within their first seven years with the university. Promise may be demonstrated in scholarship, research, or creativity.
- (3) Anthony N. Caruso – Office of Naval Research Young Investigator’s Award, **2012**.
Received for the proposed research program entitled ‘Prompt Neutron Spectrometry for Identification of SNM in Unknown Shielding Configurations.’

(4) Michelle M. Paquette – Promotion from Postdoctoral Research Associate to Assistant Research Professor, **2013**.

(5) Anthony N. Caruso – UMKC N.T. Veatch Award for Distinguished Research and Creative Activity, **2014**.

Recognizes distinguished research and other scholarly or creative activity accomplished by UMKC faculty.

(6) Justin D. Hurley – UMKC School of Graduate Studies Research Grant Program Award, **2014**.

Received for the proposal entitled, ‘Photoconductivity Studies of Amorphous Hydrogenated Boron Carbide’ (\$6000)

(7) Thuong D. Nguyen – UMKC Trustee's Scholarship (full scholarship), **2014**.

(8) Thuong D. Nguyen – University Chancellor's Scholar Award (\$2500), **2014**.

5.6. Graduations

(1) Christopher L. Keck – B.Sc. Graduation, 05/17/2013

(2) M. Sky Driver – Ph.D. Graduation, 05/17/2013

(3) Thuong D. Nguyen – High school graduation, 05/13/2014

(4) Christopher L. Keck – M.Sc. Graduation, 05/15/2015

6. REFERENCES

1. Caruso, A. N. The physics of solid-state neutron detector materials and geometries. *J. Phys. Condens. Matter* **22**, 443201 (2010).
2. McGregor, D. S., Bellinger, S. L. & Shultz, J. K. Present status of microstructured semiconductor neutron detectors. *J. Cryst. Growth* **379**, 99–110 (2013).
3. Bellinger, S. L., Fronk, R. G., McGregor, D. S. & Sobering, T. J. Arrayed High Efficiency Dual-Integrated Microstructured Semiconductor Neutron Detectors. *2011 IEEE Nucl. Sci. Symp. Conf. Rec.* 1281–1284 (2011).
4. Bellinger, S. L., Fronk, R. G., Sobering, T. J. & McGregor, D. S. High-efficiency microstructured semiconductor neutron detectors that are arrayed, dual-integrated, and stacked. *Appl. Radiat. Isot.* **70**, 1121–4 (2012).
5. Shao, Q. *et al.* High aspect ratio composite structures with 48.5% thermal neutron detection efficiency. *Appl. Phys. Lett.* **102**, 063505 (2013).

6. Shultz, J. K. & McGregor, D. S. Design and performance considerations for perforated semiconductor thermal-neutron detectors. *Nucl. Instruments Methods Phys. Res. Sect. A Accel. Spectrometers, Detect. Assoc. Equip.* **606**, 608–636 (2009).
7. Runkle, R. C., Bernstein, A. & Vanier, P. E. Securing special nuclear material: Recent advances in neutron detection and their role in nonproliferation. *J. Appl. Phys.* **108**, 111101 (2010).
8. Kumashiro, Y. & Okada, Y. Schottky barrier diodes using thick, well-characterized boron phosphide wafers. *Appl. Phys. Lett.* **47**, 64–66 (1985).
9. Doty, F. P. Boron nitride solid state neutron detector. US Patent No. 6,727,504 B1 (2004).
10. Uher, J., Pospisil, S., Linhart, V. & Schieber, M. Efficiency of composite boron nitride neutron detectors in comparison with helium-3 detectors. *Appl. Phys. Lett.* **90**, 124101 (2007).
11. McGinnis, W. C., Diego, S. S. C. S., Clarke, R. & Cionca, C. Film Implementation of a Neutron Detector (FIND): Critical Materials Properties. (2007).
12. Li, J., Dahal, R., Majety, S., Lin, J. Y. & Jiang, H. X. Hexagonal boron nitride epitaxial layers as neutron detector materials. *Nucl. Instruments Methods Phys. Res. Sect. A Accel. Spectrometers, Detect. Assoc. Equip.* **654**, 417–420 (2011).
13. Robertson, B. W. *et al.* A class of boron-rich solid-state neutron detectors. *Appl. Phys. Lett.* **80**, 3644–3646 (2002).
14. Hong, N., Mullins, J., Foreman, K. & Adenwalla, S. Boron carbide based solid state neutron detectors: the effects of bias and time constant on detection efficiency. *J. Phys. D. Appl. Phys.* **43**, 275101 (2010).
15. Whiteley, C. E. *et al.* Semiconducting icosahedral boron arsenide crystal growth for neutron detection. *J. Cryst. Growth* **318**, 553–557 (2011).
16. Bakalova, S., Speller, R., Lacey, R. J., Frost, C. & Kuball, M. Novel n-type Mg₂B₁₄ on silicon diode: Demonstration of a thermal solid state neutron detector. *Nucl. Instruments Methods Phys. Res. Sect. A Accel. Spectrometers, Detect. Assoc. Equip.* **700**, 140–144 (2013).
17. Werheit, H. Some properties of single-crystal boron carbide. *J. Solid State Chem.* **177**, 575–579 (2004).
18. Lundstedt, C., Harken, A., Day, E., Robertson, B. & Adenwalla, S. Modeling solid-state boron carbide low energy neutron detectors. *Nucl. Instruments Methods Phys. Res. Sect. A Accel. Spectrometers, Detect. Assoc. Equip.* **562**, 380–388 (2006).

19. Schlesinger, T. E. *et al.* Cadmium zinc telluride and its use as a nuclear radiation detector material. *Mater. Sci. Eng. R Reports* **32**, 103–189 (2001).
20. Lee, S., Mazurowski, J., Ramseyer, G. & Dowben, P. A. Characterization of boron carbide thin films fabricated by plasma enhanced chemical vapor deposition from boranes. *J. Appl. Phys.* **72**, 4925–4933 (1992).
21. Sunwoo Lee & Dowben, P. A. The Properties of Boron Carbide/Silicon Heterojunction Diodes Fabricated by Plasma-Enhanced Chemical Vapor Deposition. *Appl. Phys. A* **58**, 223–227 (1994).
22. Hong, N., Langell, M. A., Liu, J., Kizilkaya, O. & Adenwalla, S. Ni doping of semiconducting boron carbide. *J. Appl. Phys.* **107**, 024513 (2010).
23. Nordell, B. J. *et al.* The Influence of Hydrogen on the Chemical, Mechanical, Optical/Electronic, and Electrical Transport Properties of Amorphous Hydrogenated Boron Carbide. *J. Appl. Phys.* **118**, 035703 (2015).
24. Driver, M. S., Paquette, M. M., Karki, S., Nordell, B. J. & Caruso, a N. The electronic and chemical structure of the a-B(3)CO(0.5):H(y)-to-metal interface from photoemission spectroscopy: implications for Schottky barrier heights. *J. Phys. Condens. Matter* **24**, 445001 (2012).
25. Michaelson, H. B. The work function of the elements and its periodicity. *J. Appl. Phys.* **48**, 4729–4733 (1977).
26. Grosvenor, A. P., Biesinger, M. C., Smart, R. S. C. & McIntyre, N. S. New interpretations of XPS spectra of nickel metal and oxides. *Surf. Sci.* **600**, 1771–1779 (2006).
27. Moulder, J. F., Stickle, W. F., Sobol, P. E. & Bomben, K. D. *Handbook of X-ray Photoelectron Spectroscopy. Surf. Interface Anal.* **3**, (1992).
28. Gonzalez-Elipe, A. R., Holgado, J. P., Alvarez, R. & Munuera, C. Use of Factor Analysis and XPS To Study Defective Nickel Oxide. *J. Phys. Chem.* **96**, 3080–3086 (1992).
29. Legrand, J., Gota, S., Guittet, M.-J. & Petit, C. Synthesis and XPS Characterization of Nickel Boride Nanoparticles. *Langmuir* **18**, 4131–4137 (2002).
30. Eastman, D. E. Photoemission Studies of the Electronic Structure of Transition Metals. *J. Appl. Phys.* **40**, 1387–1394 (1969).
31. Kibis, L. S., Titkov, A. I., Stadnichenko, A. I., Koscheev, S. V. & Boronin, A. I. X-ray photoelectron spectroscopy study of Pd oxidation by RF discharge in oxygen. *Appl. Surf. Sci.* **255**, 9248–9254 (2009).

32. Wang, Y. & Trenary, M. Surface chemistry of boron oxidation. 2. The reactions of boron oxides B₂O₂ and B₂O₃ with boron films grown on tantalum(110). *Chem. Mater.* **5**, 199–205 (1993).
33. Moon, O., Kang, B., Lee, S. & Boo, J. Temperature effect on structural properties of boron oxide thin films deposited by MOCVD method. *Thin Solid Films* **464-465**, 164–169 (2004).
34. Pillo, T., Zimmermann, R., Steiner, P. & Hufner, S. The electronic structure of PdO found by photoemission (UPS and XPS) and inverse photoemission (BIS). *J. Phys. Condens. Matter* **9**, 3987–3999 (1997).
35. S. Hufner, G. K. Werthem, and D. N. E. B. X-Ray Photoemission Spectra of Palladium. *Chem. Phys. Lett.* **24**, 527–530 (1974).
36. Heras, J. M., Estiu, G. & Viscido, L. Annealing behaviour of clean and oxygen covered polycrystalline palladium films: A work function and electrical resistance study. *Thin Solid Films* **188**, 165–172 (1990).
37. Blakesley, J. C. *et al.* Towards reliable charge-mobility benchmark measurements for organic semiconductors. *Org. Electron.* **15**, 1263–1272 (2014).
38. Baranovski, S. D. & Rubel, O. in *Charge Transport in Disordered Solids with Applications in Electronics* (Baranovski, S.) 49–96 (Wiley, 2006).
39. Kokil, A., Yang, K. & Kumar, J. Techniques for characterization of charge carrier mobility in organic semiconductors. *J. Polym. Sci. Part B Polym. Phys.* **50**, 1130–1144 (2012).
40. Weiβ, O. J., Krause, R. K. & Hunze, A. Hole mobility of 1-NaphDATA. *J. Appl. Phys.* **103**, 043709 (2008).
41. Silver, M. & Shaw, M. P. in *Photoconductivity and Related Phenomena* (Mort, J. & Pai, D. M.) (Elsevier, 1976).
42. Lampert. *Current Injection in Solids* (1970).
43. Takeshita, S. Modeling of space-charge-limited current injection incorporating an advanced model of the Poole-Frenkel effect. Dissertation (2008).
44. Murgatroyd, P. N. Theory of space-charge-limited current enhanced by Frenkel effect. *J. Phys. D. Appl. Phys.* **3**, 151–156 (1970).
45. Majumdar, H. S., Bolognesi, A. & Pal, A. J. Memory applications of a thiophene-based conjugated polymer: capacitance measurements. *J. Phys. D. Appl. Phys.* **36**, 211–215 (2002).

46. Xia, Y., He, W., Chen, L., Meng, X. & Liu, Z. Field-induced resistive switching based on space-charge-limited current. *Appl. Phys. Lett.* **90**, 022907 (2007).
47. Lin, Y.-J. Hysteresis-type current-voltage characteristics of indium tin oxide/poly(3,4-ethylenedioxythiophene) doped with poly(4-styrenesulfonate)/indium tin oxide devices. *J. Appl. Phys.* **103**, 063702 (2008).
48. Many, A. & Rakavy, G. Theory of Transient Space-Charge-Limited Currents in Solids in the Presence of Trapping. *Phys. Rev.* **126**, 1980–1988 (1962).
49. Eward, T. *et al.* A metrology perspective on the dark injection transient current method for charge mobility determination in organic semiconductors. *J. Appl. Phys.* **109**, 093707 (2011).
50. Scott, J. C., Ramos, S. & Malliaras, G. G. Transient Space-Charge-Limited Current Measurements of Mobility in a Luminescent Polymer. *J. Imaging Sci. Technol.* **43**, 233–236 (1999).
51. Szymanski, M. Z., Luszczynska, B., Verilhac, J.-M., Reiss, P. & Djurado, D. Simplified transient space-charge-limited current measurements of mobility using transimpedance amplifier. *Org. Electron.* **14**, 230–235 (2013).
52. Yap, B. K., Koh, S. P., Tiong, S. K. & Ong, C. N. Space-Charge-Limited Dark Injection (SCL DI) transient measurements. *2010 IEEE Int. Conf. Semicond. Electron.* 192–194 (2010). doi:10.1109/SMELEC.2010.5549542
53. Mozer, A. J. & Sariciftci, N. S. Negative electric field dependence of charge carrier drift mobility in conjugated, semiconducting polymers. *Chem. Phys. Lett.* **389**, 438–442 (2004).
54. Conte, G., Rossi, M. C., Salvatori, S., Ascarelli, P. & Trucchi, D. Thin polycrystalline diamond for low-energy x-ray detection. *J. Appl. Phys.* **96**, 6415 (2004).
55. Cui, Y., Groza, M., Hillman, D., Burger, A. & James, R. B. Study of surface recombination velocity of Cd(1-x)Zn(x)Te radiation detectors by direct current photoconductivity. *J. Appl. Phys.* **92**, 2556 (2002).
56. Many, A. High-field effects in photoconducting cadmium sulphide. *J. Phys. Chem. Solids* **26**, 575–578 (1965).
57. Zanichelli, M., Santi, A., Pavesi, M. & Zappettini, A. Charge collection in semi-insulator radiation detectors in the presence of a linear decreasing electric field. *J. Phys. D: Appl. Phys.* **46**, 365103 (2013).
58. Street, R. A. *Hydrogenated Amorphous Silicon*. (Cambridge University Press, 1991).

59. Wood, D. L. & Tauc, J. Weak Absorption Tails in Amorphous Semiconductors. *Phys. Rev. B* **5**, 3144–3151 (1972).
60. Cody, G. D. Urbach edge of crystalline and amorphous silicon: a personal review. *J. Non. Cryst. Solids* **141**, 3–15 (1992).
61. Sweenor, D. E., O’Leary, S. K. & Foutz, B. E. On defining the optical gap of an amorphous semiconductor: an empirical calibration for the case of hydrogenated amorphous silicon. *Solid State Commun.* **110**, 281–286 (1999).
62. Basa, D. K. Correlation between the opto-electronic and structural parameters of amorphous semiconductors. *Thin Solid Films* **406**, 75–78 (2002).
63. Hori, A., Takeda, M., Yamashita, H. & Kimura, K. Absorption Edge Spectra of Boron-Rich Amorphous Films Constructed with Icosahedral Cluster. *J. Phys. Soc. Japan* **64**, 3496–3505 (1995).
64. Forouhi, A. R. & Bloomer, I. Optical dispersion relations for amorphous semiconductors and amorphous dielectrics. *Phys. Rev. B* **34**, 7018–7026 (1986).
65. Mauro, J. C. Topological constraint theory of glass. *Am. Ceram. Soc. Bull.* **90**, 31–37 (2011).
66. Knoll, G. *Radiation detection and measurement*. (John Wiley & Sons Inc., 2010).
67. Domnich, V., Reynaud, S., Haber, R. A. & Chhowalla, M. Boron Carbide: Structure, Properties, and Stability under Stress. *J. Am. Ceram. Soc.* **94**, 3605–3628 (2011).
68. Ramo, S. Currents Induced by Electron Motion. *Proc. IRE* **27**, 0–1 (1939).
69. Shockley, W. Currents to conductors induced by a moving point charge. *J. Appl. Phys.* **9**, 635–636 (1938).
70. Ziegler, J. F. *Volume 3 of The Stopping and Ranges*. (1976).
71. Klein, C. a. Bandgap Dependence and Related Features of Radiation Ionization Energies in Semiconductors. *J. Appl. Phys.* **39**, 2029 (1968).
72. Liu, C. Conductivity transition of semiconducting boron carbide by doping. *Mater. Lett.* **49**, 308–312 (2001).

Appendix A

Establishing Electrical Contacts for Amorphous Hydrogenated Boron Carbide

Michelle M. Paquette,¹ Joseph W. Otto,¹ Sudarshan Karki,¹ Bradley J. Nordell,¹ M. Sky Driver,¹ Thuong D. Nguyen,¹ Christopher L. Keck,¹ Brent J. Rogers,¹ Andrew Kitahara,¹ Sean W. King,² William A. Lanford,³ Sudhaunshu Purohit,⁴ Wenjing Li,⁴ Chi Zhang,⁴ Nathan A. Oyler,⁴ and A. N. Caruso¹

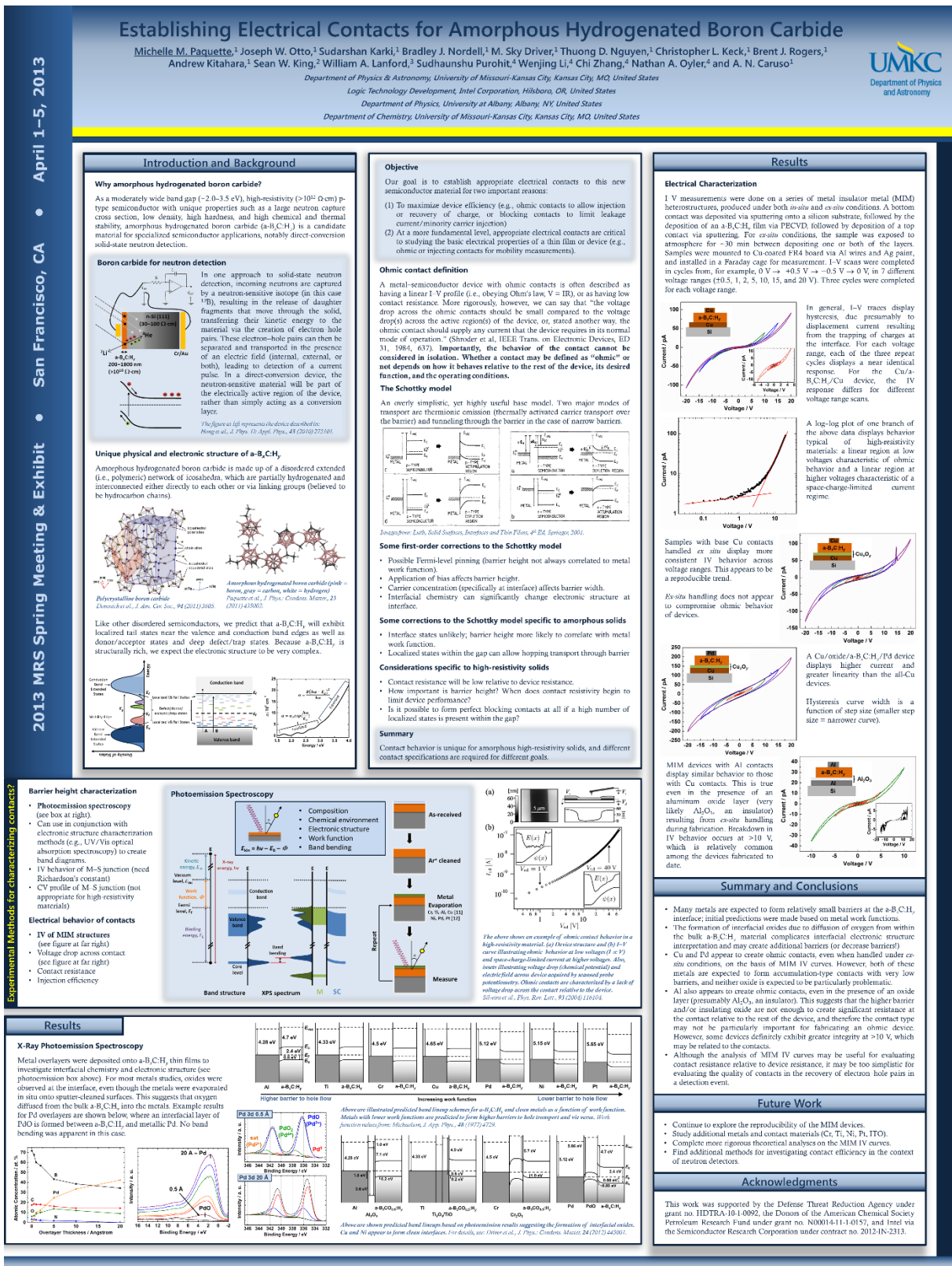
Department of Physics & Astronomy, University of Missouri-Kansas City, Kansas City, MO, United States

Logic Technology Development, Intel Corporation, Hillsboro, OR, United States

Department of Physics, University at Albany, Albany, NY, United States

 UMKC
Department of Physics
and Astronomy

2013 MRS Spring Meeting & Exhibit • San Francisco, CA • April 1-5, 2013



DISTRIBUTION LIST
DTRA-TR-16-63

DEPARTMENT OF DEFENSE

DEFENSE THREAT REDUCTION
AGENCY
8725 JOHN J. KINGMAN ROAD
STOP 6201
FORT BELVOIR, VA 22060
ATTN: D. PETERSEN

DEFENSE TECHNICAL
INFORMATION CENTER
8725 JOHN J. KINGMAN ROAD,
SUITE 0944
FT. BELVOIR, VA 22060-6201
ATTN: DTIC/OCA

**DEPARTMENT OF DEFENSE
CONTRACTORS**

QUANTERION SOLUTIONS, INC.
1680 TEXAS STREET, SE
KIRTLAND AFB, NM 87117-5669
ATTN: DTRIAC